

Upscaling of Lacustrine Groundwater Discharge by Fiber Optic Distributed Temperature Sensing and Thermal Infrared imaging

Dissertation

zur Erlangung des akademischen Grades

doctor rerum naturalium

(Dr. rer. nat.)

im Fach Geographie

eingereicht an der

Mathematisch-Naturwissenschaftlichen Fakultät

der Humboldt-Universität zu Berlin

von

Agrarwirtschafts Ingenieurin Amaya Irene, Marruedo Arricibita

Präsidentin/Präsident der Humboldt-Universität zu Berlin

Prof. Dr.-Ing. Dr. Sabine Kurst

Dekanin/Dekan der Mathematisch-Naturwissenschaftlichen Fakultät

Prof. Dr. Elmar Kulke

Gutachter/innen:

1. Prof. Dr. Gunnar Nützmann

2. Prof. Dr. Jörg Lewandowski

3. Prof. Dr. Jan Fleckenstein

Tag der Einreichung: 4.12.2017

Tag der mündlichen Prüfung: 17.05.2018

Abstract

Groundwater (GW) and surface water (SW) are nowadays considered closely coupled entities of a hydrological continuum. GW exfiltration into lakes (lacustrine groundwater discharge, LGD) can have significant impacts on lake water quantity and quality. This entails the need to understand the mechanisms relevant in the context of LGD and to develop and improve measurement methods for LGD. Multiple approaches to identify and quantify LGD are based on significant temperature differences between GW and lake water and the measurement of related heat transport. The main aim of the present PhD thesis is to study signal propagation from the point scale of LGD at the sediment-water interface across the overlying water body to the water surface-atmosphere interface. The PhD thesis tests the hypothesis that the positive buoyancy of warm GW causes upwelling across the cold water column and allows the detection of LGD at the water surface by thermal infrared imaging (TIR). For that purpose, a general conceptual framework is developed based on hierarchical patch dynamics (HPD). It aims to guide the researchers in this field, on adequately combining multiple heat tracing techniques to identify and quantify heat and water exchange over several spatial scales and across ecohydrological interfaces in freshwater environments (Chapter 2). The conceptual framework was used for the design of a mesocosm experiment (Chapters 3 and 4). Different LGD rates were simulated by injecting relatively warm water at the bottom of an outdoor mesocosm. A fiber optic distributed temperature sensing (FO-DTS) cable was installed in a 3D setup at multiple depths in the water column to trace the heat signal of the simulated LGD under different weather conditions and over entire diurnal cycles. Additionally, a TIR camera was mounted 4 meters above the mesocosm to monitor water surface temperatures. TIR images were validated using FO-DTS temperature data 2 cm below the water surface (Chapter 4). The positive buoyancy of relatively warm LGD allows the detection of GW across the water column and at the water surface-atmosphere interface by FO-DTS and TIR. Hydrometeorological factors such as cloud cover and diurnal cycle of net radiation strongly control: 1) the upwelling of simulated LGD across the water column (Chapter 3) and 2) the reliability of TIR for detection of LGD at the water surface-atmosphere interface (Chapter 4). In both cases, optimal results are obtained under overcast conditions and during night. Thus, detection of upwelling of LGD across the water column and at the water surface-atmosphere interface is only possible if heat fluxes related to LGD are not overshadowed by heat fluxes of other sources across the water surface-atmosphere interface. Even though the present study proves that the LGD signal can be identified by TIR at the water surface, it can also be concluded that TIR will be only restrictedly applicable in real world case studies.

Keywords: Lacustrine groundwater discharge, Thermal infrared, Fiber optic distributed temperature sensing, Heat tracing.

Zusammenfassung

Grund- und Oberflächenwasser werden heutzutage als hydraulisch eng verbundene Kompartimente eines hydrologischen Kontinuums angesehen. Der Zustrom von Grundwasser zu Seen (engl. lacustrine groundwater discharge, LGD) kann signifikante Auswirkungen auf Qualität und Quantität des Seewasser haben. Dementsprechend besteht die Notwendigkeit die zugrunde liegenden Prozesse zu verstehen und geeignete Methoden zur Erfassung von LGD zu entwickeln. Viele Ansätze zur Identifikation und Quantifizierung von LGD basieren auf signifikanten Temperaturunterschieden zwischen Grund- und Seewasser und der Messung des damit einhergehenden Wärmetransports. Hauptziel der vorliegenden Doktorarbeit ist es, Signalfortpflanzung und -ausbreitung des Grundwasserzustroms zu untersuchen – von der Punktskala des LGD an der Sediment-Wasser Grenzfläche durch den Wasserkörper zur Grenzfläche Wasseroberfläche-Atmosphäre. Die Doktorarbeit testet die Hypothese, dass das im Verhältnis zum Umgebungswasser leichtere warme Grundwasser in der kalten Wassersäule aufsteigt (engl. upwelling) und eine Detektion von LGD an der Wasseroberfläche mit thermalen Infrarot (TIR) Aufnahmen erlaubt. Zu diesem Zweck wird zunächst mit der „hierarchical patch dynamics (HPD)“ ein konzeptioneller Rahmen entwickelt, der dazu dienen soll, eine angemessene Kombination multipler Techniken zur Erfassung von Wärme- und Wasserflüssen anzubieten (Kapitel 2). Dabei sollen verschiedene räumliche Skalen und ökohydrologische Grenzflächen in Süßwassersystemen abgedeckt werden. Die HPD wurde als Grundlage für das Design eines Mesokosmos-Experimentes genutzt (Kapitel 3 und 4). Dabei wurden unterschiedliche LGD-Raten durch den Zustrom von relativ warmem Wasser am Grund eines Outdoor-Pools simuliert. Ein Glasfaserkabel (engl. fibre-optic distributed temperature sensing, FO-DTS) wurde in einem 3D Aufbau in verschiedenen Tiefen der Wassersäule installiert, um das Wärmesignal des simulierten Grundwasserzustroms zu verfolgen – unter verschiedenen Witterungsbedingungen und im Laufe eines kompletten Tagesgangs. Zusätzlich wurde 4 m über dem Mesokosmos eine TIR-Kamera installiert, um die Temperatur des Oberflächenwassers aufzuzeichnen. Die TIR-Aufnahmen wurden mit Temperaturen, die mit FO-DTS 2 cm unter der Wasseroberfläche gemessen worden waren, validiert (Kapitel 4). Die Anwendung von FO-DTS und TIR ermöglicht die Detektion von LGD in der Wassersäule und an der Grenzfläche Wasseroberfläche-Atmosphäre. Hydrometeorologische Faktoren wie Wolkenbedeckung und der Tagesgang der Netto-Strahlung kontrollieren: 1) den Auftrieb des simulierten LGD in der Wassersäule (Kapitel 3) und 2) die Zuverlässigkeit von TIR bei der Erfassung von LGD an der Grenzfläche zwischen Wasseroberfläche und Atmosphäre (Kapitel 4). In beide Fällen werden die besten Ergebnisse bei Wolkenbedeckung und nachts erzielt. Das heißt, dass der Auftrieb von LGD in der Wassersäule und an der Grenzfläche zwischen Wasseroberfläche und Atmosphäre nur erfasst werden kann, wenn die LGD-bedingten Wärmeflüsse nicht durch andere Wärmeflüsse über die Grenzfläche zwischen Wasseroberfläche und Atmosphäre überdeckt werden. Obwohl die vorliegende Studie zeigt, dass das LGD-Signal mit TIR an der Wasseroberfläche erfasst werden kann, muss einschränkend auch der Schluss gezogen werden, dass TIR unter realen in-situ Verhältnissen nur bedingt anwendbar sein wird.

Schlagwörter: Lacustrine groundwater discharge, Thermalen Infrarot, Fiber optic distributed temperature sensing, Wärme als Tracer










Table of contents

1	Introduction	1
1.1	Motivation to study groundwater-surface water interactions	1
1.2	State of the Art: GW-SW interactions	3
1.2.1	<i>Mechanisms of GW-SW interactions</i>	<i>3</i>
1.2.2	<i>Factors controlling GW-SW interactions</i>	<i>4</i>
1.2.3	<i>GW discharge in lakes</i>	<i>5</i>
1.2.4	<i>GW discharge in streams</i>	<i>6</i>
1.3	Measurement methods for GW-SW interactions	6
1.4	Heat as a natural tracer of GW-SW interactions	8
1.4.1	<i>Heat tracing in stream and lake beds</i>	<i>9</i>
1.4.2	<i>Heat tracing in the water column</i>	<i>11</i>
1.5	Scaling in hydrology	13
1.5.1	<i>Can we learn from other disciplines?</i>	<i>16</i>
1.6	Hypothesis and aims of this PhD thesis	17
1.7	References	18
2	Scaling on temperature tracers for water and heat exchange processes in ecohydrological interfaces	28
2.1	Introduction	30
2.2	Theory and methodology of hierarchical patch dynamics	32
2.2.1	<i>Hierarchy theory</i>	<i>33</i>
2.2.2	<i>Patch dynamics in landscape ecology</i>	<i>34</i>
2.2.3	<i>Hierarchical patch dynamics</i>	<i>35</i>
2.3	Application of HPD to water and heat fluxes in freshwater environments	36
2.3.1	<i>Structure of the HPD scheme for generic freshwater environments</i>	<i>36</i>
2.4	Heat tracing techniques in ecohydrological interfaces	39
2.5	Proof of concept: vertical upscaling of discrete GW upwelling by FO-DTS and TIR	43
2.6	Synthesis, conclusions and recommendations	46
	Acknowledgments	48
	Supplementary information	48
	References	49
	Annex S1: Definitions	55
3	Mesocosm experiments identifying hotspots of groundwater upwelling in a water column by fiber optic distributed temperature sensing	58
3.1	Introduction	60
3.2	Material and methods	62
3.2.1	<i>Experimental setup</i>	<i>62</i>

3.2.2	<i>Data analyses and spatial statistics</i>	65
3.2.3	<i>Preprocessing and sources of error</i>	66
3.2.4	<i>Quantification of net heat fluxes across the water surface, advective heat fluxes and internal energy change</i>	67
3.3	Results	67
3.3.1	<i>FO-DTS observed temperature patterns</i>	67
3.3.2	<i>Quantitative analysis of spatial temperature patterns</i>	70
3.3.3	<i>Net heat fluxes across the water surface, advective heat fluxes and internal energy change</i>	76
3.4	Discussion	80
3.5	Conclusion.....	87
	Acknowledgments.....	87
	Supporting information	87
	References	89
	Appendix S1: Quantification of interfacial heat transfer and net-advective heat flux	94
	Appendix S2 Nomenclature	97
4	Thermal infrared imaging for detection of groundwater at the surface of stagnant freshwater bodies.....	102
4.1	Introduction	104
4.2	Methods.....	106
4.2.1	<i>Experimental design.....</i>	106
4.2.2	<i>Measurement protocol and calibration</i>	108
4.2.3	<i>Study period and influence of discharge rates, weather conditions and diurnal cycle</i>	109
4.2.4	<i>Comparison of TIR temperature data with FO-DTS temperature data</i>	110
4.3	Results	111
4.3.1	<i>Comparison of TIR temperature data with FO-DTS temperature data</i>	111
4.4	Discussion	116
4.4.1	<i>Comparison of TIR temperature data with FO-DTS temperature data</i>	116
4.4.2	<i>Influence of discharge rates, weather conditions and the diurnal cycle</i>	116
4.4.3	<i>Experimental shortcomings and future improvements</i>	118
4.4.4	<i>Implications of results for TIR based monitoring of groundwater upwelling</i>	119
4.5	Conclusions	120
	Acknowledgments and Data.....	121
	References	122
5	Synopsis.....	130
5.1	Summary of results.....	130

5.2	Discussion	130
5.2.1	<i>Impacts of diurnal cycle of net radiation and cloud cover on tracing of LGD .</i>	130
5.2.2	<i>FO-DTS for monitoring LGD in lakes.....</i>	132
5.2.3	<i>TIR imaging for detection of LGD at the lake surface</i>	133
5.2.4	<i>Combination of multiple heat tracing techniques for scaling of GW-SW interactions across ecohydrological interfaces.....</i>	134
5.3	Conclusions	136
5.4	Future direction	137
5.5	References	139
Acknowledgements.....		144
Declaration of independent work.....		145

List of figures

Figure 1.1 Unsaturated zone, saturated zone, GW and SW in freshwater systems (Taken and modified from Winter, 1998).....	4
Figure 1.2 Sediment temperatures against depth (z): for gaining and losing conditions (green and red lines respectively) and for daily (in italic) or annual cycles. For annual cycles the depth at which the temperature reaches a constant value can be 10 m or more at downward flow. On the contrary, the depth at which the temperatures reach constant values at upward flows can be less than 1 meter. Taken from Constantz and Stonestrom (2003).....	11
Figure 2.1 Conceptualization of heat and water exchange processes at freshwater ecosystem across several ecohydrological interfaces.	31
Figure 2.2 Hierarchical conceptualización of heat and water exchange processes at freshwater ecosystems at different spatial and temporal scales and across different ecohydrological interfaces.	34
Figure 2.3 An HPD based conceptual guideline on how to adequately observe water/heat exchange processes across spatial scales and ecohydrogological interfaces by combination of different heat tracing techniques.....	38
Figure 2.4 Application of different experimental temperature tracing techniques to identify heat and water fluxes at different ecohydrological interfaces in freshwater environments defined in Figures 2.1, 2.2 and 2.3.	42
Figure 2.5 Example for vertical scaling of water and heat exchanges related to simulated LGD.44	
Figure 3.1 Sketch of the experimental set up showing a cross section through the mesocosm including the fibre optic distributed temperature sensing set up.	63
Figure 3.2 (a) Raw temperature data (black line) and smoothed temperature data with local polynomial regression fitting (LOESS; red line) and (b) temperature difference between raw temperature data and smoothed temperature data.	67
Figure 3.3 Slice3D plots visualizing for the four layers of DTS measurements the difference from the minimum temperature of each dataset. Values averaged for approximately 12 hr day (always left of colour scale) or night (always right), respectively. Different injection rates and weather conditions as follows: (a) 1 L min ⁻¹ clear 19.03.2015, (b) 1 L min ⁻¹ partly cloudy 25.03.2015, (c) 5.5 L min ⁻¹ clear 18.03.2015, (d) 1 L min ⁻¹ overcast 26.03.2015, (e) 5 L min ⁻¹ overcast 27.03.2015, and (f) 15 L min ⁻¹ overcast 12.03.2015.  inlet of cold lake water,  inlet of warm water,  outlet of mixed water from mesocosm.  clear day,  clear night,  partly cloudy day,  partly cloudy night,  overcast day, and  overcast night.....	69
Figure 3.4 (a) and (b) Moran's I scatterplots, (c) and (d) LISA maps, (a) and (c) for 1 L min ⁻¹ clear sky, day, (b) and (d) for 15 L min ⁻¹ overcast sky, day. In (a) and (b), potential influencing measures for the linear relationship between the data and the lag are highlighted as red diamond shape. In (c)	

and (d), red coloured points belong to the high-high quadrant in Moran's I scatterplot, yellow coloured points belong to the low-low quadrant in Moran's I scatterplot, and blue coloured points are spatially nonsignificant points. From top row to bottom row: Layers 4, 3, 2, and 1. 71

Figure 3.5 Moran's I values. (a) Day, clear and partly cloudy sky; (b) night, clear and partly cloudy sky; (c) day, overcast sky; and (d) night, overcast sky. All plots are plotted from lowest to highest injection rates. 72

Figure 3.6 Spatial correlation coefficients for (a) day, clear sky and partly cloudy conditions; (b) night and clear sky, partly cloudy conditions; (c) day and overcast conditions; (d) night and overcast conditions. 75

Figure 3.7 Calculated heat fluxes across the water surface (G), net radiation (R_n) evaporative heat flux (λE), and sensible heat flux (H) for (a) control dataset with 0 L min^{-1} injection rate, overcast, (c) 1 L min^{-1} clear, (e) 1 L min^{-1} partly cloudy, (g) 1 L min^{-1} overcast, (i) 5.5 L min^{-1} clear, (k) 5 L min^{-1} overcast, and (m) 15 L min^{-1} overcast and calculated ΔE , E_G and E_{adv} for (b) control experiment overcast (d) 1 L min^{-1} clear, (f) 1 L min^{-1} partly cloudy, (h) 1 L min^{-1} overcast, (j) 5.5 L min^{-1} clear, (l) 5 L min^{-1} overcast, and (n) 15 L min^{-1} overcast. 78

Figure 3.8 Change of energy (ΔE) over time for seven datasets: 1 L min^{-1} clear, 1 L min^{-1} partly cloudy, 1 L min^{-1} overcast, 5.5 L min^{-1} clear, 5 L min^{-1} overcast, 15 L min^{-1} overcast, and control dataset with 0 L min^{-1} injection rate, overcast conditions. 79

Figure 3.9 Conceptual model of spatial distribution of injected water in the water column under different weather conditions, for different injection rates during (a) day and (b) night. (a.1) and (b.1) 1 L min^{-1} , clear sky; (a.2) and (b.2) 1 L min^{-1} , partly cloudy sky; (a.3) and (b.3) 1 L min^{-1} , overcast sky; (a.4) and (b.4) clear sky, 5.5 L min^{-1} ; (a.5) and (b.5) 5 L min^{-1} , overcast sky; (a.6) and (b.6) 15 L min^{-1} , overcast sky. The degree of the signal strength is indicated by the intensity of the red colour: Light red: weak signal, dark red: strong signal. The size of the arrows indicates the strength of the R_{nl} and R_{ns} . The blue colour indicates the losses of energy from the mesocosm. The red colour indicates the gains of energy in the mesocosm. 83

Figure 4.1 Schematic of the mesocosm experimental design including TIR setup and the upper layer of the FO-DTS. 107

Figure 4.2 Visual comparison of TIR temperature data with FO-DTS temperature data. Worst (left) and best (right) spatially correlated datasets for overcast conditions at three injection rates: a) 1 L min^{-1} , b) 5 L min^{-1} and c) 15 L min^{-1} . Temperature signal corresponding to the warm water injection is indicated with a black arrow in Fig. 4.2a and b. 113

Figure 4.3 Visual comparison of TIR temperature data with FO-DTS temperature data. Worst (left) and best (right) correlated datasets for clear conditions at three injection rates: a) 1 L min^{-1} and b) 5 L min^{-1} 114

Figure 4.4 Bivariate Global Moran’s I values for spatial correlation between FO-DTS and TIR temperature data under overcast weather conditions, for three injection rates: a) 1 L min⁻¹, b) 5 L min⁻¹ and c) 15 L min⁻¹. 115

Figure 4.5 Bivariate Global Moran’s I values for spatial correlation between FO-DTS and TIR temperature data under clear sky conditions, for two injection rates: a) 1 L min⁻¹ and b) 5 L min⁻¹. 115

List of tables

Table 1.1 LGD examples reported as percentage of the lake water balance and as absolute rates. 3

Table 2.1 Summary of the heat tracing techniques that are considered in this paper for scaling of water and heat fluxes in freshwater environments: scales, limitations and recommendations. Scales used in this paper are: Point/Small (few cm), local (cm to few m), reach, plot or lake shore (from few m), stream, land or lake (from m to km) and finally catchment (from km). “Temp.” goes for temperature. 41

Table 4.1 24-hour measurements with FO-DTS and TIR camera. The control dataset is only used as a reference for the initial conditions of the mesocosm measurements and is not included in the results. 109

Table S1 Spatial correlation coefficients between layers. 100

List of abbreviations

GW: Groundwater

SW: Surface water

LGD: Lacustrine groundwater discharge

HZ: Hyporheic zone

HEF: Hyporheic exchange flow

FO-DTS: Fiber optic distributed temperature sensor

TIR: Thermal infrared

HPS: Heat pulse sensor

HT: Hierarchy theory

PD: Patch dynamics

HPD: Hierarchical patch dynamics

1 Introduction

1.1 Motivation to study groundwater-surface water interactions

Freshwater is essential for human life and societies. Lakes, rivers and aquifers, among others, are important sources of freshwater. Therefore preserving quality and quantity of freshwater in these systems is crucial. In addition, it is important to maintain the integrity of these freshwater systems because they provide multiple services such as flood control, habitats for numerous plant, animal and other species, production of fish or purification of human and industrial wastes. The failure to keep the integrity of these freshwater systems will lead to loss of species and other of the above mentioned ecosystems services (Baron *et al.*, 2002). In 2015, the European Environmental Agency (EEA) reported that more than half of the rivers and lakes in Europe did not hold a good ecological status as requested by the European Water Framework Directive (EC, 2000) (European Environmental Agency, 2015). Furthermore, about 25% of groundwater across Europe had a poor chemical status in 2015 according to the EEA. At European level, groundwater is the most important drinking water source in many European regions (Bartel *et al.*, 2016). Nowadays' widespread intense agriculture is often claimed to be responsible for the situation described above. Agricultural activities often include intensive use of pesticides and fertilizers that end up in surface waters (SW) and groundwater (GW). In addition, discharge of waste water from industry, transport, mining and households are also a source of pollution for freshwaters (European Environmental Agency, 2015). GW and SW are often hydrologically closely connected and by that might influence each other in quality and quantity (Winter *et al.*, 1998). Therefore, knowledge on how GW is connected to SW can be of major relevance to design successful management strategies (Winter *et al.*, 1998) to maintain or improve the quality and quantity of GW and SW.

For a long time, GW and SW have been studied as individual entities. In fact, GW and SW differ to some extent in their chemical, biological and physical features (Kalbus *et al.*, 2006). However, over the last decades, an important paradigm shift has taken place: from a static image of rivers, lakes and aquifers as discrete bodies, respectively, to a more complex and dynamic interpretation of GW and SW as undivided constituents of a stream/lake-catchment continuum (Krause *et al.*, 2011). Thus, GW and SW are now considered as connected entities (Winter *et al.*, 1998) which interact across and within different interfaces. The interfaces where GW and SW interact are generally distinguished by permeable sediments with saturated conditions and low flow velocities (e.g. the hyporheic zone (HZ) in streams or

lacustrine sediments in lakes) (Kalbus *et al.*, 2006). Dynamic and non-stationary biogeochemical and physical processes take place at these interfaces (Krause *et al.*, 2017), which include transport, degradation, transformation, precipitation or sorption of compounds (Kalbus *et al.*, 2006). These interfaces can contribute significantly to SW metabolism and biota as well (Brunke and Gonser, 1997). Thus, GW-SW interactions have a relevant influence on the water quality of SW bodies such as streams and lakes as well as on aquifers (Kalbus *et al.*, 2006).

In the last decades, there has been an increased interest in GW-SW interactions (Fleckenstein *et al.*, 2010). With the adoption of The European Water Framework Directive (EC, 2000) in 2000 the motivation to investigate GW-SW interactions increased even more. The relevance of GW-SW interfaces has been acknowledged by several authors who described GW-SW interfaces as “hotspots” (areas of intensified activity: Frei *et al.*, 2012; Krause *et al.*, 2013) or areas, where interaction between GW and SW takes place (Winter, 1999; Krause *et al.*, 2011; Lewandowski *et al.*, 2014). Nevertheless, complete understanding on the functioning of these “hotspots” is still a knowledge gap necessary to describe GW-SW interactions in aquatic environments.

In lakes, all flow of GW from the lake bed (i.e. the interface) to the lake is referred to as lacustrine groundwater discharge (LGD) (Lewandowski *et al.*, 2014). GW-SW interactions in lake systems might be different to the ones observed at stream-aquifer interfaces (i.e. in the HZ). Therefore, different definitions and influencing factors come into consideration. Research on GW-lake interactions is not as common as research on GW-streams interactions and the function of the HZ (Lewandowski *et al.*, 2014). Especially when it comes to water and nutrient budgets LGD has long been ignored due to several reasons, (Meinikmann *et al.*, 2013; Lewandowski *et al.*, 2014):

- Difficulty of access the interface due to the depth of lakes
- Low local discharge rates due to large extent of the interface
- Lack of appropriate methodology
- Large spatial and temporal variability of discharge rates and GW composition which requires high numbers of measurements in order to get reliable estimates of the LGD component in budgets
- GW can be relevant in nutrient budgets even if it is not relevant in water budgets because concentrations in groundwater might be much higher than in lake water.

For example, Meinikmann *et al.* (2015) demonstrated that more than 50% of external phosphorus loads to an eutrophied lake, were discharged by GW. By that LGD was identified to be a main driver of lake eutrophication. In this example LGD accounted for only about 25% of the lake's water balance. In contrast to that, LGD is often the dominant component in the water balance of lakes (Table 1, Lewandowski *et al.*, 2014). By that they have the natural potential to also contribute significantly to the quality of these lakes.

Table 1.1 LGD examples reported as percentage of the lake water balance and as absolute rates.

LGD as percentage of the lake water balance (%)	LGD rates
LGD represents 74% of all inflows to Williams Lake, Minnesota (Labaugh <i>et al.</i> , 1997).	477 L m ⁻² d ⁻¹ for Ashumet Pond, Massachusetts (McCobb <i>et al.</i> , 2009)
LGD represents 94% to Mary Lake, Minnesota (Stets <i>et al.</i> , 2010).	155 L m ⁻² d ⁻¹ for Dickson Lake, Ontario (Ridgway and Blanchfield, 1998)
LGD represents 90% to Cliff Lake, Montana (Gurrieri and Furniss, 2004).	138 L m ⁻² d ⁻¹ Shingobee Lake, Minnesota (Rosenberry <i>et al.</i> , 2000)
LGD represents 85% to Lake Annie, Florida (Sacks <i>et al.</i> , 1998)	

Although the main focus of the present PhD thesis is on LGD, GW discharge to streams is also considered in some chapters to compare it with LGD and to transfer knowledge from GW-SW interfaces in streams to GW-SW interfaces in lakes.

1.2 State of the Art: GW-SW interactions

1.2.1 Mechanisms of GW-SW interactions

In the unsaturated zone the soil pores are filled with air and water and in the saturated zone the soil pores are only filled with water. Water in the unsaturated zone usually percolates downwards to the saturated zone. Subsurface water in the saturated zone moves generally in the direction of the steepest hydraulic gradient. The upper part of the unsaturated zone is called soil-water zone. Water in that zone might be used by plants or evaporate to the atmosphere. The water in the saturated zone is called GW and the upper boundary of this zone is called water table. When the GW is connected to SW bodies the water table touches SW bodies at the shore or near the shore line (see Figure 1.1) (Winter *et al.*, 1998).

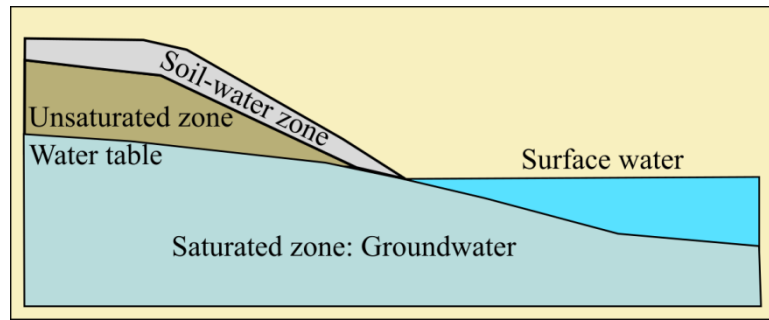


Figure 1.1 Unsaturated zone, saturated zone, GW and SW in freshwater systems (Taken and modified from Winter, 1998).

Flow across the GW-SW interface occurs in two directions. On the one hand, water can flow from the aquifer through the stream or lake bed into the stream or lake, respectively. This process is called exfiltration – a term which we define from the perspective of the aquifer (please note that other authors use a different definition and call the process which we call exfiltration, infiltration). Such streams are called gaining streams and in lakes the process is termed LGD. GW inflow into the stream or lake can occur at diffuse or at discrete localized inflow points (Winter, 1998; Lewandowski *et al.*, 2014). On the other hand, water can flow through the streambed or lake bed into the aquifer, this process is called infiltration and the system is called losing stream or losing lake, respectively (Winter *et al.*, 1998; Constantz and Stonestrom, 2003).

When GW discharges into SW (e.g. in streams or lakes) the chemical composition of the SW will be impacted by the differing chemical composition of the GW. In addition, when GW flows across the stream or lake bed various chemical reactions can take place that result in a change of the composition of the exfiltrating GW. When water infiltrates into the stream or lake bed the chemical composition of the SW will also impact the subsurface water in the HZ or lacustrine sediments (Constantz and Stonestrom, 2003).

1.2.2 Factors controlling GW-SW interactions

GW-SW interactions are mainly controlled by:

- Hydraulic head gradients between aquifer and stream/lake (Constantz and Stonestrom, 2003).
- Spatial distribution and variability of hydraulic conductivity of sediments in the HZ or lacustrine sediments and the underlying aquifer (Brunke and Gonser, 1997; Genereux *et al.*, 2008; Leek *et al.*, 2009; Angermann *et al.*, 2012a; Blume *et al.*, 2013).

In an unconfined aquifer the hydraulic head equals the water level. In a confined aquifer the hydraulic head equals the pressure. Subsurface water flows from higher to lower heads. At the stream or lake surface, the water pressure is zero as well as at all points on the water table (in unconfined aquifer conditions). In this manner, the elevation of the water table regarding the stream or lake surface will indicate the direction of the subsurface water flow between the stream/lake and the near-shore aquifer. For instance, if the stream or lake is gaining, that means that the elevation of the GW table is higher than the SW level. On the contrary, in losing stream reaches or sections of the lake, the elevation of the GW table will be lower than the stream or lake water level (Kalbus *et al.*, 2006). Both kinds of interaction might occur simultaneously in different parts of the stream or lake (Winter *et al.*, 1998).

Some other variables impacting on exchange flows are:

- Pressure changes due to the presence of geomorphological characteristics in the river bed: pool riffle series, changes in slope, ripples or woody debris (Elliott and Brooks, 1997; Tonina and Buffington, 2007; Cardenas, 2009) or pressure changes due to wave action and currents in lakes (Rosenberry *et al.*, 2013).
- The redistribution of sediments on the stream bed or lake bed also might play an important role regarding seepage rates. Sometimes, the sediments can clog the stream or lake bed leading to lower infiltration rates through the HZ or lacustrine sediments. They can also trap stream or lake water between their interstices and enhance interstitial water release into the stream or lake (Elliott and Brooks, 1997; Rosenberry *et al.*, 2010). Finally, due to wave action (e.g. during storm events), fine sediments in the shore of the lakes can be resuspended and settle again in deeper regions of the lake affecting seepage rates at the shore of the lake (Rosenberry *et al.*, 2015).
- Turbulence in the flowing stream water might induce upwelling and downwelling.
- Geological heterogeneities within the alluvial aquifer and GW discharge area. (Cardenas and Wilson, 2006; Fleckenstein *et al.*, 2006; Frei *et al.*, 2009; Engdahl *et al.*, 2010) or local geological conditions (Winter, 1999).
- Stream or lake position relative to GW flow systems (Winter, 1999; Woessner, 2000).

1.2.3 GW discharge in lakes

In lakes GW discharge rates are often small, there is lower turbulent mixing in the lake water than in the stream water and volume ratio between the water body in regards to the discharging GW, is higher than in streams. Under homogeneous conditions with homogeneous geology exchange flows are focused to near shore areas (Lewandowski *et al.*,

2014). The major reason is that flow lines approaching a lake bend upwards. An additional reason for higher GW release in near shore areas is the spatial distribution of fine grained and low permeability muddy material. The accumulation of muddy material is lower in areas close to shore since wave action influences the distribution of sediments within the lake. Sediments close to the shore will be easily resuspended and redistributed within the lake bed, while sediments in deeper parts of the lake won't be affected so intensively by wave action and therefore less resuspended and redistributed (Rosenberry *et al.*, 2015). This fact will lead to higher hydraulic conductivities near shore than offshore (McBride and Pfannkuch, 1975; Krabbenhoft *et al.*, 1990; Kishel and Gerla, 2002). Some other times, if the aquifer has hydraulically highly conductive areas, the GW will mainly flow through those areas following preferential flow paths into the lake. Sometimes, if the lake is set on fractured rocks it will show much localized LGD on the fractures of the rocks. Finally, lakes that are in contact with more than one aquifer might show high GW discharge rates below the aquitard layer (low permeability layer) separating both aquifers (Lewandowski *et al.*, 2014).

1.2.4 GW discharge in streams

The HZ is defined conceptually as the saturated interstitial zones under the streambed and in the stream bank that contains at least some parts of channel water (White *et al.*, 1993). Sometimes, low hydraulic conductivity streambed sediments inhibit GW upwelling and enhance horizontal pore water movement in the HZ since GW upwelling is inhibited by horizontal low-conductivity layers. Some other times, GW upwelling might be enhanced by high hydraulic conductivity of streambed sediments near confining riverbed structures, supplying a preferential flow path for rapid upwelling of semi-trapped GW (Angermann *et al.*, 2012a). The HZ in streams has been highlighted as an important ecohydrological interface with intense biogeochemical processes. It is characterized by high spatial and temporal heterogeneity in terms of sediment and discharge variability (Krause *et al.*, 2011; Lewandowski *et al.*, 2011).

1.3 Measurement methods for GW-SW interactions

Many methods exist to measure GW-SW interactions. The methods can be applied in the aquifer, in the SW, or in the HZ or lacustrine sediments. The methods vary in resolution, sampled volume and time scale. Usually, the choice of a method requires balancing between resolution, heterogeneities and sampled volumes. What is more, the scale of the method chosen might have a relevant impact on the results. The impact of the scale on measurements in heterogeneous media means that even if measurements are conducted with a dense grid of

points, the results obtained might be different from those obtained at larger scales due to the possibly large role of small-scale heterogeneities. For example, the role of small and high conductivity areas might be underestimated with point measurements (Kalbus *et al.*, 2006). As another example, GW discharge in streams and hyporheic exchange flow (HEF) might not be clearly distinguished when using the wrong scale. This is related to the high spatial variability of flow patterns on small spatial scales in the HZ or in lacustrine sediments (Schmidt *et al.*, 2006; Lewandowski *et al.*, 2011; Angermann *et al.*, 2012). Additional measurements are always advised to clearly determine the type of GW-SW interaction occurring in the HZ or lacustrine sediments (Kalbus *et al.*, 2006).

The research goal also has an important role when selecting the most appropriate methods to describe GW-SW interactions (Kalbus *et al.*, 2006) because it will determine the scale at which techniques for measurements of GW-SW interactions are applied. For instance, for regional studies large scale techniques are more appropriate. On the contrary, for process studies high resolution measurements might be needed. Of course all methods have their own limitations and uncertainties. For instance, at stream reach scales a high density measuring network is needed which takes into account small scale patterns of flow (Schmidt *et al.*, 2006). Unfortunately that requires high device and measurement efforts. As a result, these measurements are usually constrained to small spatial scales. For these reasons, there is a requirement for inexpensive and quantitative methods which allow describing the spatial heterogeneity of GW-SW interactions more adequately. Under ideal conditions, GW-SW interactions should be characterized by a high amount of measurements (high temporal resolution) with high spatial accuracy (Schmidt *et al.* 2006).

Several authors (Palmer *et al.*, 1993; White *et al.*, 1993; Kalbus *et al.*, 2006; Schmidt *et al.*, 2006; Krause *et al.*, 2011) have stated the need of multi-dimensional research methods which could cope with several spatial and temporal scales in order to adequately describe GW-SW interactions in aquatic ecosystems. A multi scale approach bringing together different techniques can substantially decrease uncertainties and improve estimates of water fluxes between GW-SW interfaces (Kalbus *et al.*, 2006). For instance, Blume *et al.* (2013) combined LGD rates derived from temperature lances or vertical hydraulic gradients (VHG) with 2-D patterns of lake bed temperatures monitored by fiber optic distributed temperature sensing (FO-DTS) for successful upscaling of LGD.

Therefore, the right selection of methods is of major importance for getting useful data (Kalbus *et al.*, 2006) to describe GW-SW interactions. For instance, GW-SW interactions can be followed by monitoring the chemical composition of the water that is exchanged. The flow

path can be followed at different scales, from small to catchment scale (Constantz and Stonestrom, 2003). Another method for tracing water flow is heat tracing. Natural variations of temperature in areas close to the stream or lake environment are easy to track since temperature can be easily measured during specific seasons and when exchange is fast (Anderson, 2005).

In addition to the **scale**, the **research goal** and the selection of the most adequate **method** are three key steps to characterize GW-SW interactions in freshwater bodies. Conant Jr (2004) and Keery *et al.* (2007) advise the development of a **conceptual model** that considers the main mechanisms that influence water flow across GW-SW interfaces.

Regarding the main focus of interest of the present PhD thesis, which is LGD, Lewandowski *et al.* (2014) listed methods for LGD detection in three different groups:

- Spatially specific methods which measure LGD rates in one point or over a small area, for instance seepage meters (Lee, 1977), sediment temperature depth profiles (Schmidt *et al.*, 2006).
- Integrating methods that quantify the entire GW inflow into a lake e. g. radon balances (Kluge *et al.*, 2007), stable isotope methods (Hofmann *et al.*, 2008), annual GW recharge in the subsurface catchment by modelling or computation of the water budget.
- Identification of discharge patterns without quantification of LGD such as fiber optic distributed temperature sensing (FO-DTS) (Selker *et al.*, 2006b), geophysical approaches around the lake perimeter (Ong *et al.*, 2010), airborne measurements of thermal infrared radiation (TIR) (Lewandowski *et al.*, 2013).

In the present PhD thesis, methods based on heat as a tracer to study GW-SW interaction in stagnant waters (or LGD) will be the main focus of interest.

1.4 Heat as a natural tracer of GW-SW interactions

Natural heat tracing techniques allow monitoring the heat transported by groundwater or surface water (Constantz and Stonestrom, 2003). The use of heat as a tracer for GW-SW interactions, is based on the fact that GW temperatures are more or less stable throughout the year whereas stream or lake temperatures change daily and seasonally (Kalbus *et al.*, 2006). Relevant differences between GW and SW temperatures can be observed during summer and winter periods (Meinikmann *et al.*, 2013) at the sediment profile of stream and lake beds and at the water body.

1.4.1 Heat tracing in stream and lake beds

Measurements of stream or lake bed temperatures can be used if there are large GW-SW temperature differences. The results can be used to observe the propagation of the heat signal through the sediment bed and to determine flow directions within the sediment (Anderson, 2005; Keery *et al.*, 2007; Schmidt *et al.*, 2007; Anibas *et al.*, 2009; Hatch *et al.*, 2010) to determine GW discharge or recharge areas (Kalbus *et al.*, 2006) or to compute exchange fluxes (Westhoff *et al.*, 2007; Hatch *et al.*, 2010).

Stream/lake bed heat transfer is governed by three processes (Hannah *et al.*, 2004; Constantz, 2008; Webb *et al.*, 2008):

1. Advective or convective (free or forced) heat transfer
2. Conductive heat transfer
3. Radiative heat transfer

The horizontal and vertical distribution of heat in stream/lake beds is due to heat transport by moving water (advective heat flow) and by heat or thermal conduction across the solid and fluid phase of the sediments (conductive heat flow) (Constantz and Stonestrom, 2003; Schmidt *et al.*, 2007). The terms “advective heat transfer” and “convective heat transfer” are used interchangeably in hydrology (Anderson, 2005). Sometimes convective heat transfer is defined as heat transfer by moving water when water flows above the stream/lake bed in order to differentiate advective and convective heat transfer processes (Constantz, 2008). In the present PhD thesis, advective and convective heat transfer processes are considered synonyms. To avoid confusion only one term is used. Free convection is understood as the heat transfer by flow driven due to density differences in response to temperature differences (e.g. in freshwater systems). Forced convection is heat transfer due to flow driven by other mechanisms. For instance, forced convection is a common phenomenon in GW systems where heat is transported by the movement of GW by recharge or discharge processes (Anderson, 2005). Radiative heat transfer takes place when sun radiation is absorbed by the water body or the sediment bed of the water body (Constantz, 2008).

The three dimensional heat transport equation

The three dimensional heat transport equation (eq.1) defines the heat transport by conduction and by GW movement (advection or convection) (Anderson, 2005). The first term of the equation refers to transport of heat by conduction and thermal dispersion. The second term of the equation refers to heat transport by moving water (advection/convection) (Anderson, 2005).

$$\frac{\kappa_e}{\rho c} \nabla^2 T - \frac{\rho_w c_w}{\rho c} \nabla \cdot (T q) = \frac{\partial T}{\partial t} \quad (\text{eq.1})$$

Where:

T = temperature.

t = time.

ρ_w = density of water.

c_w = specific heat of water.

ρ = density of the rock fluid matrix.

c = specific heat of the rock fluid matrix.

q = seepage velocity.

κ_e = effective thermal conductivity of the rock fluid matrix.

The temperature profile within the stream and lake bed

Surface water is heated or cooled at the water surface. Therefore, downward water flow through the sediment (loosing reaches and lakes) provokes a deeper spread of cyclic temperature variations (Winter *et al.*, 1998). Inversely, if the water flow is upward (gaining reaches and lakes), cyclic temperature changes do not spread as deep into the aquifer as in the case of the downwelling flow due to the more constant temperature of upwelling GW (Kalbus *et al.*, 2006) (see Figure 1.2).

Vertical temperature profiles within the stream or lake bed sediments depend on advective and conductive heat exchange across GW-SW interfaces. Among the infiltration gradient the thermal amplitude decreases with depth, with increasing temperatures in winter and decreasing temperatures in summer (Stonestrom and Constantz, 2003) (see Figure 1.2, red lines). Moreover, there is no quick variation in temperature and the changes become delayed and softened with increasing depth and distance from the infiltration area (Brunke and Gonser, 1997). Finally, the curvature of temperature gradients in the sediment close to the interface shows the direction and intensity of vertical GW exchange (Meinikmann *et al.*, 2013) (see Figure 1.2).

Monitoring temperature time series in the stream/lake bed and nearby sediments allows delineating the main flow regime (Constantz and Stonestrom, 2003; Kalbus *et al.*, 2006; Constantz, 2008) in the stream and lake bed. In addition, the three dimensional heat transport equation (eq. 1) can be applied to monitored temperature profiles to calculate LGD rates in lakes or exfiltration rates in streams, respectively (Schmidt *et al.*, 2006).

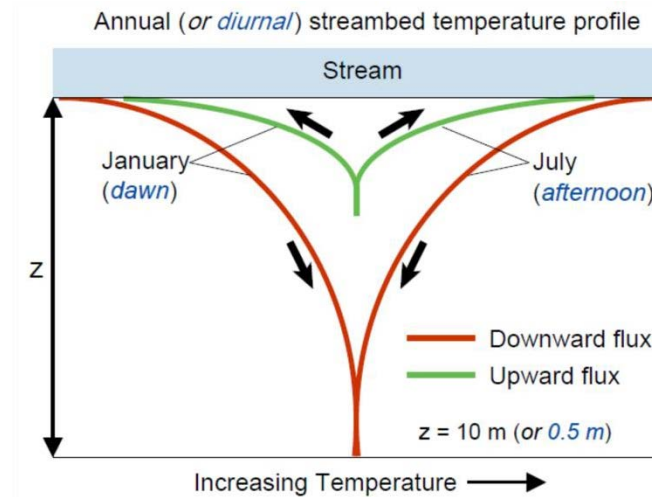


Figure 1.2 Sediment temperatures against depth (z): for gaining and losing conditions (green and red lines respectively) and for daily (in italic) or annual cycles. For annual cycles the depth at which the temperature reaches a constant value can be 10 m or more at downward flow. On the contrary, the depth at which the temperatures reach constant values at upward flows can be less than 1 meter. Taken from Constantz and Stonestrom (2003).

1.4.2 Heat tracing in the water column

Heat transport through the water column is caused by different factors compared to heat transport through the HZ or lacustrine sediments, where the presence of sediment affects how transport of heat occurs. For instance, in Ouellet *et al.* (2014) the heat budget of a water column in a pool under controlled environment conditions was conducted. In that study, advection and bottom fluxes were excluded (for instance heat fluxes that would occur in natural conditions related to discharge of GW from the stream or lake bed to the SW) in order to observe other heat fluxes related to weather conditions. In Ouellet *et al.* (2014), the atmospheric long wave radiation and surface long wave radiation are the largest components during day and night compared to shortwave radiation, convection, evaporation, precipitation and heat from the pool bottom (Ouellet *et al.*, 2014). Therefore, the radiative components of the heat budget equation appeared to control the main sources and sinks of heat in the water column. In addition, the wind component is relevant for the computation of the latent heat flux (Ouellet *et al.*, 2014). Another research by Benyahya *et al.* (2012), monitored various radiation components at stream scale considering the microclimate conditions at that same stream site. On the one hand, it was found that energy gains in the stream were driven mainly by solar radiation flux and to a less extent by net longwave radiation. On the other

hand, it was found that energy losses in the stream were mainly attributed to net longwave radiation and evaporation (Benyahya *et al.*, 2012).

The results showed in Ouellet *et al.* (2014) and Benyahya *et al.* (2012) indicate that the net radiation balance (net short- and net long-wave radiation on the water surface) is an important factor controlling water column temperatures. Therefore, when monitoring small scale GW-SW interactions (for instance discrete discharge of GW from the stream or lake bed) at broader scales (for instance from the more accessible water surface of streams or lakes) with heat tracing techniques, different radiation components could have an impact on the heat tracing of GW-SW interactions in streams and lakes.

Upwards directed groundwater flow is often called upwelling, especially when considering the HZ, where generally, upwelling and downwelling occur along river reaches. In the present PhD thesis the term upwelling is only used for upward transport processes in the water column; this definition is borrowed from limnophysics. The above-mentioned processes in the HZ are called gaining and losing in the present thesis.

In marine systems, GW upwelling can be more intense than in freshwater systems. The main reason is the large density differences between discharging fresh GW and the saline SW. Thus, the buoyancy of GW in marine systems is not dependent on temperatures alone but mainly on salinity differences between GW and the saline SW (Lewandowski *et al.*, 2013). In contrast, buoyancy of GW in freshwater systems (non-saline) is mainly dependent on temperature differences between GW and SW. In this manner, small temperature differences between GW and SW in non-saline systems may result in small density differences between GW and SW leading to GW upwelling intensities much smaller than in saline systems (Lewandowski *et al.*, 2013). Nevertheless, temperature-induced buoyancy of GW might allow the detection of GW upwelling at the surface of freshwater systems. Still, the ability of TIR imaging to detect GW upwelling at the water surface in freshwater systems can differ fundamentally from marine systems, because GW-SW temperature differences change considerably both seasonally and diurnally. For those reasons, detection of submarine groundwater discharge (SGD) using remote sensing, for instance thermal infrared (TIR) imaging, is generally much easier than detection of GW discharge in freshwater systems, for instance in lakes (Lewandowski *et al.*, 2014).

While research on detection of SGD by TIR imaging is broad and well documented, there is little research on detection of GW discharge in freshwater systems. Moreover, within freshwater systems most of the publications (Tcherepanov *et al.*, 2005; Danieleescu *et al.*,

2009; Briggs *et al.*, 2013, 2016b; Dugdale *et al.*, 2015; Wawrzyniak *et al.*, 2016) that have used TIR imaging for detection of GW, focused on the detection of cool temperature anomalies during summer and in streams. The detection of GW-SW interactions by TIR imaging, in lakes and during winter, has received very little attention. For instance, in Lewandowski *et al.* (2013), high GW discharge rates calculated from temperature data monitored by temperature lances at the shore of Lake Arendsee were related to warm water areas at the water surface of Lake Arendsee detected with airborne TIR imaging. However, further research demonstrated that observed warm temperature patterns by TIR imaging at the water surface of Lake Arendsee were related to wind-driven upwelling of cold water (Pöschke *et al.*, 2015). This example highlights the need for understanding how the heat signal of the upwelling GW travels across the water column and how it spreads at the water surface in freshwater systems, especially in lakes.

Natural heat transport processes occurring within the sediment of stream or lake beds, differ from natural heat transport processes that occur in the water column and at the water surface (see sections 1.4.2. to 1.4.5). Therefore, GW-SW interactions traced with heat tracing techniques across the sediment (stream or lake bed) might not always correspond to thermal anomalies detected by heat tracing techniques at the water surface of streams or lakes. In this respect, there is a need for more research on heat tracing of GW-SW interactions across the water column and at the water surface.

1.5 Scaling in hydrology

Hydrological processes occur at different scales, for instance, from unsaturated flow in a 1 m soil profile to big floods in river systems of a million square km, same for the temporal scale, from flashfloods (minutes of duration) to flow in aquifers (hundreds of years) (Blöschl and Silvapalan, 1995). Models and theories developed at small scales are pretended to be suitable for larger scales and inversely, large scale models or data are used to get predictions for smaller scales. This procedure requires extrapolation or transfer of information through scales. This process is called scaling and problems related to it are called scaling issues. Under ideal conditions, processes should be observed at the scale they occur. But this is not always possible (Blöschl and Silvapalan, 1995). Therefore, the choice of the right spatial and temporal scale is critical since the site and time of the year (or even time of the day) where and when the measurements are done can strongly influence the results. In addition, it is very important to carefully consider possible scaling issues when designing experiments,

especially if extrapolating the results to broader scales such as streams, lakes or catchments (Palmer 1993).

Within hydrology scaling has been long discussed during the last decades (Jelinski and Wu, 1996; Gardner, 1998; Burnett and Blaschke, 2003). Various strategies and methods have been proposed and used as an attempt to solve the scaling issue and develop a new paradigm (Wu and Loucks, 1995; Marceau and Hay, 1999; Wu, 1999). However, it is still one of the main challenges in hydrology as well as in other natural and social science fields.

Multiple authors have suggested scale definitions for hydrological systems aiming to describe and understand hydrological processes across scales. For instance, Tóth (1963) grouped GW in GW flow systems (for unconfined aquifers until few hundred square km with low slope and a low rate outlet stream): Tóth (1963) defined three different flow system scales: local, intermediate and regional. These ideas are now broadly accepted and used in general terms (Winter *et al.*, 1998; Winter, 1999; Brinson *et al.*, 2002; Devito *et al.*, 2005). Larkin and Sharp (1992), Brunke and Gonser (1997) and Woessner (2000) differentiated two scales of water exchange in riparian areas: large scale processes affecting entire riparian aquifers where flow paths linking the systems are defined mainly by geological features of the catchment, and local scale exchange processes in the hyporheic zone (part of the fluvial system and aquifer system is functionally ruled by river stage, hydraulic features and topography of the stream bed) (Dahl *et al.*, 2007). In addition, Dahl *et al.* (2007) mentioned the need to monitor and characterize GW-SW interactions at different scales: sediment scale (< 1 m); reach scale (1 – 1000 m); and catchment scale (> 1000 m). Since the scale boundaries or thresholds are arbitrary, the key issue is that the hierarchic organization of GW-SW interactions should be symmetric or equal to the hierarchic organization of GW flow systems. In this manner, a local flow system refers to the reach scale and a regional flow system refers to the catchment scale. HZ processes refer to the sediment scale (Dahl *et al.*, 2007).

However, despite the various suggestions for scale definitions and monitoring at those scales, there is no broadly accepted generic scaling method or generic conceptual model for scaling of GW-SW interactions in freshwater environments. This is mainly because GW-SW interactions are characterized by large heterogeneities and scaling issues (Woessner, 2000; Becker *et al.*, 2004; Kalbus *et al.*, 2008; Krause *et al.*, 2011; Lewandowski *et al.*, 2011). The spatio-temporal distribution of GW-SW interactions is complex (Lewandowski *et al.*, 2011) due to the different scales relevant for GW-SW interactions, layering of stream or lake beds (Marion *et al.*, 2008), heterogeneities in alluvial geology (Fleckenstein *et al.*, 2006) and the

temporal variability of the driving factors. This is one of the main reasons for the knowledge gap on interpreting the hydrology of GW-SW interactions at different scales (Krause *et al.*, 2011; Anibas *et al.*, 2012; Lewandowski *et al.*, 2014).

For instance, point measurements are only representative for the specific local conditions and processes. Therefore, to cover a large area, a huge amount of labor intensive measurements is needed followed by an extrapolation of these measurements in order to get an overall image of the entire system, since GW-SW interaction occurs at multiple scales (Kidmose *et al.*, 2011). In addition, measurements on GW-SW interactions show large uncertainties (Blume *et al.*, 2013). For instance, some studies about lake water balances and nutrient budgets usually don't have proper information about the spatial patterns of seepage fluxes through the aquifer-lake interface, constraining the reliability of the results of those studies (Blume *et al.*, 2013). Indeed, uncertainty regarding determination of exchange flow patterns rises with larger spatial scales (White *et al.*, 1993; Kasahara and Wondzell, 2003; Krause *et al.*, 2009, 2011). Even in latest research, such as by Lautz and Ribaudó (2012) it is still remarked that methods used to describe hyporheic exchange at reach scale are not yet spatially precise enough to locate and describe hyporeic exchange flow (HEF).

Since spatial scaling refers to a widening or narrowing of the area under consideration where GW-SW interactions occurring at one scale can be observed in a wider or narrower environmental context, heterogeneities of factors controlling GW-SW interactions might increase or decrease, respectively. Thus, the understanding of GW-SW interactions may improve by being aware and by consideration of the heterogeneities of factors controlling GW-SW interactions when applying multiple approaches over a range of scales. Therefore, there is a need for: 1) methods and approaches that would allow the identification of controlling factors of GW-SW interactions and 2) scaling techniques to better understand the functioning of GW-SW interactions over a range of scales (Krause *et al.*, 2011). For instance, distributed sensor technology or adaptive modeling approaches suggested by Krause *et al.* (2011) or remote sensing data, are promising technology that can offer rapid and interesting gains and insights on GW-SW interactions (Stewart *et al.*, 1998).

Finally, most of the research on scaling of GW-SW interactions is focused on the HZ or on stream-aquifer interfaces (Fleckenstein *et al.*, 2006; Anibas *et al.*, 2012; Kikuchi *et al.*, 2012; Lautz and Ribaudó, 2012; Mouhri *et al.*, 2013; Boano *et al.*, 2014) whereas there is less research on scaling of GW-SW interactions in lakes (Kidmose *et al.*, 2011; Blume *et al.*, 2013). Signal propagation and scaling of GW-SW interactions across various interfaces such as: sediment-water interface -> water column -> water surface-atmosphere interface, has not

been broadly considered. GW-SW interactions are most of the time studied in the sediment or at the sediment surface. Nevertheless, remote sensing technology provides now the opportunity for observation of GW-SW interactions at different spatial scales and at different interfaces (e.g. water surface-atmosphere).

1.5.1 Can we learn from other disciplines?

In landscape science, when creating a method for landscape monitoring and analysis, a conceptual understanding of the architecture and functioning of the ecological systems is necessary (Müller, 1997). More specifically, a conceptual model can characterize the fundamental functions and behaviors of SW and GW systems in a catchment. It can describe the actual understanding of the processes, linkages and effects on the water source (Brodie *et al.*, 2007). It seems that, a conceptual framework should be the basis for field researches and development of predictive models (Brodie *et al.*, 2007). Palmer *et al.* (1993) and White *et al.* (1993) also suggested the development of interdisciplinary multi-scale conceptual frameworks combined with more communication between different scientific fields in order to solve the scaling issue in hydrology. In addition, Blöschl and Silvapalan (1995) suggested that combining theoretical concepts with engineering solutions would be suitable for filling the gap between theory (e.g. conceptual understanding) and practice (measurement campaigns). For example, Hierarchy Theory (Simon, 1962; Koestler, 1967; O'Neill *et al.*, 1989; Wu, 1999) provides a conceptual framework for connecting processes at different scales. However, the creation of operational hierarchies and upscaling of GW-SW interactions is still not a common approach in the field of hydrology. The combination of Hierarchy Theory and Patch Dynamics (from landscape science (Forman, 1995; Johnson and Gage, 1997; Wu, 1999; Poole and Berman, 2001)) results in Hierarchical Patch Dynamics (HPD) (Wu and Loucks, 1995). These concepts will be broadly introduced in Chapter 2: *Scaling on temperature tracers for water and heat exchange processes in ecohydrological interfaces*. By HPD theory, the architecture of an ecological system can be defined and adapted to each environment, in order to use it as a leader for scaling processes.

By using the main idea of the HPD theory a conceptual model or conceptual guideline can be designed in order to use it as a scaling tool and as a conceptual framework for the data (or observations) obtained with heat tracing techniques in order to describe patterns and processes related to GW-SW interaction over several spatial scales and across GW-SW interfaces (sediment-water interface, water column, water surface-atmosphere interface).

1.6 Hypothesis and aims of this PhD thesis

There is a need for an integrated multi-scale approach that can upscale GW-SW interactions over several spatial scales and across different ecohydrological interfaces. The main goal of the present PhD thesis is to upscale heat and water exchange processes related to LGD, from the sediment-water interface through the water column to the water surface-atmosphere interface.

Based on the central hypothesis of this PhD thesis:

‘The positive buoyancy of warm GW causes upwelling across the cold water column during winter and allows the detection of LGD at the water surface by TIR.’

an integrated approach (GW-SW-atmosphere interactions) that considers the use of fiber optic distributed temperature sensing (FO-DTS) and thermal infrared (TIR) imaging at different spatial scales (multi-scale approach) is developed. This approach aims:

1. to provide a conceptual framework based on HPD that identifies and quantifies heat and water exchange fluxes over several spatial and temporal scales and across ecohydrological interfaces in freshwater environments (Chapter 2: *Scaling of temperature tracers for water and heat exchange processes at ecohydrological interfaces.*).
2. to describe how interactions between discharging GW, upwelling warm water and cold SW occur in lakes, in terms of spatial and temporal distribution of temperature through the water column by FO-DTS and TIR (Chapter 3: *Mesocosm experiments identifying hotspots of groundwater upwelling in a water column by fiber optic distributed temperature sensing* and Chapter 4: *Thermal infrared imaging for detection of groundwater at the surface of stagnant water bodies*).
3. to identify the main parameters controlling whether it is possible to detect GW-SW interactions at the water surface of stagnant water bodies such as lakes by heat tracing techniques, in this case FO-DTS and TIR (Chapter 3 and Chapter 4).

1.7 References

- Anderson MP. 2005. Heat as a ground water tracer. *Ground water* **43** (6): 951–68 DOI: 10.1111/j.1745-6584.2005.00052.x
- Angermann L, Krause S, Lewandowski J. 2012. Application of heat pulse injections for investigating shallow hyporheic flow in a lowland river. *Water Resources Research* **48** (October): 1–16 DOI: 10.1029/2012WR012564
- Anibas C, Fleckenstein JH, Volze N, Buis K, Verhoeven R, Meire P, Batelaan O. 2009. Transient or steady-state? Using vertical temperature profiles to quantify groundwater–surface water exchange. *Hydrological Processes* **23**: 2165–2177 DOI: 10.1002/hyp.7289
- Anibas C, Verbeiren B, Buis K, Chormański J, De Doncker L, Okruszko T, Meire P, Batelaan O. 2012. A hierarchical approach on groundwater-surface water interaction in wetlands along the upper Biebrza River, Poland. *Hydrology and Earth System Sciences* **16**: 2329–2346 DOI: 10.5194/hess-16-2329-2012
- Baron JS, Poff NL, Angermeier PL, Clifford ND, Gleick PH, Hairston NG, Jackson RB, Johnston CA, Richter BD, Steinman AD. 2002. Meeting ecological and societal needs for freshwater
- Bartel H, Dieter HH, Feuerpfeil I, Grummt HJ, Grummt T, Hummel A, Konietzka R, Litz N, Rapp T, Rechenberg J, et al. 2016. *Rund um das Trinkwasser*. Dessau-Roßlau. Available at: http://www.umweltbundesamt.de/sites/default/files/medien/479/publikationen/uba_rund_um_das_trinkwasser_ratgeber_web_0.pdf
- Becker MW, Georgian T, Ambrose H, Siniscalchi J, Fredrick K. 2004. Estimating flow and flux of ground water discharge using water temperature and velocity. *Journal of Hydrology* **296** (1–4): 221–233 DOI: 10.1016/j.jhydrol.2004.03.025
- Benyahya L, Caissie D, Satish MG, El-jabi N. 2012. Long-wave radiation and heat flux estimates within a small tributary in Catamaran Brook (New Brunswick , Canada). **484** (May 2011): 475–484 DOI: 10.1002/hyp.8141
- Blöschl G, Silvapalan M. 1995. Scale Issues in Hydrological Modeling. *Hydrological processes* **9**: 251–290 DOI: 10.1029/96EO00131
- Blume T, Krause S, Meinikmann K, Lewandowski J. 2013. Upscaling lacustrine groundwater discharge rates by fiber-optic distributed temperature sensing. *Water Resources Research* **49** (October 2012): 7929–7944 DOI: 10.1002/2012WR013215
- Boano F, Harvey JW, Marion A, Packman AI, Revelli R, Ridolfi L, Wörman A. 2014. Hyporheic flow and transport processes: Mechanisms, models, and biogeochemical

- implications. *Reviews of Geophysics*: 1–77 DOI: 10.1002/2012RG000417. Received
- Briggs MA, Hare DK, Boutt DF, Davenport G, Lane JW. 2016. Thermal infrared video details multiscale groundwater discharge to surface water through macropores and peat pipes. *Hydrological Processes* **30** (14): 2510–2511 DOI: 10.1002/hyp.10722
- Briggs MA, Voytek EB, Day-Lewis FD, Rosenberry DO, Lane JW. 2013. Understanding water column and streambed thermal refugia for endangered mussels in the Delaware River. *Environmental Science and Technology* **47** (20): 11423–11431 DOI: 10.1021/es4018893
- Brinson MM, MacDonnell LJ, Austen DJ, Beschta RL, Dillaha TA, Donahue DL, Gregory S V, Harvey JW, Molles Jr MC, Rogers EI. 2002. Riparian areas: functions and strategies for management. *National Academy of Sciences, Washington DC* **444**
- Brodie R, Sundaram B, Tottenham R, Hostetler S, Ransley T. 2007. An Adaptive Management Framework for Connected Groundwater-Surface Water Resources in Australia. Canberra.
- Brunke M, Gonser T. 1997. The ecological significance of exchange processes between rivers and groundwater. *Freshwater Biology* **37**: 1–33 DOI: 10.1046/j.1365-2427.1997.00143.x
- Burnett C, Blaschke T. 2003. A multi-scale segmentation/object relationship modelling methodology for landscape analysis. *Ecological Modelling* **168**: 233–249 DOI: 10.1016/S0304-3800(03)00139-X
- Cardenas BM, Wilson JL. 2006. The influence of ambient groundwater discharge on exchange zones induced by current-bedform interactions. *Journal of Hydrology* **331** (1–2): 103–109 DOI: 10.1016/j.jhydrol.2006.05.012
- Cardenas MB. 2009. Stream-aquifer interactions and hyporheic exchange in gaining and losing sinuous streams. *Water Resources Research* **45** (6): 1–13 DOI: 10.1029/2008WR007651
- Conant Jr B. 2004. Delineating and Quantifying Ground Water Discharge Zones Using Streambed Temperatures. *Ground water* **42** (2): 243–257 DOI: 10.1111/j.1745-6584.2004.tb02671.x
- Constantz J. 2008. Heat as a tracer to determine streambed water exchanges. *Water Resources Research* **44**: 1–20 DOI: 10.1029/2008WR006996
- Constantz J, Stonestrom D a. 2003. Heat as a tracer of water movement near streams. In *Heat as a Tool for Studying the Movement of Ground Water near Streams*, Stonestrom DA, , Constantz J (eds). Reston, Virginia; 1–6. Available at: <http://pubs.usgs.gov/circ/2003/circ1260/#pdf>

- Dahl M, Nilsson B, Langhoff JH, Refsgaard JC. 2007. Review of classification systems and new multi-scale typology of groundwater-surface water interaction. *Journal of Hydrology* **344**: 1–16 DOI: 10.1016/j.jhydrol.2007.06.027
- Danielescu S, MacQuarrie K. TB, Faux RN. 2009. The integration of thermal infrared imaging, discharge measurements and numerical simulation to quantify the relative contributions of freshwater inflows to small estuaries in Atlantic Canada. *Hydrological Processes* **23**: 2847–2859 DOI: 10.1002/hyp.7383
- Devito K, Creed I, Gan T, Mendoza C, Petrone R, Silins U, Smerdon B. 2005. A framework for broad-scale classification of hydrologic response units on the Boreal Plain: Is topography the last thing to consider? *Hydrological Processes* **19** (8): 1705–1714 DOI: 10.1002/hyp.5881
- Dugdale SJ, Bergeron NE, St-Hilaire A. 2015. Spatial distribution of thermal refuges analysed in relation to riverscape hydromorphology using airborne thermal infrared imagery. *Remote Sensing of Environment* **160**: 43–55 DOI: 10.1016/j.rse.2014.12.021
- EC. 2000. Directive 2000/60/EC of the European Parliament and of the Council of 23 October 2000 establishing a framework for Community action in the field of water policy DOI: 10.1039/ap9842100196
- Elliott H, Brooks NH. 1997. Transfer of nonsorbing solutes to a streambed with bed forms : Theory permeable streambed and the overlying water of a stream or river is presented in this In a companion paper this issue] the results of experimental $q(x) = U \cdot$ **33** (1): 123–136
- Engdahl NB, Vogler ET, Weissmann GS. 2010. Evaluation of aquifer heterogeneity effects on river flow loss using a transition probability framework. *Water Resources Research* **46** (1): 1–13 DOI: 10.1029/2009WR007903
- European Environmental Agency. 2015. Freshwater quality. *SOER 2015*: 1–4 Available at: <https://www.eea.europa.eu/soer-2015/europe/freshwater#tab-based-on-indicators> [Accessed 22 November 2017]
- Fleckenstein JH, Krause S, Hannah DM, Boano F. 2010. Advances in Water Resources Groundwater-surface water interactions: New methods and models to improve understanding of processes and dynamics. *ADWR* **33** (11): 1291–1295 DOI: 10.1016/j.advwatres.2010.09.011
- Fleckenstein JH, Niswonger RG, Fogg GE. 2006. River-aquifer interactions, geologic heterogeneity, and low-flow management. *Ground Water* **44** (6): 837–852 DOI: 10.1111/j.1745-6584.2006.00190.x

- Forman RTT. 1995. Some general principles of landscape and regional ecology. *Landscape Ecology* **10** (3): 133–142 DOI: 10.1007/BF00133027
- Frei S, Fleckenstein JH, Kollet SJ, Maxwell RM. 2009. Patterns and dynamics of river-aquifer exchange with variably-saturated flow using a fully-coupled model. *Journal of Hydrology* **375** (3–4): 383–393 DOI: 10.1016/j.jhydrol.2009.06.038
- Frei S, Knorr KH, Peiffer S, Fleckenstein JH. 2012. Surface micro-topography causes hot spots of biogeochemical activity in wetland systems : A virtual modeling experiment. *Journal of Geophysical Research* **117** (August): 1–18 DOI: 10.1029/2012JG002012
- Gardner RH. 1998. Pattern, process, and the analysis of spatial scales. *Ecological Scale. Colombia University Press, New York*: 17–34
- Genereux DP, Leahy S, Mitsova H, Kennedy CD, Corbett DR. 2008. Spatial and temporal variability of streambed hydraulic conductivity in West Bear Creek, North Carolina, USA. *Journal of Hydrology* **358** (3–4): 332–353 DOI: 10.1016/j.jhydrol.2008.06.017
- Gurrieri JT, Furniss G. 2004. Estimation of groundwater exchange in alpine lakes using non-steady mass-balance methods. *Journal of Hydrology* **297**: 187–208 DOI: 10.1016/j.jhydrol.2004.04.021
- Hannah DM, Malcolm IA, Soulsby C, Youngson AF. 2004. Heat exchanges and temperatures within a salmon spawning stream in the Cairngorms, Scotland: Seasonal and sub-seasonal dynamics. *River Research and Applications* **20** (6): 635–652 DOI: 10.1002/rra.771
- Hatch CE, Fisher AT, Ruehl CR, Stemler G. 2010. Spatial and temporal variations in streambed hydraulic conductivity quantified with time-series thermal methods. *Journal of Hydrology* **389** (3–4): 276–288 DOI: 10.1016/j.jhydrol.2010.05.046
- Hofmann H, Knöller K, Lessmann D. 2008. Mining lakes as groundwater-dominated hydrological systems: assessment of the water balance of Mining Lake Plessa 117 (Lusatia, Germany) using stable isotopes. *Hydrological Processes* **22**: 4620–4627 DOI: 10.1002/hyp.7071
- Jelinski DE, Wu J. 1996. The modifiable areal unit problem and implications for landscape ecology. *Landscape Ecology* **11** (3): 129–140 DOI: 10.1007/BF02447512
- Johnson LB, Gage SH. 1997. Landscape approaches to the analysis of aquatic ecosystems. *Freshwater Biology* **37**: 113–132 DOI: 10.1046/j.1365-2427.1997.00156.x
- Kalbus E, Reinstorf F, Schirmer M. 2006. Measuring methods for groundwater, surface water and their interactions: a review. *Hydrology and Earth System Sciences Discussions* **3** (4): 1809–1850

- Kalbus E, Schmidt C, Molson JW, Reinstorf F, Schirmer M. 2008. Influence of aquifer and streambed heterogeneity on the distribution of groundwater discharge. *Hydrology and Earth System Sciences Discussions* **5** (4): 2199–2219 DOI: 10.5194/hessd-5-2199-2008
- Kasahara T, Wondzell SM. 2003. Geomorphic controls on hyporheic exchange flow in mountain streams. *Water Resources Research* **39** (1): 1–14 DOI: 10.1029/2002WR001386
- Keery J, Binley A, Crook N, Smith JWN. 2007. Temporal and spatial variability of groundwater-surface water fluxes: Development and application of an analytical method using temperature time series. *Journal of Hydrology* **336**: 1–16 DOI: 10.1016/j.jhydrol.2006.12.003
- Kidmose J, Engesgaard P, Nilsson B, Laier T, Looms MC. 2011. Spatial Distribution of Seepage at a Flow-Through Lake: Lake Hampen, Western Denmark. *Vadose Zone Journal* **10** (1): 110 DOI: 10.2136/vzj2010.0017
- Kikuchi CP, Ferrè TPA, Welker JM. 2012. Spatially telescoping measurements for improved characterization of ground water-surface water interactions. *Journal of Hydrology* **446–447**: 1–12 DOI: 10.1016/j.jhydrol.2012.04.002
- Kishel HF, Gerla PJ. 2002. Characteristics of preferential flow and groundwater discharge to Shingobee Lake, Minnesota, USA. *Hydrological Processes* **16** (10): 1921–1934 DOI: 10.1002/hyp.363
- Kluge T, Ilmberger J, von Rohden C, Aeschbach-Hertig W. 2007. Tracing and quantifying groundwater inflow into lakes using radon-222. *Hydrology and Earth System Sciences Discussions* **4** (3): 1519–1548 DOI: 10.5194/hessd-4-1519-2007
- Koestler AG. 1967. *The ghost in the machine*.
- Krabbenhoft DP, Anderson MP, Bowser CJ. 1990. Estimating groundwater exchange with lakes: 2. Calibration of a three-dimensional, solute transport model to a stable isotope plume. *Water Resources Research* **26** (10): 2455–2462 DOI: 10.1029/WR026i010p02455
- Krause S, Hannah DM, Fleckenstein JH. 2009. Hyporheic hydrology: interactions at the groundwater-surface water interface. *Hydrological Processes* **23**: 2103–2107 DOI: 10.1002/hyp.7366
- Krause S, Hannah DM, Fleckenstein JH, Heppell CM, Kaeser D, Pickup R, Pinay G, Robertson AL, Wood PJ. 2011. Inter-disciplinary perspectives on processes in the hyporheic zone. **499** (November 2010): 481–499 DOI: 10.1002/eco
- Krause S, Lewandowski J, Grimm NB, Hannah DM, Pinay G, McDonald K, Martí E,

- Argerich A, Pfister L, Klaus J, et al. 2017. Ecohydrological interfaces as hotspots of ecosystem processes. *Water Resources Research* DOI: 10.1002/2016WR019516
- Krause S, Tecklenburg C, Munz M, Naden E. 2013. Streambed nitrogen cycling beyond the hyporheic zone: Flow controls on horizontal patterns and depth distribution of nitrate and dissolved oxygen in the upwelling groundwater of a lowland river. *Journal of Geophysical Research: Biogeosciences* **118** (1): 54–67 DOI: 10.1029/2012JG002122
- Labagh JW, Schuster PF, Reddy MM, Aiken GR, Rosenberry DO. 1997. Area of Outseepage of Inseepage. *Water Resources* **33** (12): 2799–2812 DOI: 10.1029/97wr02427
- Larkin RG, Sharp JM. 1992. On the relationship between river-basin geomorphology, aquifer hydraulics, and ground-water flow direction in alluvial aquifers. *GSA Bulletin* **104** (12): 1608–1620 Available at: [http://dx.doi.org/10.1130/0016-7606\(1992\)104%3C1608:OTRBRB%3E2.3.CO](http://dx.doi.org/10.1130/0016-7606(1992)104%3C1608:OTRBRB%3E2.3.CO)
- Lautz LK, Ribaud RE. 2012. Scaling up point-in-space heat tracing of seepage flux using bed temperatures as a quantitative proxy. *Hydrogeology Journal* **20** (7): 1223–1238 DOI: 10.1007/s10040-012-0870-2
- Lee DR. 1977. A device for measuring seepage flux in lakes and estuaries. *Limnology and Oceanography* **22** (1): 140–147 DOI: 10.4319/lo.1977.22.1.0140
- Leek R, Wu JQ, Hanrahan TP, Barber ME, Qiu H. 2009. Heterogeneous characteristics of streambed saturated hydraulic conductivity of the Touchet River, south eastern Washington, USA. *Hydrological Processes* **23**: 1236–1246 DOI: 10.1002/hyp.7258
- Lewandowski J, Angermann L, Nützmann G, Fleckenstein JH. 2011. A heat pulse technique for the determination of small-scale flow directions and flow velocities in the streambed of sand-bed streams. *Hydrological Processes* **25** (March): 3244–3255 DOI: 10.1002/hyp.8062
- Lewandowski J, Meinikmann K, Pöschke F, Nützmann G, Rosenberry DO. 2014. From submarine to lacustrine groundwater discharge. *IAHS-AISH Proceedings and Reports* **365** (July 2013): 72–78 DOI: 10.5194/piahs-365-72-2015
- Lewandowski J, Meinikmann K, Ruhtz T, Pöschke F, Kirillin G. 2013. Localization of lacustrine groundwater discharge (LGD) by airborne measurement of thermal infrared radiation. *Remote Sensing of Environment* **138**: 119–125 DOI: 10.1016/j.rse.2013.07.005
- Marceau DJ, Hay GJ. 1999. Remote sensing contributions to the scale issue. **25** (4): 357–366
- Marion A, Packman AI, Zaramella M, Bottacin-Busolin A. 2008. Hyporheic flows in stratified beds. *Water Resources Research* **44** (9): 1–10 DOI: 10.1029/2007WR006079

- McBride MS, Pfannkuch HO. 1975. The distribution of seepage within lakebeds. *Journal of Research of the U.S. Geological Survey* **3** (5): 505–512 Available at: <http://scholar.google.com/scholar?hl=en&btnG=Search&q=intitle:Revised+Value+for+the+O18+Fractionation+Between+CO2+and+H2O+at+25#0>
- McCobb TD, LeBlanc DR, Massey AJ. 2009. Monitoring the removal of phosphate from ground water discharging through a pond-bottom permeable reactive barrier. *Ground Water Monitoring and Remediation* **29** (2): 43–55 DOI: 10.1111/j.1745-6592.2009.01235.x
- Meinikmann K, Lewandowski J, Hupfer M. 2015. Phosphorus in groundwater discharge - A potential source for lake eutrophication. *Journal of Hydrology* **524**: 214–226 DOI: 10.1016/j.jhydrol.2015.02.031
- Meinikmann K, Lewandowski J, Nützmann G. 2013. Lacustrine groundwater discharge: Combined determination of volumes and spatial patterns. *Journal of Hydrology* **502**: 202–211 DOI: 10.1016/j.jhydrol.2013.08.021
- Mouhri A, Flipo N, Rejiba F, de Fouquet C, Bodet L, Kurtulus B, Tallec G, Durand V, Jost A, Ansart P, et al. 2013. Designing a multi-scale sampling system of stream-aquifer interfaces in a sedimentary basin. *Journal of Hydrology* **504**: 194–206 DOI: 10.1016/j.jhydrol.2013.09.036
- Müller F. 1997. State-of-the-art in ecosystem theory. *Ecological Modelling* **100** (1–3): 135–161 DOI: 10.1016/S0304-3800(97)00156-7
- O'Neill RV, Johnson AR, King AW. 1989. A hierarchical framework for the analysis of scale*. *Landscape Ecology* **3** (3381): 193–205
- Ong JB, Lane JW, Zlotnik V a., Halihan T, White E a. 2010. Combined use of frequency-domain electromagnetic and electrical resistivity surveys to delineate near-lake groundwater flow in the semi-arid Nebraska Sand Hills, USA. *Hydrogeology Journal* **18** (6): 1539–1545 DOI: 10.1007/s10040-010-0617-x
- Ouellet V, Secretan Y, St-Hilaire A, Morin J. 2014. Water temperature modelling in a controlled environment: Comparative study of heat budget equations. *Hydrological Processes* **28** (November 2012): 279–292 DOI: 10.1002/hyp.9571
- Palmer MA, Journal S, American N, Society B, Mar N. 1993. Experimentation in the Hyporheic Zone : Challenges and Prospectus Experimentation in the hyporheic zone : challenges and prospectus. **12** (1): 84–93
- Poole GC, Berman CH. 2001. An Ecological Perspective on In-Stream Temperature : Natural Heat Dynamics and Mechanisms of Human-Caused Thermal Degradation. **27** (6): 787–

802 DOI: 10.1007/s002670010188

- Pöschke F, Lewandowski J, Engelhardt C, Preuß K, Oczipka M, Ruhtz T, Kirillin G. 2015. Upwelling of deep water during thermal stratification onset—A major mechanism of vertical transport in small temperate lakes in spring? *Water Resources Research* **51** (January 2016): 9612–9627 DOI: 10.1002/2015WR017579
- Ridgway MS, Blanchfield PJ. 1998. Brook trout spawning areas in lakes. *Ecology of Freshwater Fish* **7**: 140–145 DOI: 10.1111/j.1600-0633.1998.tb00180.x
- Rosenberry DO, Lewandowski J, Meinikmann K, Nitzmann G. 2015. Groundwater - the disregarded component in lake water and nutrient budgets. Part 1: Effects of groundwater on hydrology. *Hydrological Processes* **29** (13): 2895–2921 DOI: 10.1002/hyp.10403
- Rosenberry DO, Sheibley RW, Cox SE, Simonds FW, Naftz DL. 2013. Temporal variability of exchange between groundwater and surface water based on high-frequency direct measurements of seepage at the sediment-water interface. **49**: 2975–2986 DOI: 10.1002/wrcr.20198
- Rosenberry DO, Striegl RG, Hudson DC. 2000. Plants as indicators of focused ground water discharge to a Northern Minnesota Lake. *Ground Water* **38**: 296–303
- Rosenberry DO, Toran L, Nyquist JE. 2010. Effect of surficial disturbance on exchange between groundwater and surface water in nearshore margins. *Water Resources Research* **46** (6): 1–10 DOI: 10.1029/2009WR008755
- Sacks BL a, Swancar A, Lee TM. 1998. Estimating Ground-Water Exchange with Lakes Using Water-Budget and Chemical Mass-Balance Approaches for Ten Lakes in Ridge Areas of Polk and Highlands Counties , Florida: 57
- Schmidt C, Bayer-Raich M, Schirmer M. 2006. Characterization of spatial heterogeneity of groundwater-stream water interactions using multiple depth streambed temperature measurements at the reach scale. *Hydrology and Earth System Sciences Discussions* **3** (4): 1419–1446
- Schmidt C, Conant B, Bayer-Raich M, Schirmer M. 2007. Evaluation and field-scale application of an analytical method to quantify groundwater discharge using mapped streambed temperatures. *Journal of Hydrology* **347** (3–4): 292–307 DOI: 10.1016/j.jhydrol.2007.08.022
- Selker JS, Thévenaz L, Huwald H, Mallet A, Luxemburg W, van de Giesen N, Stejskal M, Zeman J, Westhoff M, Parlange MB. 2006. Distributed fiber-optic temperature sensing for hydrologic systems. *Water Resources Research* **42** (12): n/a-n/a DOI: 10.1029/2006WR005326

- Simon HA. 1962. THE ARCHITECTURE OF COMPLEXITY. **106** (6)
- Stets EG, Winter TC, Rosenberry DO, Striegl RG. 2010. Quantification of surface water and groundwater flows to open - and closed-basin lakes in a headwaters watershed using a descriptive oxygen stable isotope model. *Water Resources Research* **46**: 1–16 DOI: 10.1029/2009WR007793
- Stewart JB, Engman ET, Feddes R a., Kerr YH. 1998. Scaling up in hydrology using remote sensing: Summary of a Workshop. *International Journal of Remote Sensing* **19** (1): 181–194 DOI: 10.1080/014311698216503
- Stonestrom D a., Constantz J. 2003. *Heat as a Tool for Studying the Movement of Ground Water Near Streams - Circular 1260*. U.S.G.S. Available at: <http://pubs.water.usgs.gov/circ1260/>
- Tcherepanov EN, Zlotnik V a., Henebry GM. 2005. Using Landsat thermal imagery and GIS for identification of groundwater discharge into shallow groundwater-dominated lakes. *International Journal of Remote Sensing* **26** (17): 3649–3661 DOI: 10.1080/01431160500177315
- Tonina D, Buffington JM. 2007. Hyporheic exchange in gravel bed rivers with pool-riffle morphology: Laboratory experiments and three-dimensional modeling. *Water Resources Research* **43** (1): 1–16 DOI: 10.1029/2005WR004328
- Tóth J. 1963. A theoretical analysis of groundwater flow in small drainage basins. *Journal of Geophysical Research* **68** (16): 4795–4812 DOI: 10.1029/JZ068i016p04795
- Wawrzyniak V, Piégay H, Allemand P, Vaudor L, Goma R, Grandjean P. 2016. Effects of geomorphology and groundwater level on the spatio-temporal variability of riverine cold water patches assessed using thermal infrared (TIR) remote sensing. *Remote Sensing of Environment* **175**: 337–348 DOI: 10.1016/j.rse.2015.12.050
- Webb BW, Hannah DM, Moore RD, Brown LE, Nobilis F. 2008. Recent advances in stream and river temperature research. *Hydrological Processes* **22** (February): 902–918 DOI: 10.1002/hyp.6994 Recent
- Westhoff MC, Savenije HHG, Luxemburg WM, Stelling GS, Van de Giesen NC, Selker JS, Pfister L, Uhlenbrook S. 2007. A distributed stream temperature model using high resolution temperature observations: 1469–1480
- White DS, Journal S, American N, Society B, Mar N. 1993. Perspectives on defining and delineating hyporheic zones. **12** (1): 61–69
- Winter TC. 1999. Relation of streams, lakes, and wetlands to groundwater flow systems. *Hydrogeology Journal* **7** (September 1998): 28–45 DOI: 10.1007/s100400050178

- Winter TC, Harvey JW, Franke OL, Alley WM. 1998. Ground water and surface water: a single resource. U.S. Geological Survey.
- Woessner WW. 2000. Stream and fluvial plain ground water interactions: rescaling hydrogeologic thought. *Ground water* **38** (3): 423–429
- Wu J. 1999. Hierarchy and scaling: extrapolating information along a scaling ladder. *Canadian Journal of Remote Sensing* **25** (4): 367–380
- Wu J, Loucks OL. 1995. From Balance of Nature to Hierarchical Patch Dynamics: A Paradigm Shift in Ecology. *The quarterly review of biology* **70** (4): 439–466 DOI: 0033-5770/95/7004-0003

2 Scaling on temperature tracers for water and heat exchange processes in ecohydrological interfaces

Amaya I. Marruedo Arricibita^{a,b}, Jörg Lewandowski^{a,b}, David M. Hannah^c, Aaron Packman^d and Stefan Krause^c,

^aDepartment of Ecohydrology, Leibniz-Institute of Freshwater Ecology and Inland Fisheries, 12587 Berlin, Germany.

^bGeography Department, Humboldt University of Berlin, 10099 Berlin, Germany.

^cSchool of Geography, Earth and Environmental Sciences, University of Birmingham, B15 2TT Birmingham, United Kingdom.

^dDepartment of Civil and Environmental Engineering, Northwestern University 2145 Sheridan Road, Evanston IL 60208-3109, United States

Submitted to Science of the Total Environment on the 4.12.2017

Abstract

Water and heat fluxes across ecohydrological interfaces can be traced at different space and time scales by a range of different heat tracing techniques. These comprise single point temperature sensors, temperature lances, passive and active fiber optic distributed temperature sensing (FO-DTS), and Thermal InfraRed (TIR) imaging. Previous research has validated and benchmarked the applicability of individual temperature techniques for different environments and on specific scales. However, there are still gaps in the scale continuum when characterizing water and heat fluxes in freshwater environments' ecohydrological interfaces which still remain unresolved. There is an imbalance between measurements and process understanding. The present paper proposes a conceptual guideline for experimental approaches design, based on hierarchical patch dynamics (HPD) theory. The goal of the conceptual guideline is to adequately identify and quantify water and heat exchange processes and its spatio-temporal variability over several scales and across ecohydrological interfaces in freshwater environments by combination of different heat tracing techniques.

Keywords: Groundwater-surface water interactions, hierarchical patch dynamics, conceptual framework, heat tracing.

2.1 Introduction

Water and heat exchange processes occur across ecohydrological interfaces. Ecohydrological interfaces are changing transition areas (non-stationary) that can appear at ecosystem's or subsystem's limits and regulate the flow of water and energy (e.g. heat) between neighboring systems, among others (Krause *et al.*, 2017). Exchange of water and heat in freshwater ecosystem's ecohydrological interfaces can be facilitated by groundwater (GW) discharge to lakes (Lacustrine Groundwater Discharge, LGD), GW-SW exchange or SW flow into the stream bed (Hyporheic Exchange Flow, HEF) in rivers and infiltration of precipitation in soil, amongst others (see Figure 2.1). Ecohydrological interfaces can become hot-spots for water and heat exchange processes that play a key role in freshwater environments (Krause *et al.*, 2017). For instance, GW discharge into rivers or LGD provides areas of warmer or colder water temperature that can function as thermal refugia for some species of fish (Brabrand *et al.*, 2002; Hayashi and Rosenberry, 2002; Warren *et al.*, 2005; Baker *et al.*, 2014), may represent potential vectors for pollution in streams and lakes (Nakayama and Watanabe, 2008), can influence nutrient budgets of lentic ecosystems (Shaw *et al.*, 1990; Meinikmann *et al.*, 2013) and supply stream organisms with nutrients (Boulton *et al.*, 1998). SW downwelling into the stream bed provides dissolved oxygen and organic matter to microbes and invertebrates in the hyporheic zone (Boulton *et al.*, 1998).

A combination of different approaches in order to picture the complete scale continuum of water and heat exchange processes across ecohydrological interfaces is recommended by different authors, e.g. Krause *et al.* (2014). Several studies have previously combined various heat and water flux tracing methods aiming to describe water and heat exchange processes across several scales (Binley *et al.*, 2013; Blume *et al.*, 2013; Hare *et al.*, 2015; Krause *et al.*, 2012). All these investigations have described, tested and benchmarked the mentioned techniques in different environments and scales. However, there are gaps in the scale continuum when characterizing water and heat fluxes in freshwater environments' ecohydrological interfaces which still remain unresolved (McDonnell *et al.*, 2007; Boano *et al.*, 2014; Krause *et al.*, 2014).

HEF in streams, LGD in lakes, SW flow across the stream or lake bed and water (e.g. rain) infiltration into soils involves water and heat exchange processes across ecohydrological interfaces that range several scales in space and time (Figure 2.1).

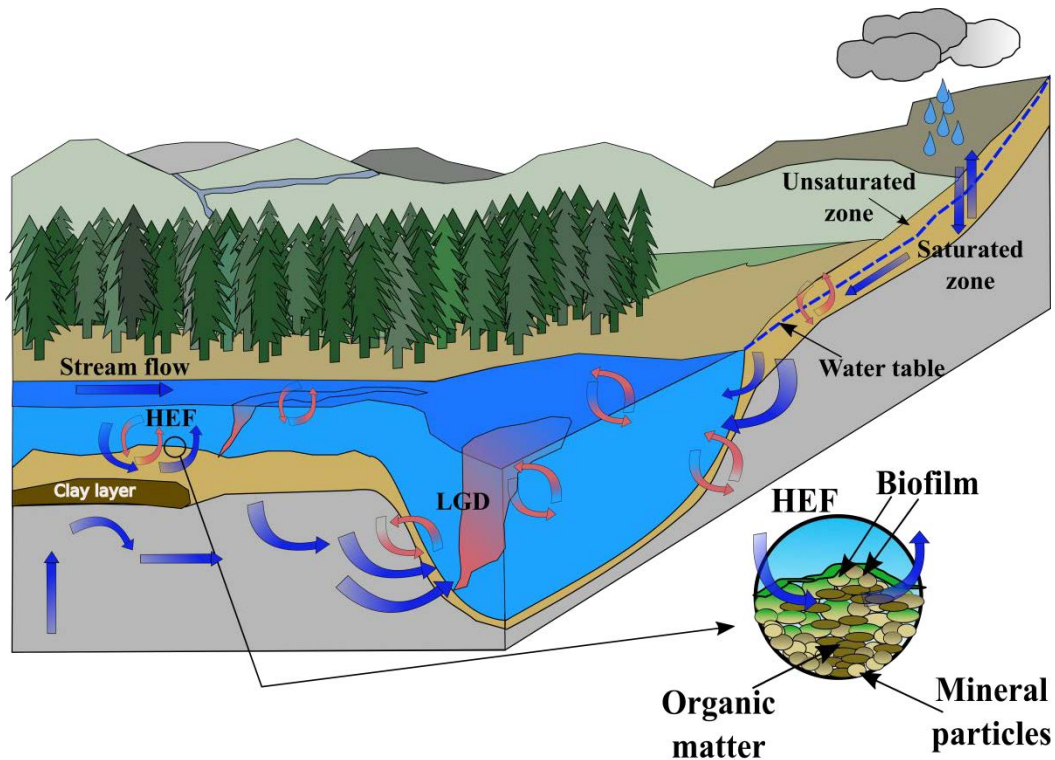


Figure 2.1 Conceptualization of heat and water exchange processes at freshwater ecosystem across several ecohydrological interfaces.

Water and heat fluxes in freshwater environments across different ecohydrological interfaces can be traced at different spatial and temporal scales by heat tracing techniques (Anderson, 2005). Hydrological and heat fluxes can be monitored by anomalies in temperatures or how fast a specific point in space is cooling. The observed temperature patterns are useful for information to understand heat transport processes and water fluxes related to them (Constantz and Stonestrom, 2003).

The tracing of temperature in freshwater environments is based on a wide range of different technological and methodological applications:

For instance, in Wawrzyniak *et al.*, (2016), GW discharge into a stream was traced by remote sensing of water surface temperatures, in Angermann *et al.*, (2012) hyporheic flow was traced in the upper part of the hyporheic zone (HZ) by Heat Pulse Sensor (HPS) and in Ciocca *et al.*, (2012) soil moisture was traced in the soil/sediment column by Active- Fiber Optic Distributed Temperature Sensor (A-FODTS).

The scale at which the measurements are performed strongly affects the interpretation of respective measurements: Processes and parameters relevant at one scale might not have the same relevance or predictive capacity at another scale (Turner, 1989). For this reason, limitation of monitoring campaigns to one single device and its specific scale optimum, lead

to incomplete observations and biases in the analysis of processes and patterns described. In fact, there is a strong trend in recent studies to combine multiple technologies/approaches in order to overcome data gaps in the scale continuum (Krause *et al.*, 2012; Lautz and Ribaud, 2012; Blume *et al.*, 2013; Hare *et al.*, 2015). However, there is an imbalance between measurements and process understanding. Available methods and procedures for transferring information from one scale to another are not complete. It is not clear yet how well the available scaling theories could be applied to multiscale water/heat exchange processes across ecohydrological interfaces in freshwater environments.

Furthermore, there is a lack of a general conceptual framework for freshwater ecosystems which integrates water and heat exchange processes (LGD, HEF, and water flow from saturated to unsaturated zones) across ecohydrological interfaces with available heat tracing techniques.

This is relevant because heat tracing techniques used for monitoring dynamic processes in space and time are also affected by the environment where the measurements are done (e.g. scale and meteorological conditions) (chapters 3 and 4).

For these reasons, the present paper proposes a conceptual guideline for experimental approaches design, based on hierarchical patch dynamics (HPD) theory (Wu and Loucks, 1995). The goal of the conceptual guideline is to adequately identify and quantify water and heat exchange processes and its spatio-temporal variability over several scales and across ecohydrological interfaces in freshwater environments by combination of different heat tracing techniques.

Ultimately, this conceptual guideline will guide or assist the researcher on how to combine and best apply different heat tracing techniques adequately across the spatial and temporal scale continuum to get the best picture of the processes under study. In the following sections an overview of HPD, how HPD could be applied in heat tracing of water and heat fluxes in freshwater environments, heat tracing techniques available for monitoring water and heat fluxes across ecohydrological interfaces and proof of concept of the suggested HPD scheme for a generic freshwater environment will be presented.

2.2 Theory and methodology of hierarchical patch dynamics

The hierarchical patch dynamics theory (HPD) (Wu and Loucks, 1995) integrates hierarchy theory with patch dynamics theory. This theory describes the dynamic relationship between patterns, processes and scales in a landscape context. On the one hand, hierarchy theory gives guidelines to resolve a complex system and has a vertical perspective (top down/ bottom up

approach). On the other hand, patch dynamics addresses spatial heterogeneity and its variation and has a horizontal perspective (sideways/lateral approach) (Wu, 1999). The output of combining both theories into HPD represents the integration of structural and functional components of a spatially spread system (e.g. landscape) into a comprehensible hierarchical framework (Wu and David, 2002).

The HPD can be applied by using a hierarchy of patches in freshwater environments linking physical processes that go across scales (Poole and Berman, 2001) and ecohydrological interfaces. In the present case, the considered processes are water and heat exchange processes.

2.2.1 Hierarchy theory

A hierarchic system is formed by interrelated subsystems. At the same time, each of the subsystems is also hierarchic in structure until the lowest level of the system is reached, an elementary system (Simon, 1997). The subsystems that comprise a level are called “holons” (Koestler, 1967). Koestler, (1967) defined the concept of “holon” as a dual faced entity. “Holons” act as “wholes” when facing downwards and as “parts” when facing upwards (Wu, 1999). Levels in the traditional hierarchy usually apply to scalar hierarchies (O’Neill *et al.*, 1989). However, in ecological hierarchy theory this is not always the case; there are also more definitional hierarchies (Wu, 1999). A hierarchical system has a vertical and a horizontal structure. The vertical structure is composed by the levels and the horizontal structure is composed by the “holons”. In hierarchical systems, the highest levels are characterized by slower and larger entities, and the lower levels are characterized by faster and smaller entities. The upper levels apply constraints to the lower levels, while the lower levels give initiating conditions to the upper levels (Simon, 1977; Urban *et al.*, 1987). Each of the constraints will provide a context for the processes of the lower levels of the hierarchy (Urban *et al.*, 1987). Hierarchy theory proposes that when studying a process at a specific hierarchical level (called the focal level, or Level 0), the mechanistic understanding of the process comes from the next lower level (Level -1), while the relevance of that process can only be unveiled at the next higher level (Level +1). This is sometimes referred to as the Triadic structure of hierarchy (Salthe, 1985).

For instance, Figure 2.2 presents a hierarchical structure for the water and heat exchange processes shown in Figure 2.1. The smallest hierarchical units considered here are defined as aggregates in the colmation/biofilm layer of streambeds or lakebeds and the unconsolidated and consolidated sediment aggregates in soils. Grouping the smallest units, in this case

aggregates, leads to the next hierarchical level. Aggregates can be composed of: 1) biofilm, mineral particles, organic matter and water if the aggregate belongs to the colmation/biofilm layer, 2) mineral particles, organic matter, humus, water and air if the aggregate belongs to the unconsolidated sediment layer and 3) mineral particles and water if the aggregate belongs to the consolidated sediment layer (Figure 2.2).

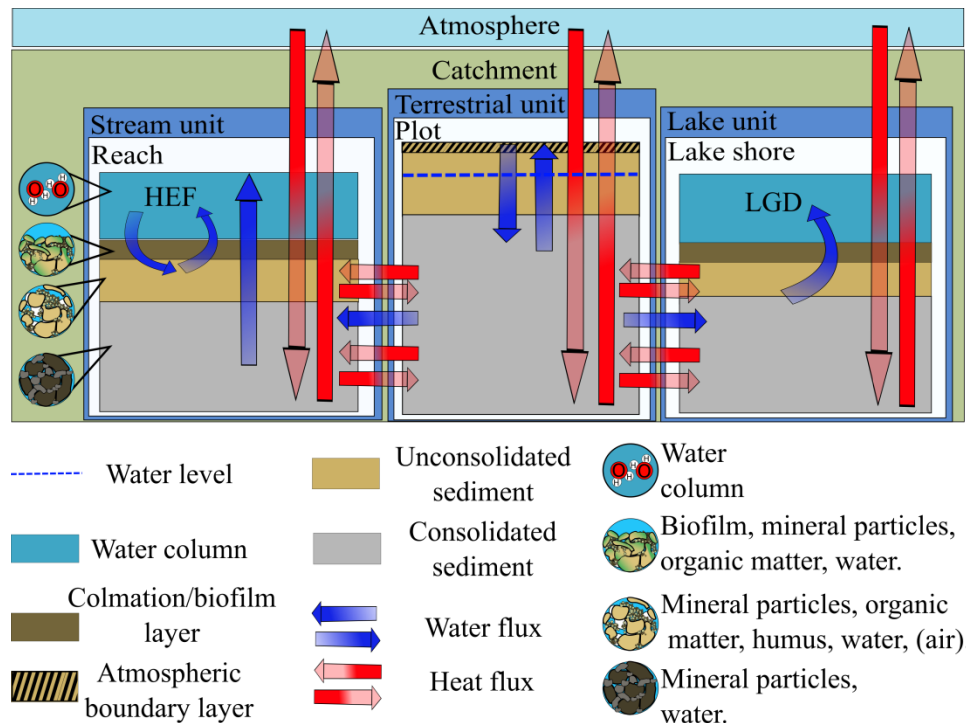


Figure 2.2 Hierarchical conceptualización of heat and water exchange processes at freshwater ecosystems at different spatial and temporal scales and across different ecohydrological interfaces.

Water and heat fluxes occur across many ecohydrological interfaces such as: atmospheric boundary layer-atmosphere or water column-atmosphere (Figure 2.2). However, water and heat fluxes that occur across ecohydrological interfaces can be considered at different scales in the hierarchical organization of the freshwater environment in Figure 2.2. Thus, water and heat fluxes can be observed at small scales (e.g. aggregate level in the hierarchical structure of the freshwater environment), local scales (e.g. reach, lake shore or plot), at a stream, lake or terrestrial unit scale or even at the catchment scale.

2.2.2 Patch dynamics in landscape ecology

The concept of patch dynamics developed in landscape ecology is used in ecology since 1970 (Wu, 1999) and it is nowadays widely applied to freshwater systems, too (Johnson and Gage, 1997; Poole and Berman, 2001). Patch dynamics resolve landscapes into elements or patches (Forman, 1995). Thus, freshwater ecosystems can be understood as landscapes composed by

dynamic interacting terrestrial and aquatic elements (Frissell *et al.*, 1986; Fisher *et al.*, 1998; Dent *et al.*, 2001; Soranno *et al.*, 2010). These elements are defined as the basic homogeneous units (patches) observable in the landscape at a specific spatial scale (Poole and Berman, 2001). The patch dynamics theory studies the structure, function and dynamics of a patchy systems focusing on its emergent properties, which originate from interactions at the patch level (Wu and Levin, 1997; Wu and David, 2002).

2.2.3 Hierarchical patch dynamics

In HPD the system is understood to be hierarchical and each of the levels of the hierarchy is composed of patches. These patches coincide with the concepts of “holons” in hierarchy theory. In this manner, concepts explained for hierarchy theory can be translated to HPD. The only difference is that HPD considers that patches are dynamic in space and time, which allows studying processes and patterns in space and time within a landscape. A catchment can hence be divided into a hierarchy of patches in three dimensions in space (e.g. in plane view and lateral cross-section view). At any scale, these patches are affected by the interaction between their context with the patch itself (context is defined by the next larger patch it belongs in), the internal structure of the patch in question and the processes across scales that link the patches in the hierarchy (Poole and Berman, 2001). There have been a number of applications of hierarchy theory and HPD in environmental sciences and ecohydrology. Frissell *et al.*, (1986) introduced a hierarchical framework for habitat classification of stream systems. A hierarchical approach allowed Dent *et al.*, (2001) decomposing the influences of subsurface groundwater up-welling at different scales. For instance, Dent *et al.*, (2001) found that subsurface patches affect surface water nutrient patterns from a few meters scales to several kilometers scales. Finally, Poole and Berman, (2001) used the HPD approach for fluvial landscape ecology in order to resolve interactions between patches of a single scale and across different spatial scales. Thus, the present study is not the first one that approaches freshwater environments (such as streams and lakes) by hierarchy theory and hierarchical patch dynamics from a landscape perspective. However, monitoring of ecohydrological interfaces in freshwater environments have not yet been broadly approached from a landscape perspective (Soranno *et al.*, 2009). Furthermore, the mentioned examples introduce and suggest conceptual frameworks for stream ecosystems and some of them use these frameworks for interpretation of nutrient processes or for simulation of models. Nevertheless, none of them uses the conceptual framework for designing experimental approaches that combine different heat tracing techniques adequately over the scale continuum to get the best

picture of the water and heat exchange processes across ecohydrological interfaces in freshwater environments.

2.3 Application of HPD to water and heat fluxes in freshwater environments

In this section a generic freshwater environment is conceptualised in different hierarchical levels and patches following HPD (Figure 2.3). The processes explained and shown in Figure 2.1 and 2.2 and the scale-dependent suitability of the range of different heat tracing techniques across different types of ecohydrological interfaces are gathered in Figure 2.3. By following Figure 2.3, it is possible to design a monitoring approach, which could allow vertical spatial scaling across ecohydrological interfaces (hierarchy theory perspective) and horizontal spatial scaling across scales (patch dynamics perspective). In section 4 (*Heat tracing techniques in ecohydrological interfaces*), heat tracing techniques included in Figure 2.3 will be introduced in more detail. In section 5 (*Proof of concept: vertical upscaling of discrete GW upwelling, by FO-DTS and TIR*) an example experiment approach designed following Figure 2.3 will be introduced as a proof of concept for the suggested HPD based scheme and to illustrate how to follow Figure 2.3 in a real case study.

2.3.1 Structure of the HPD scheme for generic freshwater environments

Levels in a hierarchical structure can usually be applied to scalar hierarchies (O'Neill *et al.*, 1989). Scales defined in Table 1 (see in section 4: *Heat tracing techniques in ecohydrological interfaces*) are considered as the levels for the hierarchical structure of a generic freshwater environment according to Figure 2.3. Thus, the upper level of the hierarchical system describing a generic freshwater environment is defined as the catchment scale. Within this level, three structural elements are found: streams, lakes and terrestrial areas around them. Each of them is considered a patch because it represents a landscape unit within the catchment with assumed homogeneous properties and functioning. This level is related to stream/lake or terrestrial scale. The next lower hierarchical level of a stream will be a reach. For lakes only the lake shore will be regarded as the next lower level because this is where usually most LGD occurs (McBride and Pfannkuch, 1975; Lewandowski *et al.*, 2013). Finally, the terrestrial level can be resolved into plots. Stream reach, lake shore and plot levels will be related to reach, lake shore and plot scales respectively. In a very general way and with a vertical perspective a stream reach and a portion of the lake's shore can be represented as a combination of water column, colmation/biofilm layer, unconsolidated sediments and consolidated sediments. Each of this compartments are patches that are part of the upper level that we call reach or lake shore. These compartments form the local level or scale. Within this

scale, water and heat exchange occur across the above-mentioned compartments in both time and space. Each of the compartments represents one phase and the boundaries between them are called interfaces. Thus, we can find at the defined local level or scale the following interfaces:

- Consolidated sediment-Unconsolidated sediment
- Unconsolidated sediment-Colmation/biofilm layer
- Colmation/biofilm layer-Water column
- Water column-Atmosphere

Similarly, the plot-scale can be presented by units or patches that are characterised by the following properties: atmospheric boundary layer, unconsolidated sediments and consolidated sediments. Each of the compartments is a phase and the boundaries between them are interfaces across which water and heat exchange processes will occur:

- Consolidated sediments-Unconsolidated sediments
- Unconsolidated sediments-Atmospheric boundary layer
- Atmospheric boundary layer-Atmosphere

The unity of all these compartments together forms the local scale. Finally, the lowest hierarchical level considered in this paper will be related to water drops and colmation/biofilm, unconsolidated and consolidated aggregates. Figure 2.3 summarises all the hierarchical levels, scales and patches considered in the generic freshwater environment.

Heat exchange processes can be observed from lowest levels of organization (aggregate level) to the highest level of organization in our system (catchment level) and vice versa (Figure 2.3, red arrows). Water exchange processes occur across all the levels of organization in our system. However, LGD, HEF and water infiltration into subsurface soil are generally considered at a plot scale where water flows across different interfaces (Figure 2.3, blue arrows).

Finally, the atmosphere (where different weather conditions occur) is not considered as a level in our system because is not a scalar hierarchy level. But, it is an important element in the system since heat exchange across the defined HPD structure is affected by it. Therefore, it is included in Figure 2.4 as an influencing element in the described system.

This simplification of a generic freshwater environment (our system) eases integration of a HPD representation of: 1) a freshwater system and 2) water and heat exchange processes across and within the represented generic freshwater system and its ecohydrological interfaces.

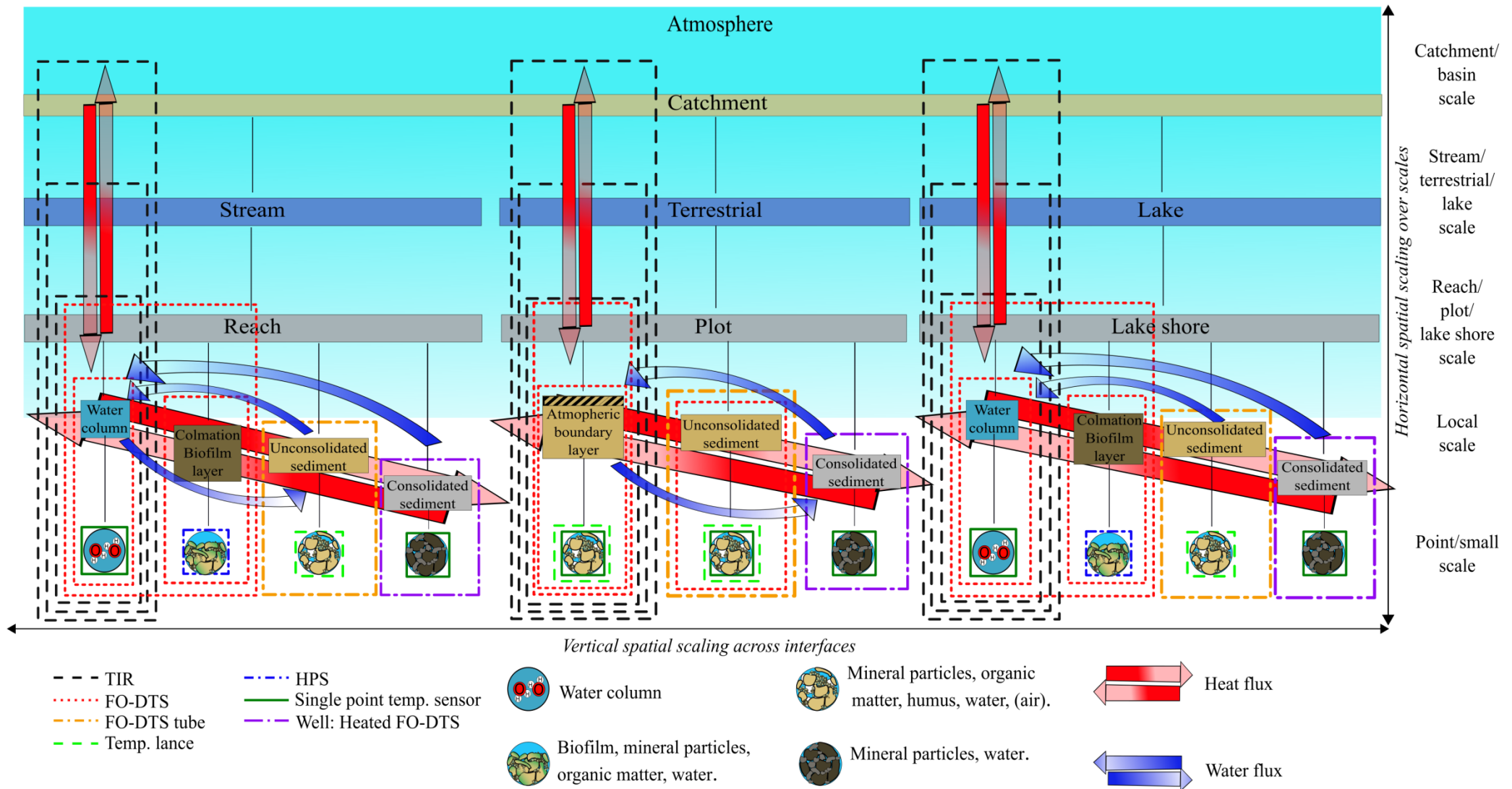


Figure 2.3 An HPD based conceptual guideline on how to adequately observe water/heat exchange processes across spatial scales and ecohydrological interfaces by combination of different heat tracing techniques.

2.4 Heat tracing techniques in ecohydrological interfaces

In the first part of this section, a general description of each of the considered heat tracing techniques for heat and water fluxes across different ecohydrological interfaces is introduced. Table 1 summarises the main characteristics of each of the heat tracing technologies based on scale, limitations and recommendations for best use of the technology. In the second part of this section the application of each of the described heat tracing techniques at the different ecohydrological interfaces defined in Figures 2.1, 2.2 and 2.3 is introduced.

Self-contained temperature loggers (e.g. Onset Hobo data loggers from Onset Computer Corp., Pocasset, MA, USA; <http://www.onsetcomp.com>) can be easily setup in stream or lake beds, surface waters or inside a piezometer in the soil profile. They can record long time series of temperature measurements. However, they only provide point scale temperature data. For example, Lowry *et al.*, (2007) used Hobo loggers to verify FO-DTS measurements.

Temperature lances are multilevel stainless steel temperature probes with attached data logger that are used to simultaneously record temperatures in different sediment depth (usually in the upper meter of the sediment or shallower depths). They provide time series of vertical temperature depth profiles. Based on the curvature of the profile, the dampening of temperature fluctuations with depth or the phase shift of temperature fluctuations fluxes can be calculated (Constantz and Stonestrom, 2003). The common tool to calculate vertical water flux rates at multiple depths from the data obtained from the temperature lances is the program VFLUX (Gordon *et al.*, 2012). The principle VFLUX is based upon is offset in time and depth dependent dampening of diurnal oscillation. However, in streams or lakes with strong non vertical water fluxes across the stream/lake bed, the simplification of assuming purely vertical flow that is underlying this concept might not be valid (Schmidt *et al.*, 2006).

The 3D heat pulse sensor (HPS) (Lewandowski *et al.*, 2011) is a point-scale heat tracing device which provides 3D heat and water flux information over a diameter of 7 cm in the hyporheic zone. It is an optimized heat pulse sensor device which has been adapted by Lewandowski *et al.*, (2011) from previous 1D and 2D heat pulse sensors used in boreholes for horizontal groundwater flow characterization and in soil sciences for characterization of vertical soil water movement (Byrne *et al.*, 1967; Kawanishi, 1983; Ren *et al.*, 2000; Greswell *et al.*, 2009; Cuthbert *et al.*, 2010). The HPS performs best in sandy stream beds with high flow velocities in the HZ (Lewandowski *et al.*, 2011; Angermann *et al.*, 2012a, 2012b).

The fiber optic distributed temperature sensor (FO-DTS) (Selker *et al.*, 2006a, 2006b) has been used in various different setups: at groundwater-surface water interfaces of streams and

lakes as a loose horizontal loop (Krause *et al.*, 2012; Blume *et al.*, 2013), across stream beds and sediment columns curled around a cylinder (Briggs *et al.*, 2012), in soil profiles for soil moisture characterization (Ciocca *et al.*, 2012), across the forest canopy as a single loose cable (Krause *et al.*, 2013a) or in the water column in a 3D looped cable setup (e.g. chapter 3). At the moment the highest sampling resolution of the FO-DTS is 12.5 cm (i.e. Ultima-S, Silixa Ltd.). The sampling resolution is determined by the duration of each of the laser pulses sent by the DTS. The ULTIMA-S sends pulses of 12.5 ns. This results in a sampling resolution of 12.5cm. The FO-DTS cable allows 1D to 3D setups providing the opportunity to describe 1D, 2D and 3D heat and water flow patterns at local to medium scales.

When naturally occurring temperature variations are not strong enough to be traced by FO-DTS, the metal coating of the optical fiber (Read *et al.*, 2014) or an independent metal wire at the core of the cable (Ciocca *et al.*, 2012), can be actively heated in order to monitor how fast the heat dissipates from the heated cable to the surrounding medium. This data provides information on the spatial distribution of physical properties of the surrounding medium or fluid fluxes (Read *et al.*, 2014). This so called Active DTS (A-DTS) method has been used in boreholes to track groundwater movement (Read *et al.*, 2014), to measure soil moisture in soils (Ciocca *et al.*, 2012) or in streambeds to quantify streambed flow dynamics in zones of strong groundwater discharge (Briggs *et al.*, 2016a).

Finally, thermal infrared (TIR) imaging allows to measure temperatures of water surfaces or top soil in a wide range of environments with low to coarse spatial resolutions (mm to decameters) at local, catchment or regional scales (e.g: from m² to km²) depending on the system used (ground based, unmanned aerial vehicle, plane or satellite) (Davies *et al.*, 2008; Hare *et al.*, 2015; Pöschke *et al.*, 2015; Briggs *et al.*, 2016; Lee *et al.*, 2016). Haghighi and Or, (2015) measured soil surface temperatures with a handheld TIR camera at small scale. In Hare *et al.*, (2015) GW discharge to SW is monitored by using a ground-based TIR camera at the reach/local scale. In Pöschke *et al.* (2015) LGD into a lake is monitored at the lake scale with a TIR setup in an airplane. As another example, Davies *et al.* (2008) combined ground based TIR and satellite TIR imagery to monitor volcanic lake temperatures.

Table 2.1 summarises considered heat tracing techniques in this paper, for water and heat fluxes across ecohydrological interfaces. The scale at which each of the heat tracing techniques are applied, limitations of the heat tracing technology and recommendations on how to best use each of heat tracing techniques are included.

Table 2.1 Summary of the heat tracing techniques that are considered in this paper for scaling of water and heat fluxes in freshwater environments: scales, limitations and recommendations. Scales used in this paper are: Point/Small (few cm), local (cm to few m), reach, plot or lake shore (from few m), stream, land or lake (from m to km) and finally catchment (from km). “Temp.” goes for temperature.

Heat Tracing Technique	Scale	Limitation	Recommendation
<i>Single point temp. sensor</i>	Point	<ul style="list-style-type: none"> • Point temperature measurements 	<ul style="list-style-type: none"> • For verification of other devices, e.g. FO-DTS.
<i>Temp. lance</i>	Point and local vertical patterns	<ul style="list-style-type: none"> • Max. depth: 0.5.m. Point temperature measurements. • Not for horizontal fluxes. 	<ul style="list-style-type: none"> • For vertical flux calculation. • For preliminary study of stream/lake bed for choosing locations for additional devices (Schmidt et al. 2006).
<i>HPS</i>	Point and small	<ul style="list-style-type: none"> • Sandy sediment texture. • Sufficient subsurface flow velocity. 	<ul style="list-style-type: none"> • 3D fluxes in HZs. • Best sandy HZs and fast flowing streams.
<i>FO-DTS</i>	Small, local, plot, lake shore and stream.	<ul style="list-style-type: none"> • Extensive logistics. • Challenging calibration. 	<ul style="list-style-type: none"> • 1D to 3D heat flux patterns.
<i>A-DTS</i>	Small, local, plot, lake shore and stream.	<ul style="list-style-type: none"> • Extensive logistics. • Challenging calibration. 	<ul style="list-style-type: none"> • When GW-SW temperatures differences are not sufficient for classic DTS.
<i>TIR</i>	Local	<ul style="list-style-type: none"> • Water and soil surface temperatures. 	<ul style="list-style-type: none"> • Ground trothing required.

Figure 2.4 shows how heat tracing techniques considered in this study (summarised in Table 2.1) can be setup across the ecohydrological interfaces shown in, Figure 2.1,2.2 and 2.3.

The HPS can monitor 3D heat fluxes in the colmation/biofilm layer and the upper part of the unconsolidated sediment layer. Temperature lances are installed in the colmation/biofilm layer and partly in the unconsolidated sediment layer too. It provides vertical temperature variations in the colmation/biofilm layer and in part of the unconsolidated sediment layer.

The application of FO-DTS surveys in 1D to 3D experimental setups offers the opportunity to monitor temperature variations across several interfaces in the reach, plot and lake shore levels, the colmation/biofilm layer and in the unconsolidated sediment layer in streams, lakes and soils to obtain a temperature depth profile with an even higher resolution. FO-DTS tube can also monitor temperature variations in the water column or air.

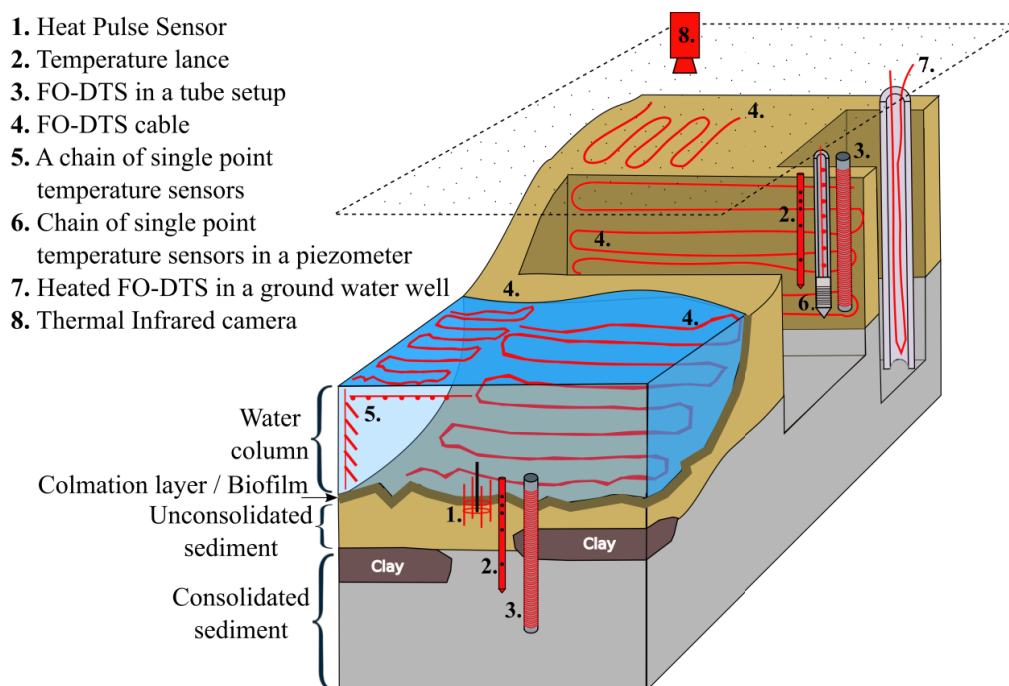


Figure 2.4 Application of different experimental temperature tracing techniques to identify heat and water fluxes at different ecohydrological interfaces in freshwater environments defined in Figures 2.1, 2.2 and 2.3.

Single temperature sensors can be attached to a string or a rope. The string of single temperature sensors can be setup in the water column, on the water surface, on the colmation/biofilm layer in streams and lakes and on the atmospheric boundary layer on soils. The string of single temperature sensors can also be setup inside a piezometer across the unconsolidated sediment layer and the colmation/biofilm layer. Single temperature sensor strings can be installed as well in boreholes across the consolidated sediment layer.

The diameters of some of the A-DTS cables are higher than that of comparable standard FO-DTS cables (e.g. when an independent metal wire at the core of the cable is heated). In this case, A-DTS are usually setup in 1D or 2D designs as a loose cable in a borehole across the consolidated sediment layer, on the colmation/biofilm layer forming several loops or buried in a coil in the unconsolidated sediment layer in the terrestrial unit. When the outer jacket of the A-DTS is heated (e.g. the outer jacket of a thin tube fibre), then, the setup options for the A-DTS are the same or similar as with the FO-DTS.

Finally, TIR cameras provide surface water and soil temperatures. Although TIR imaging cannot monitor temperature inside of water and soil bodies, it provides temperature data over continuous spatial areas in one shot.

Each of the heat tracing techniques included in this paper is generally best used in one specific scale and phase. However, none of them is able to monitor water and heat fluxes across the scale continuum and all the ecohydrological interfaces described in Figures 2.1, 2.2 and 2.3.

2.5 Proof of concept: vertical upscaling of discrete GW upwelling by FO-DTS and TIR

The experimental design and investigation in chapters 3 and 4 are used in the following section to demonstrate the suitability of the suggested approach for scaling water and heat exchange processes (Figure 2.3). The triadic structure of hierarchy (Salthe, 1985) was the basis when designing the experiment approach for tracing warm water up-welling in the water column caused by discharge of warm GW (LGD). In the present manuscript the term upwelling describes upward transport processes in the water column. LGD was simulated in an outdoor mesocosm with injection of warm water at its bottom. In this case, the goal was to test vertical scaling mechanisms and monitoring technologies across the interfaces of discrete discharge of warm water, from the colmation/biofilm layer (mesocosm bed) across the water column to the atmosphere. Thus, our focal level or level 0 was defined as the water column. The mechanistic understanding of water and heat exchange processes related to LGD comes from the next lower level or level -1. This belonged to the colmation/biofilm layer (or mesocosm bed) while the relevance of the process is unveiled at the next higher level or level +1. In the present example, level +1 belongs to the water surface or the water surface-atmosphere interface.

The processes' mechanistic understanding (or the main property controlling the processes at level 0) coming from level -1 can be related to the hydraulic conductivity (K) of the sediment of the colmation/biofilm layer (or mesocosm bed). Pore-water flow in streambed and lake bottom sediments is regulated by the hydraulic gradient and the hydraulic conductivity of sediments while the colmation/biofilm layer adds another filter creating respective spatial patterns. In the mesocosm experiment of Maruedo et al., 2017, LGD was simulated by a pipe injecting warm water at the bottom of the mesocosm through a bag filled with coarse sediments to support dispersion of the point inflow in a more natural way.

The relevance (or impact) of the process can be unveiled on the surface water (or at level +1). This is understood in terms of how much artificial warm water should be injected in order to detect a robust heat signal at the water surface. The aim of the experiment was to follow the heat signal across the water column using different heat tracing techniques at different spatial

scales. Going back to Figure 2.4 and having in mind our triadic hierarchical structure we should follow the figure from right to left within the lake shore level. First we should identify which are the boundaries and interfaces of our triadic structure in Figure 2.3: Figure 2.5 is a zoom out of Figure 2.3.

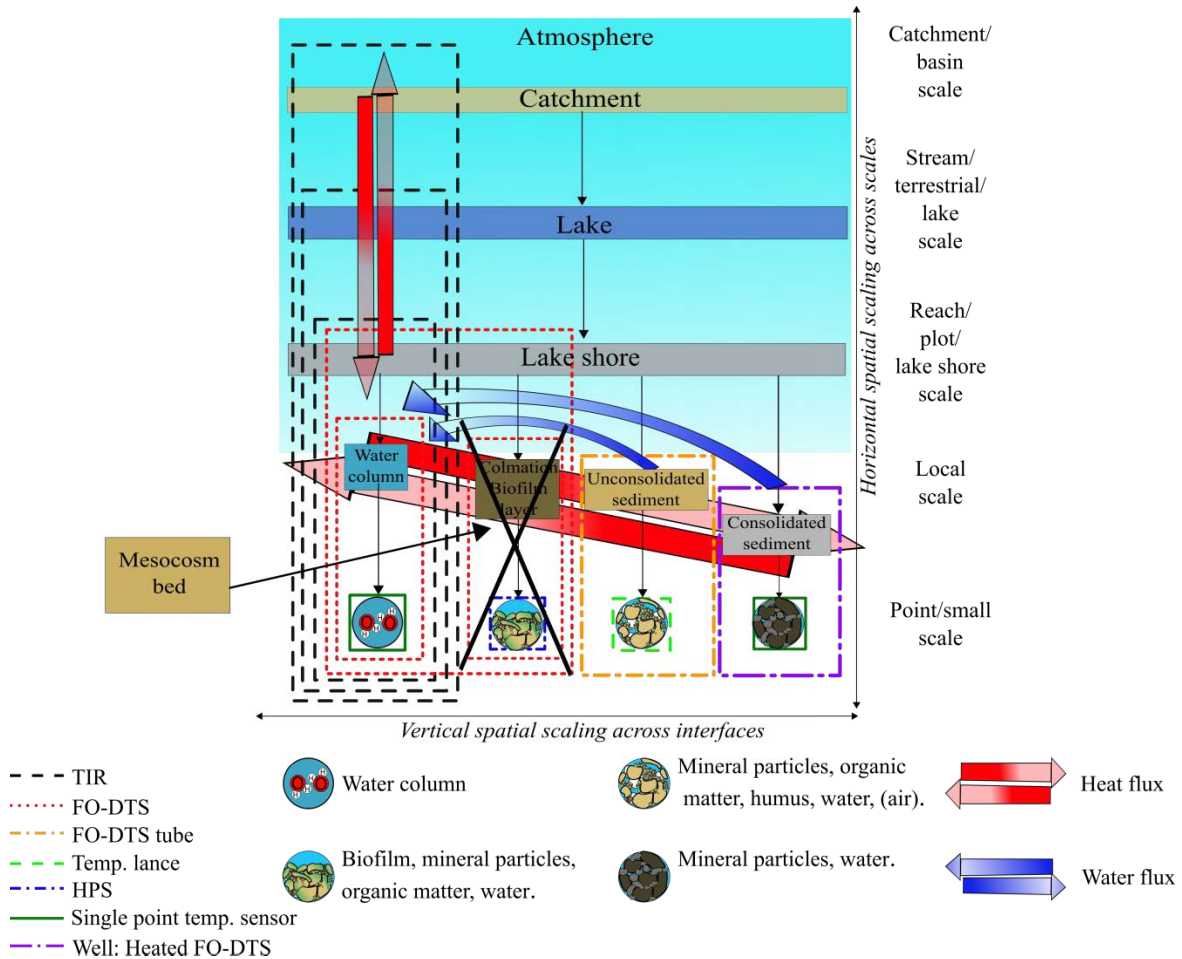


Figure 2.5 Example for vertical scaling of water and heat exchanges related to simulated LGD.

Since there was no colmation/biofilm layer in our case study, the lowest boundary is the unconsolidated sediment (or the artificial mesocosm bed which is the coarse sediment in the bag). Which devices could we have deployed on this boundary or interface? If there would have been a colmation/ biofilm layer, following Figures 2.3 and 2.5, we could have chosen between a HPS at the small scale and FO-DTS at the local scale. As there was no such layer, we can substitute the layer by the mesocosm bed compartment (Figure 2.5). Still, the heat tracing techniques recommended for this interface would be the same. Following Figure 2.5 on the left we find the water column compartment (patch within the lake shore scale level). Within this compartment measurements can be conducted by using FO-DTS at local scales or

single point temperature sensors at point scales. Finally, in Figure 2.5 it is possible to see how the compartment (patch) called water column overlaps with the element atmosphere. This is the water column-atmosphere interface. FO-DTS allows measuring at this interface at a local scale, or – if wanted – at a larger scale (reaching scale). This can be combined with TIR measurements (see Figure 2.5) at the lake shore scale.

Summarizing, in order to get measurements to trace warm water upwelling across the water column we could combine the following devices: HPS, single temperature sensors, FO-DTS and TIR camera. In this way we can get information on small and local scales and at different interfaces (defined here as vertical scaling).

Since, in this example water discharge is artificial, the injection rate is controlled and the location of the discrete discharge is known, it was not necessary to monitor the sediment-water interface. Thus, a 3D setup of FO-DTS cable was used in the water column inside the mesocosm and a TIR camera was setup at an altitude of 4 m above the mesocosm to monitor temperature changes caused by upwelling of warm water in the water column (see chapters 3 and 4).

Monitored and analysed temperature data showed that at level +1 (water column-atmosphere interface) the relevance of the process is unveiled (or the effect/impact of the process is observable), but this was strongly linked to weather conditions. Thus, detectability of warm water upwelling on the surface water is strongly influenced by weather conditions (see chapters 3 and 4). Heat fluxes occur across interfaces in both directions: from atmosphere to the water column and from the water column to the sediment and vice versa. Under clear sky conditions, downward heat flux from the atmosphere is strong enough to affect and change the temperature in the water column. In consequence, heat signals from the artificial warm water upwelling cannot be traced in the top layers of the water column. On the contrary, under overcast conditions, downward heat flux is not strong enough to affect and change the temperature in the water column and the heat signal from the artificial warm water upwelling is possible to be traced in the top layers of the water column (see chapters 3 and 4).

This can be understood in terms of HPD by following definitions of top-down and bottom-up processes in Poole (2002): Heat fluxes from the atmosphere are strong enough to affect the condition or the ecological functions (e.g. temperature and consequent change on locations of thermal refugia for fishes) of the water column compartment (patch) (the water column conditions change at local and also at small scales) but heat fluxes from the atmosphere can be affected by changes in patch conditions at much broader scales such as changes in weather conditions over the catchment (the upper level or scale). This could be defined as a *top-down*

process. Warm water upwelling can be affected by small scale patch structure/functions (e.g. sediment aggregates, texture, that influence the hydraulic conductivity of the lake bed) but still can affect patch structure/functions at broader scales (e.g. change in water column temperature or even reach temperature). This is defined as a *bottom-up* process (Poole, 2002).

2.6 Synthesis, conclusions and recommendations

In the present paper a conceptual guideline for adequately identify and quantify water and heat exchange processes and its spatio-temporal variability over several scales and across ecohydrological interfaces by combination of different heat tracing techniques has been introduced. The conceptual guideline proposed is based in HPD theory. HPD allows integrating spatial and temporal variability over several scales and across ecohydrological interfaces of heat and water exchange processes such as GW-SW exchange processes in lakes and streams. Figure 2.3 shows the suggestion of applying HPD in freshwater environments by resolving a generic freshwater environment (or landscape) into different levels or spatial scales and defining the structural patches that comprise each of the levels. Different heat tracing techniques are located in the recommended scales (Table 2.1) and ecohydrological interfaces (Figure 2.4) in order to get the best picture of heat and water exchange processes over several scales and across ecohydrological interfaces. Finally, as a proof of concept, the experiment which is described in more detail in chapters 3 and 4, is introduced. This is an example on how an experimental approach can be designed by following Figure 2.3.

To conclude, the following three main conclusions can be summarized from the work introduced in the previous sections:

- 1) *Heat exchange processes overlap across spatial and temporal scales and the detection of heat as a tracer depends on whether the impact or footprint of the investigated process is dominant or overshadowed:*

For instance, in the field of landscape fire ecology, energy fluxes represent processes and regulations associated with the spatial distribution of energy in relation to patterns in the landscape (McKenzie *et al.*, 2011). Since the present paper focuses on heat fluxes, process and pattern definitions used in the field of landscape fire ecology could be followed in the present case, too. In this manner, heat flux related to water flux is the process that is in our focal level (Level 0), or focus of interest. But, within ecosystems there are lots of heat fluxes. Sun radiation is a top down energy input or energy flux. This energetic input is then subjected to further top-down regulation (e.g. by locally homogeneous spatial fields of humidity,

atmospheric pressure, temperatures, and precipitation) (McKenzie *et al.*, 2011). Thus, heat flux from the atmosphere is a top-down constrain. Whereas, heat flux related to water flux is a bottom-up process/mechanism. These two heat fluxes will overlap across spatial and temporal scales.

2) HPD based approach is helpful to distinguish the overlapping impacts of heat transport processes across spatial and temporal scales:

As found in the example for proof of concept of warm water upwelling tracing experiment, there is an interaction between top-down and bottom-up heat fluxes across spatial scales. When top-down heat flux processes dominate over bottom-up mechanistic processes, homogenizes and coarsens the patterns observed on the surface water (McKenzie *et al.*, 2011), (e.g. from proof of concept: clear sky conditions allow dominant atmospheric heat fluxes leading to homogenous warmer surface water in the mesocosm). On the contrary, when bottom-up processes dominate, more heterogeneous spatial patterns will emerge (McKenzie *et al.*, 2011) (e.g. from proof of concept: overcast conditions limit heat flux from the atmosphere and heat fluxes related to warm water upwelling in the mesocosm become dominant leading to heterogeneous warm water patterns on the water of the mesocosm). Top-down heat fluxes related to atmospheric conditions can be understood as top-down controls, or environmental constraints (Urban *et al.*, 1987) over lower levels in the HPD system of a generic freshwater environment.

3) Introducing HPD into heat tracing across interfaces – this paper used an example experimental approach from chapters 3 and 4, to successfully demonstrate the applicability of the HPD concept in experimental approach and method design for tracing discrete GW upwelling by FO-DTS and TIR across ecohydrological interfaces (vertical upscaling):

The design and successful application of the experiment based in HPD allowed identification of top-down (from the atmosphere to the water column) and bottom up (from the source of the injected warm water in the sediment to the water column) heat fluxes and quantification of heat fluxes across the water column-atmosphere ecohydrological interface. Identified top-down processes affected detectability of bottom-up processes such as warm water upwelling in the water column.

Finally, we would like to remark that it is important to keep in mind that heat fluxes have an influence over the complete scale continuum and across ecohydrological interfaces and that

the used heat tracing techniques will monitor this influence. If we want to identify or isolate water exchange processes related to LGD, HEF or SW exfiltration by tracing heat fluxes we first need to know when the heat flux related to those specific processes are dominant over the spatial and temporal scales and across the interfaces that are being monitored.

Acknowledgments

Funding: This work was supported by the European Union's Seventh Framework programme for research, technological development and demonstration [grant number 60715]: Ecohydrological Interfaces as Critical Hotspots for Transformations of Ecosystem Exchange Fluxes (INTERFACES).

Supplementary information

Annex S1: Definitions

Graphical abstract

References

- Ahl V, Timothy F. Allen. 1996. *Hierarchy Theory: A Vision, Vocabulary, and Epistemology*.
- Allen TFH, Starr TB. 1982. *Hierarchy: Perspectives for ecological complexity*. The University of Chicago Press: Chicago and London.
- Anderson MP. 2005. Heat as a ground water tracer. *Ground water* **43** (6): 951–68 DOI: 10.1111/j.1745-6584.2005.00052.x
- Angermann L, Krause S, Lewandowski J. 2012a. Application of heat pulse injections for investigating shallow hyporheic flow in a lowland river. *Water Resources Research* **48** (October): 1–16 DOI: 10.1029/2012WR012564
- Angermann L, Lewandowski J, Fleckenstein JH, Nützmann G. 2012b. A 3D analysis algorithm to improve interpretation of heat pulse sensor results for the determination of small-scale flow directions and velocities in the hyporheic zone. *Journal of Hydrology* **475**: 1–11 DOI: 10.1016/j.jhydrol.2012.06.050
- Baker BH, Martinovic-Weigelt D, Ferrey M, Barber LB, Writer JH, Rosenberry DO, Kiesling RL, Lundy JR, Schoenfuss HL. 2014. Identifying non-point sources of endocrine active compounds and their biological impacts in freshwater lakes. *Archives of environmental contamination and toxicology* **67** (3): 374–388 DOI: 10.1007/s00244-014-0052-4
- Binley A, Ullah S, Heathwaite AL, Heppell C, Byrne P, Lansdown K, Trimmer M, Zhang H. 2013. Revealing the spatial variability of water fluxes at the groundwater-surface water interface. **49**: 3978–3992 DOI: 10.1002/wrcr.20214
- Blume T, Krause S, Meinikmann K, Lewandowski J. 2013. Upscaling lacustrine groundwater discharge rates by fiber-optic distributed temperature sensing. *Water Resources Research* **49** (October 2012): 7929–7944 DOI: 10.1002/2012WR013215
- Boano F, Harvey JW, Marion A, Packman AI, Revelli R, Ridolfi L, Wörman A. 2014. Hyporheic flow and transport processes: Mechanisms, models, and biogeochemical implications. *Reviews of Geophysics*: 1–77 DOI: 10.1002/2012RG000417. Received
- Boulton AJ, Findlay S, Marmonier P, Stanley EH, Boulton AJ, Findlay S, Marmonier P, Stanley EH, Valett HM. 1998. The Functional Significance of the Hyporheic Zone in Streams and Rivers Maurice Valett Source : Annual Review of Ecology and Systematics , Vol . 29 (1998), pp . 59-81 Published by: Annual Reviews Stable URL : <http://www.jstor.org/stable/221702> REFERENCE. **29**: 59–81
- Brabrand Å, Koestler AG, Borgström R. 2002. Lake spawning of brown trout related to groundwater influx. *Journal of Fish Biology* **60** (3): 751–763 DOI: 10.1006/jfbi.2002.1901

- Briggs MA, Buckley SF, Bagtzoglou AC, Werkema DD, Lane JW. 2016. Actively heated high-resolution fiber-optic-distributed temperature sensing to quantify streambed flow dynamics in zones of strong groundwater upwelling. **52**: 5179–5194 DOI: 10.1002/2015WR018219
- Briggs MA, Lautz LK, McKenzie JM, Gordon RP, Hare DK. 2012. Using high-resolution distributed temperature sensing to quantify spatial and temporal variability in vertical hyporheic flux. *Water Resources Research* **48** (2): 1–16 DOI: 10.1029/2011WR011227
- Byrne GF, Drummond JE, Rose CW. 1967. A sensor for water flux in soil. ‘Point source’ instrument. *Water Resources Research* **3** (4): 1073–1078 DOI: 10.1029/WR003i004p01073
- Ciocca F, Lunati I, Van de Giesen N, Parlange MB. 2012. Heated Optical Fiber for Distributed Soil-Moisture Measurements: A Lysimeter Experiment. *Vadose Zone Journal* **11** (4): 0 DOI: 10.2136/vzj2011.0199
- Constantz J, Stonestrom D a. 2003. Heat as a tracer of water movement near streams. In *Heat as a Tool for Studying the Movement of Ground Water near Streams*, Stonestrom DA, , Constantz J (eds). Reston, Virginia; 1–6. Available at: <http://pubs.usgs.gov/circ/2003/circ1260/#pdf>
- Cuthbert MO, Mackay R, Durand V, Aller MF, Greswell RB, Rivett MO. 2010. Impacts of river bed gas on the hydraulic and thermal dynamics of the hyporheic zone. *Advances in Water Resources* **33** (11): 1347–1358 DOI: 10.1016/j.advwatres.2010.09.014
- Davies AG, Calkins J, Scharenbroich L, Vaughan RG, Wright R, Kyle P, Castaño R, Chien S, Tran D. 2008. Multi-instrument remote and in situ observations of the Erebus Volcano (Antarctica) lava lake in 2005: A comparison with the Pele lava lake on the jovian moon Io. *Journal of Volcanology and Geothermal Research* **177** (3): 705–724 DOI: 10.1016/j.jvolgeores.2008.02.010
- Dent CL, Grimm NB, Fisher SG. 2001. Multiscale effects of surface-subsurface exchange on stream water nutrient concentrations. *Journal of the North American Benthological Society* **20** (2): 162–181 DOI: 10.2307/1468313
- Fisher SG, Grimm NB, Marti E, Gomez R. 1998. Hierarchy, spatial configuration, and nutrient cycling in a desert stream. *Australian Journal of Ecology* **23** (1): 41–52 DOI: 10.1111/j.1442-9993.1998.tb00704.x
- Forman RTT. 1995. Some general principles of landscape and regional ecology. *Landscape Ecology* **10** (3): 133–142 DOI: 10.1007/BF00133027
- Frissell CA, Liss WJ, Warren CE, Hurley MD. 1986. A hierarchical framework for stream

- habitat classification: Viewing streams in a watershed context. *Environmental Management* **10** (2): 199–214 DOI: 10.1007/BF01867358
- Goldstein J. 1999. Emergence as a Construct: History and Issues. **1**: 49–72 DOI: 10.1207/s15327000em0101_4
- Gordon RP, Lautz LK, Briggs MA, McKenzie JM. 2012. Automated calculation of vertical pore-water flux from field temperature time series using the VFLUX method and computer program. *Journal of Hydrology* **420–421**: 142–158 DOI: 10.1016/j.jhydrol.2011.11.053
- Greswell RB, Riley MS, Alves PF, Tellam JH. 2009. A heat perturbation flow meter for application in soft sediments. *Journal of Hydrology* **370** (1–4): 73–82 DOI: 10.1016/j.jhydrol.2009.02.054
- Haghighi E, Or D. 2015. Thermal signatures of turbulent airflows interacting with evaporating thin porous surfaces. *International Journal of Heat and Mass Transfer* **87**: 429–446 DOI: 10.1016/j.ijheatmasstransfer.2015.04.026
- Hare DK, Briggs MA, Rosenberry DO, Boutt DF, Lane JW. 2015. A comparison of thermal infrared to fiber-optic distributed temperature sensing for evaluation of groundwater discharge to surface water. *Journal of Hydrology* **530**: 153–166 DOI: 10.1016/j.jhydrol.2015.09.059
- Hayashi M, Rosenberry D. 2002. Effects of Ground Water Exchange on the Hydrology and Ecology of Surface Water. *Ground Water* **40** (3): 309–316
- Johnson LB, Gage SH. 1997. Landscape approaches to the analysis of aquatic ecosystems. *Freshwater Biology* **37**: 113–132 DOI: 10.1046/j.1365-2427.1997.00156.x
- Kawanishi H. 1983. A soil-water flux sensor and its use for field studies of transfer processes in surface soil. *Journal of Hydrology* **60** (1–4): 357–365 DOI: 10.1016/0022-1694(83)90031-8
- Koestler AG. 1967. *The ghost in the machine*.
- Krause S, Blume T, Cassidy NJ. 2012. Investigating patterns and controls of groundwater upwelling in a lowland river by combining Fibre-optic Distributed Temperature Sensing with observations of vertical hydraulic gradients. *Hydrology and Earth System Sciences* **16** (6): 1775–1792 DOI: 10.5194/hess-16-1775-2012
- Krause S, Boano F, Cuthbert MO, Fleckenstein JH, Lewandowski J. 2014. Understanding process dynamics at aquifer-surface water interfaces: An introduction to the special section on new modeling approaches and novel experimental technologies: Introduction. *Water Resources Research* **50** (2): 1847–1855 DOI: 10.1002/2013WR014755

- Krause S, Lewandowski J, Grimm NB, Hannah DM, Pinay G, McDonald K, Martí E, Argerich A, Pfister L, Klaus J, et al. 2017. Ecohydrological interfaces as hotspots of ecosystem processes. *Water Resources Research* DOI: 10.1002/2016WR019516
- Krause S, Taylor SL, Weatherill J, Haffenden A, Levy A, Cassidy NJ, Thomas PA. 2013. Fibre-optic distributed temperature sensing for characterizing the impacts of vegetation coverage on thermal patterns in woodlands. *Ecohydrology* **6** (5): 754–764 DOI: 10.1002/eco.1296
- Lautz LK, Ribaud RE. 2012. Scaling up point-in-space heat tracing of seepage flux using bed temperatures as a quantitative proxy. *Hydrogeology Journal* **20** (7): 1223–1238 DOI: 10.1007/s10040-012-0870-2
- Lee E, Kang K, Hyun SP, Lee K-Y, Yoon H, Kim SH, Kim Y, Xu Z, Kim D, Koh D-C, et al. 2016. Submarine groundwater discharge revealed by aerial thermal infrared imagery: a case study on Jeju Island, Korea. *Hydrological Processes* **3506** (June): 3494–3506 DOI: 10.1002/hyp.10868
- Lewandowski J, Angermann L, Nützmán G, Fleckenstein JH. 2011. A heat pulse technique for the determination of small-scale flow directions and flow velocities in the streambed of sand-bed streams. *Hydrological Processes* **25** (March): 3244–3255 DOI: 10.1002/hyp.8062
- Lewandowski J, Meinikmann K, Ruhtz T, Pöschke F, Kirillin G. 2013. Localization of lacustrine groundwater discharge (LGD) by airborne measurement of thermal infrared radiation. *Remote Sensing of Environment* **138**: 119–125 DOI: 10.1016/j.rse.2013.07.005
- Lowry CS, Walker JF, Hunt RJ, Anderson MP. 2007. Identifying spatial variability of groundwater discharge in a wetland stream using a distributed temperature sensor. *Water Resources Research* **43** (10): n/a-n/a DOI: 10.1029/2007WR006145
- McBride MS, Pfannkuch HO. 1975. The distribution of seepage within lakebeds. *Journal of Research of the U.S. Geological Survey* **3** (5): 505–512 Available at: <http://scholar.google.com/scholar?hl=en&btnG=Search&q=intitle:Revised+Value+for+the+O18+Fractionation+Between+CO2+and+H2O+at+25#0>
- McDonnell JJ, Sivapalan M, Vache K, Dunn S, Grant G, Haggerty R. 2007. Moving beyond heterogeneity and process complexity: A new vision for watershed hydrology. **43**: 1–6 DOI: 10.1029/2006WR005467
- McKenzie D, Miller C, Falk DA. 2011. *The Landscape Ecology of Fire* (D McKenzie, C Miller, and DA Falk, eds). Springer Netherlands. DOI: 10.1007/978-94-007-0301-8

- Meinikmann K, Lewandowski J, Nützmann G. 2013. Lacustrine groundwater discharge: Combined determination of volumes and spatial patterns. *Journal of Hydrology* **502**: 202–211 DOI: 10.1016/j.jhydrol.2013.08.021
- Nakayama T, Watanabe M. 2008. Missing role of groundwater in water and nutrient cycles in the shallow eutrophic Lake Kasumigaura, Japan. *Hydrological Processes* **22**: 1150–1172 DOI: 10.1002/hyp.6684
- O'Neill RV, Johnson AR, King AW. 1989. A hierarchical framework for the analysis of scale*. *Landscape Ecology* **3** (3381): 193–205
- Poole GC. 2002. Fluvial landscape ecology: Addressing uniqueness within the river discontinuum. *Freshwater Biology* **47** (4): 641–660 DOI: 10.1046/j.1365-2427.2002.00922.x
- Poole GC, Berman CH. 2001. An Ecological Perspective on In-Stream Temperature : Natural Heat Dynamics and Mechanisms of Human-Caused Thermal Degradation. **27** (6): 787–802 DOI: 10.1007/s002670010188
- Pöschke F, Lewandowski J, Engelhardt C, Preuß K, Oczipka M, Ruhtz T, Kirillin G. 2015. Upwelling of deep water during thermal stratification onset—A major mechanism of vertical transport in small temperate lakes in spring? *Water Resources Research* **51** (January 2016): 9612–9627 DOI: 10.1002/2015WR017579
- Read T, Bour O, Selker JS, Bense VF, Le Borgne T, Hochreutener R, Lavenant N. 2014. Active-Distributed Temperature Sensing to continuously quantify vertical flow in boreholes. *Water Resources Research* **50**: 3706–3713 DOI: 10.1002/2014WR015273
- Ren T, Kluitenberg GJ, Horton R. 2000. Determining Soil Water Flux and Pore Water Velocity by a Heat Pulse Technique. *Soil Science Society of America Journal* **64** (2): 552–560 DOI: 10.2136/sssaj2000.642552x
- Salthe SN. 1985. *Evolving hierarchical systems: Their structure and representation*. Columbia University Press: New York.
- Schmidt C, Bayer-Raich M, Schirmer M. 2006. Characterization of spatial heterogeneity of groundwater-stream water interactions using multiple depth streambed temperature measurements at the reach scale. *Hydrology and Earth System Sciences Discussions* **3** (4): 1419–1446
- Selker JS, van de Giesen N, Westhoff M, Luxemburg W, Parlange MB. 2006a. Fiber optics opens window on stream dynamics. *Geophysical Research Letters* **33** (24): L24401 DOI: 10.1029/2006GL027979
- Selker JS, Thévenaz L, Huwald H, Mallet A, Luxemburg W, van de Giesen N, Stejskal M,

- Zeman J, Westhoff M, Parlange MB. 2006b. Distributed fiber-optic temperature sensing for hydrologic systems. *Water Resources Research* **42** (12): n/a-n/a DOI: 10.1029/2006WR005326
- Shaw RD, Shaw JFH, Fricker H, Prepas EE. 1990. An integrated approach to quantify groundwater transport of phosphorus to Narrow Lake , Alberta. **35** (4): 870–886
- Simon HA. 1977. The Organization of Complex Systems. In *Models of Discovery: And Other Topics in the Methods of Science* Springer Netherlands: Dordrecht; 245–261. DOI: 10.1007/978-94-010-9521-1_14
- Simon HA. 1997. *The sciences of the artificial, (third edition)*. DOI: 10.1016/S0898-1221(97)82941-0
- Soranno PA, Webster KE, Cheruvilil KS, Bremigan MT. 2009. The lake landscape-context framework : linking aquatic connections , terrestrial features and human effects at multiple spatial scales. *Verh. Internat. Verein. Limnol.* **30** (January): 695–700
- Soranno P a., Cheruvilil KS, Webster KE, Bremigan MT, Wagner T, Stow C a. 2010. Using Landscape Limnology to Classify Freshwater Ecosystems for Multi-ecosystem Management and Conservation. *BioScience* **60** (6): 440–454 DOI: 10.1525/bio.2010.60.6.8
- Timothy F. Allen. A summary of the principles of hierarchy theory Available at: <http://www.isss.org/hierarchy.htm>
- Turner MG. 1989. Landscape Ecology: The Effect of Pattern on Process. *Annual Review of Ecology and Systematics* **20** (1): 171–197 DOI: 10.1146/annurev.es.20.110189.001131
- Urban DL, Neill RVO, Shugart HH. 1987. Ecology Landscape spatial patterns. *BioScience* **37** (2): 119–127
- Warren DR, Sebestyen SD, Josephson DC, Lepak JM, Kraft CE. 2005. Acidic Groundwater Discharge and in Situ Egg Survival in Redds of Lake-Spawning Brook Trout. *Transactions of the American Fisheries Society* **134** (5): 1193–1201 DOI: 10.1577/T04-180.1
- Wawrzyniak V, Piégay H, Allemand P, Vaudor L, Goma R, Grandjean P. 2016. Effects of geomorphology and groundwater level on the spatio-temporal variability of riverine cold water patches assessed using thermal infrared (TIR) remote sensing. *Remote Sensing of Environment* **175**: 337–348 DOI: 10.1016/j.rse.2015.12.050
- Wu J. 1999. Hierarchy and scaling: extrapolating information along a scaling ladder. *Canadian Journal of Remote Sensing* **25** (4): 367–380
- Wu J. 2013. Hierarchy Theory: An Overview. In *Linking Ecology and Ethics for a Changing*

World: Values, Philosophy, and Action, Rozzi R, , Pickett STA, , Palmer C, , Armesto JJ, , Callicott JB (eds). Springer Netherlands: Dordrecht; 281–301. DOI: 10.1007/978-94-007-7470-4_24

Wu J, David JL. 2002. A spatially explicit hierarchical approach to modeling complex ecological systems : theory and applications. **153**: 7–26

Wu J, Levin SA. 1997. A patch-based spatial modeling approach : conceptual framework and simulation scheme. **101**: 325–346

Wu J, Loucks OL. 1995. From Balance of Nature to Hierarchical Patch Dynamics : A Paradigm Shift in Ecology. *The quarterly review of biology* **70** (4): 439–466 DOI: 0033-5770/95/7004-0003

Annex S1: Definitions

System: Any interacting, interdependent or associated group of entities.

Context: set of circumstances and facts that surround particular event or situation.

Systems' context: encompassing element structure (Poole, 2002).

Hierarchy: Any system of things ranked one above another.

Hierarchic system: system formed by interrelated subsystems (Simon, 1997).

Entity: component (O'Neill et al. 1989) or subsystem.

Levels: A section of a hierarchy which is defined by a scale (Allen and Starr 1982, 1996). Within a level there are entities whose features characterize the level they are part of. An entity can belong to any amount of levels depending on the criteria used to unite levels above and below (Timothy F. Allen).

Scalar hierarchy: Empirically based levels of observations (Ahl and Timothy F. Allen, 1996).

Definitional hierarchy: Observer defined level of organization (Ahl and Timothy F. Allen, 1996).

Scalar levels: in a scalar hierarchy.

Definitional levels: in a definitional hierarchy.

Patch: Basic homogeneous unit observable in the landscape at a certain spatial scale. A patch can change its dynamic, structure, arrangement, union or function (Poole, 2002). Patch might be analog to entity, subsystem, Holon, component or part. These terms are commonly used in Hierarchy Theory.

Processes: Water and heat exchange processes.

Trans-scale: across scales.

Trans-interface: across interfaces.

Elements: Patches, parts of the system.

System elements: system patches.

Structural elements: Structural patches.

Element's ecological function: Patch's ecological function (Poole, 2002).

A landscape: A dynamic interaction of terrestrial and aquatic elements/patches (Forman, 1995).

Top-down process: They influence the internal structure of the system. Processes influence by patch function/condition at coarse scales but influences patch function/condition at finer scales (Poole, 2002).

Top-down constrains/influences: e.g. Environmental constrains. Each of the constrains provides a context for the behaviors of the lower levels of the hierarchy (Urban *et al.*, 1987; Wu, 2013).

Bottom up process: Processes are influenced by fine scale patch's function/condition but influence patch function/conditions at coarser scales (Poole, 2002).

Bottom up mechanism: initiating forces at lower levels of the hierarchy (Wu 2013).

Emergent properties: properties that emerge via collective actions of many individual entities. Arise of a novel and coherent structures, patterns and properties during the process of self-organization in complex systems (Goldstein, 1999).

Holon: Subsystem that comprise a level (Koestler, 1967).

Interface: Surface regarded as common boundary of two spaces, phases.

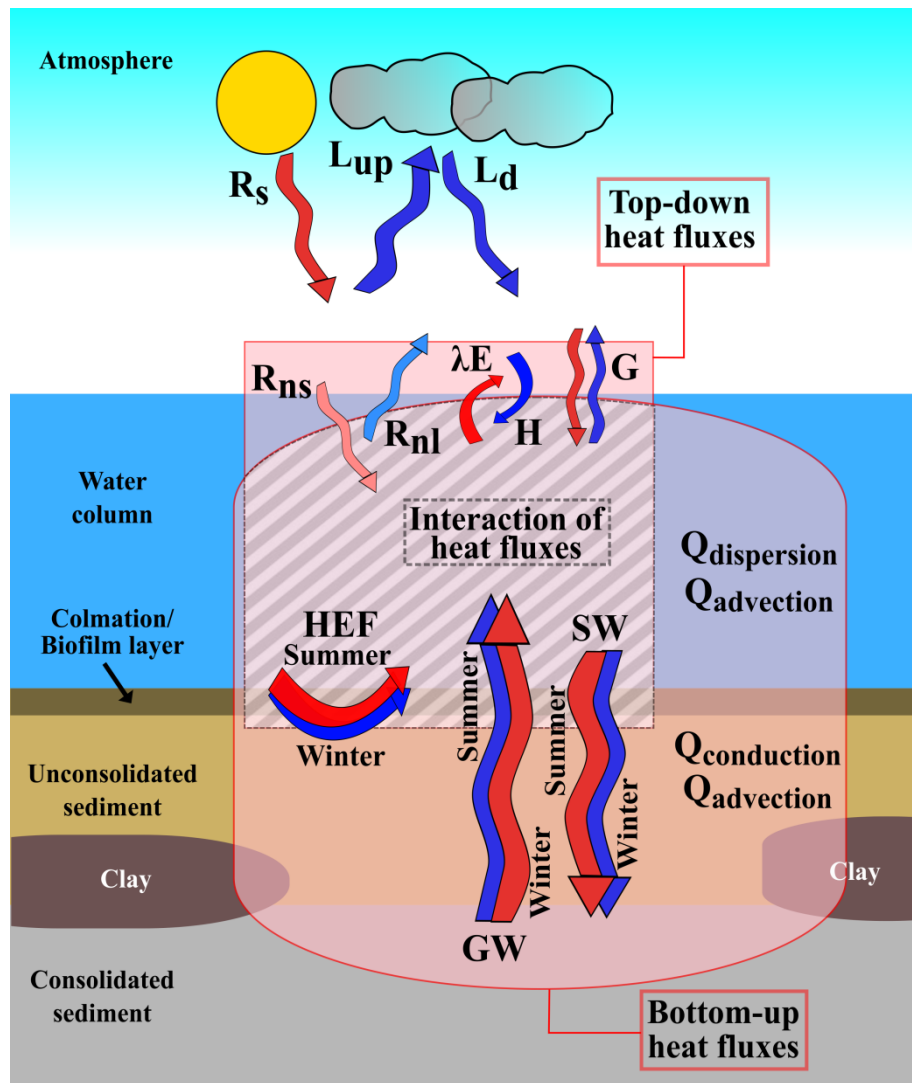
Compartment: Phase= bodies, spaces.

Sister Holon: two communicating Holon which occur at the same level in a hierarchy and do not exert constrain over each other (Allen and Starr 1982).

Interactions among Holons of same level are symmetric, among components within a Holon are stronger and more frequent than those among Holons (Koestler, 1967; Allen and Starr, 1982).

In **HPD** and patch dynamics, patch refers to the term Holon which is used in hierarchy theory.

Graphical abstract



G: Net heat flux across the water surface
R_{ns}: Net shortwave radiation
R_{nl}: Net longwave radiation
R_s: Shortwave radiation
L_{up}: Upwards longwave radiation
L_d: Downwards longwave radiation
Q: Heat flux
λE: Latent heat flux
H: Sensible heat flux
GW: Groundwater
SW: Surface water
HEF: Hyporheic exchange flow

3 Mesocosm experiments identifying hotspots of groundwater upwelling in a water column by fiber optic distributed temperature sensing

Amaya I. Marruedo Arricibita^{a,b}, Stefan Krause^c, Jesus Gomez-Velez^d, David M. Hannah^c and Jörg Lewandowski^{a,b}

^a Department of Ecohydrology, Leibniz-Institute of Freshwater Ecology and Inland Fisheries, 12587 Berlin, Germany.

^b Department of Geography, Humboldt University of Berlin, 10099 Berlin, Germany.

^c School of Geography, Earth and Environmental Sciences, University of Birmingham, B15 2TT Birmingham, United Kingdom.

^d Department of Earth and Environmental Science, New Mexico Institute of Mining & Technology, Socorro, NM 87801; United States.

Published in: Hydrological Processes

Marruedo Arricibita AI, Krause S, Gomez-Velez J, Hannah DM, Lewandowski J. 2018. Mesocosm experiments identifying hotspots of groundwater upwelling in a water column by fibre optic distributed temperature sensing. *Hydrological Processes* 32 (2): 185–199 DOI: 10.1002/hyp.11403

This is an open access article under the terms of the Creative Commons Attribution License, which permits use, distribution and reproduction in any medium, provided the original work is properly cited.

© 2017 The Authors. *Hydrological Processes* Published by John Wiley & Sons Ltd.

Abstract

Lacustrine groundwater discharge (LGD) can substantially impact ecosystem characteristics and functions. Fibre optic distributed temperature sensing (FO - DTS) has been successfully used to locate groundwater discharge into lakes and rivers at the sediment-water interface, but locating groundwater discharge would be easier if it could be detected from the more accessible water surface. So far, it is not clear if how and under which conditions the LGD signal propagates through the water column to the water surface-atmosphere interface, and what perturbations and signal losses occur along this pathway. In the present study, LGD was simulated in a mesocosm experiment. Under winter conditions, water with temperatures of 14 to 16 °C was discharged at the bottom of a 10 × 2.8 - m mesocosm. Water within this mesocosm ranged from 4.0 to 7.4 °C. Four layers (20, 40, 60, and 80 cm above the sediment) of the 82 cm deep mesocosm were equipped with FO - DTS for tracing thermal patterns in the mesocosm. Aims are (a) to test whether the positive buoyancy of relatively warm groundwater imported by LGD into shallow water bodies allows detection of LGD at the lake's water surface-atmosphere interface by FO - DTS, (b) to analyse the propagation of the temperature signal from the sediment - water interface through the water column, and (c) to learn more about detectability of the signal under different discharge rates and weather conditions. The experiments supported the benchmarking of scale dependencies and robustness of FO - DTS applications for measuring upwelling into aquatic environments and revealed that weather conditions can have important impacts on the detection of upwelling at water surface-atmosphere interfaces at larger scales.

Keywords

lake, FO - DTS, heat tracer, jet, interface, driver

3.1 Introduction

Lacustrine groundwater discharge (LGD), that is, the discharge of groundwater (GW) into lakes, can substantially impact ecosystem characteristics and functions (Baker et al., 2014; Ridgway & Blanchfield, 1998; Warren, Sebestyen, Josephson, Lepak, & Kraft, 2005). Upwards directed GW flow is sometimes called upwelling, especially in the context of hyporheic zones, where commonly both upwelling and downwelling occur along river reaches. In the present manuscript, we use the term upwelling solely for upward transport processes in the water column; this definition is adopted from limnophysics. On the one hand, upwelling of warm water in cold lakes can be caused by natural processes such as GW flow across the lake bed into the cold lake water body during winter conditions (LGD; Lewandowski, Meinikmann, Ruhtz, Pöschke, & Kirillin, 2013) or thermal springs in volcanic lakes (Cardenas et al., 2012). On the other hand, it can be related to thermal pollution caused by industries such as electric power plants, which use water and discharge heated water into lakes and streams (Hung, Eldridge, Taricska, & Li, 2005; Shuster, 1986). In both cases, quantitative interpretations of warm water upwelling patterns are hampered by the lack of understanding of how the signal propagates from the sediment–water interface through the water column to the water surface–atmosphere interface and which perturbations and signal losses occur along this pathway. The present study will focus on LGD as an example of upwelling of warm water in lacustrine ecosystems during winter conditions due to its substantial impact on the ecosystem characteristics and functioning. LGD creates favourable habitats by affecting water chemical composition and temperature, supporting for instance the spawning of fish (Brunke & Gonser, 1997; Hayashi & Rosenberry, 2002). As climate warms, aquatic environments with strong GW influence are expected to support habitat stability and provide refuge for thermally stressed-aquatic species (Brabrand, Koestler, & Borgström, 2002; Curry & Noakes, 1995; Hayashi & Rosenberry, 2002). Furthermore, detection of LGD is essential with respect to identifying it as a potential vector for pollution in aquatic ecosystems when GW quality is degraded (Nakayama & Watanabe, 2008). Despite the reported relevance of LGD on ecosystems, very little has been written about discharge of warm GW to lakes. Nearly all of the literature discusses discharge of cold GW to warm lakes, primarily because most of the research has been conducted during warm-water periods. Relatively cold GW has a higher density than warm lake water and, thus, would not reach the water surface.

There are no detailed field observations of how warm water propagates through the water column and to the surface of the lake during winter conditions. We address this research gap

by looking at trigger conditions that allow upwelling of LGD from the sediment–water interface to the water surface atmosphere interface. We consider the temperature difference required between GW and surface water (SW) as well as the influence of meteorological conditions and diurnal cycles. The different temperatures of GW and SW might allow the detection of potential discrete areas of GW discharge to SW (Hare, Briggs, Rosenberry, Boutt, & Lane, 2015). Under the prerequisite of similar ion composition (which impacts water density), warm GW is less dense and more buoyant than cold SW, which allows upwelling of GW to the water surface. Thus, heat convection is augmented by density driven buoyant forces where warm GW discharges to cold SW. This process occurs during winter and early spring when SW is substantially colder than discharging GW and when the mixing is at a minimum at the lake surface (Hare et al., 2015; Lewandowski et al., 2013).

The basic concept of fibre optic distributed temperature (FO-DTS) technology is to analyse the temperatures monitored along specific distance intervals of a fibre optic cable based on (a) the travelling time of light in the optic fibre and (b) the temperature-dependent backscattering of light in the fibre (Selker, van de Giesen, Westhoff, Luxemburg, & Parlange, 2006). In this way, temperature can be monitored through the fibre optic cable up to a distance of several km, with spatial resolutions ranging from 0.3 to 4 m and measurement precision of 0.05 to 0.1 °C when sampling over 30-s intervals (Hausner et al., 2011; Selker, Thévenaz, et al., 2006; van de Giesen et al., 2012). FO-DTS has been used to detect GW discharge at the sediment–water interface of lakes (Blume, Krause, Meinikmann, & Lewandowski, 2013; Liu, Liu, Wang, & Zheng, 2015; Sebok et al., 2013) and streams (Krause, Blume, & Cassidy, 2012; Lowry, Walker, Hunt, & Anderson, 2007). Here, FO-DTS is placed in layers of a specific depth above the sediment–water interface, to provide high-resolution temperature data to quantify the incidence, frequency, persistence, and attenuation of warmer discharging GW that reaches the water surface.

The aim of this study is to show that during winter, the positive buoyancy of relatively warm LGD to cold SW will allow or enhance detection of GW at the water surface–atmosphere interface (the lake surface). To address this aim, a mesocosm was used as a model system. Different layers of FO-DTS cable were deployed at different water depths to measure the temperature distribution. In addition, the following questions are addressed:

1. Which lake-internal upwelling patterns from the sediment–water interface through the water column to the water surface–atmosphere interface are caused by (simulated) LGD?

2. What are the intensities of (simulated) LGD at which GW signals can be identified at the water surface with FO-DTS?
3. What is the impact of weather conditions on detection of LGD at the water surface–atmosphere interface?

This paper addresses the research questions by (a) qualitative analysis of FO-DTS data, (b) statistical analysis of the FO-DTS data in order to describe temperature hotspots and significant spatial patterns across the water column, and (c) quantification of the effect of different weather conditions, injection rates, and the diurnal cycle on the net heat fluxes across the water surface (G , $W\ m^{-2}$) as well as the energy change due to advective transport by the water inlet from the lake and the water outlet from the mesocosm (E_{adv} in MJ) and the change of internal energy in the mesocosm (ΔE in MJ). Section 4 presents a conceptual model based on analyses and limitations of FO-DTS data. The conclusions of the paper will summarize briefly the findings on the different data analyses carried out, answering the three research questions.

3.2 Material and methods

3.2.1 Experimental setup

The mesocosm is composed of two inlets and one outlet (see Figure 3.1). Through one inlet water from Lake Müggelsee with a mean temperature of $4.7\ ^\circ C$ was discharged with a rate of $33\ L\ min^{-1}$. The inlet was open throughout the experiment in order to keep homogeneous and relatively constant water temperatures and water levels. The second inlet comprised a hosepipe that was deployed on the bottom of the mesocosm to provide the warm water ($14\text{--}16\ ^\circ C$ measured at halfway between tap and mesocosm) injection. The hosepipe was insulated with insulation foam in order to reduce cooling of the injected water along the flow path from the tap (located in a building close to the mesocosm, 65-m distance). A nozzle was connected to the end of the hose and covered with a bag ($35 \times 35\ cm$) filled with sediment in order to most realistically simulate discrete LGD at the sediment–water interface. Finally, an outlet on the opposite side to the cold water inlet assured a constant water level in the mesocosm of 0.82 m height. The outlet discharge rates varied from 34 to $48\ L\ min^{-1}$ depending on the applied warm water injection rate. An aluminium frame with dimensions: $4\ m \times 2\ m$ and 1.5 m height was used to deploy the FO-DTS cable at different water depths (Figure 3.1). The FO cable was installed in four layers at different heights: 20, 40, 60, and 80 cm (Layers 1, 2, 3, and 4, respectively) above the bottom of the mesocosm (Figure 3.1). The

FO-DTS cable was routed back and forth across the aluminium frame in a rectangular grid formation so that 15 parallel reaches of the cable extended across each layer within the mesocosm. Temperatures were averaged over 12.5 cm intervals (sampling resolution) along the FO-DTS cable. We acknowledge that the presence of the FO cable may alter the flow of water and heat within the mesocosm; however, considering the cable volume (0.009%) compared to the water volume and the spacing between cables (at least 12.5 cm), the effect is probably minor.

From March 11, 2015, to March 27, 2015, seven 24 hr temperature datasets were obtained: one control dataset without warm water injection under overcast conditions; three datasets with 1 L min^{-1} injection rate, under clear, partly cloudy, and overcast conditions, respectively; two datasets with 5 to 5.5 L min^{-1} injection rate, under clear and overcast conditions, respectively; and finally, one dataset with 15 L min^{-1} injection rate under overcast conditions.

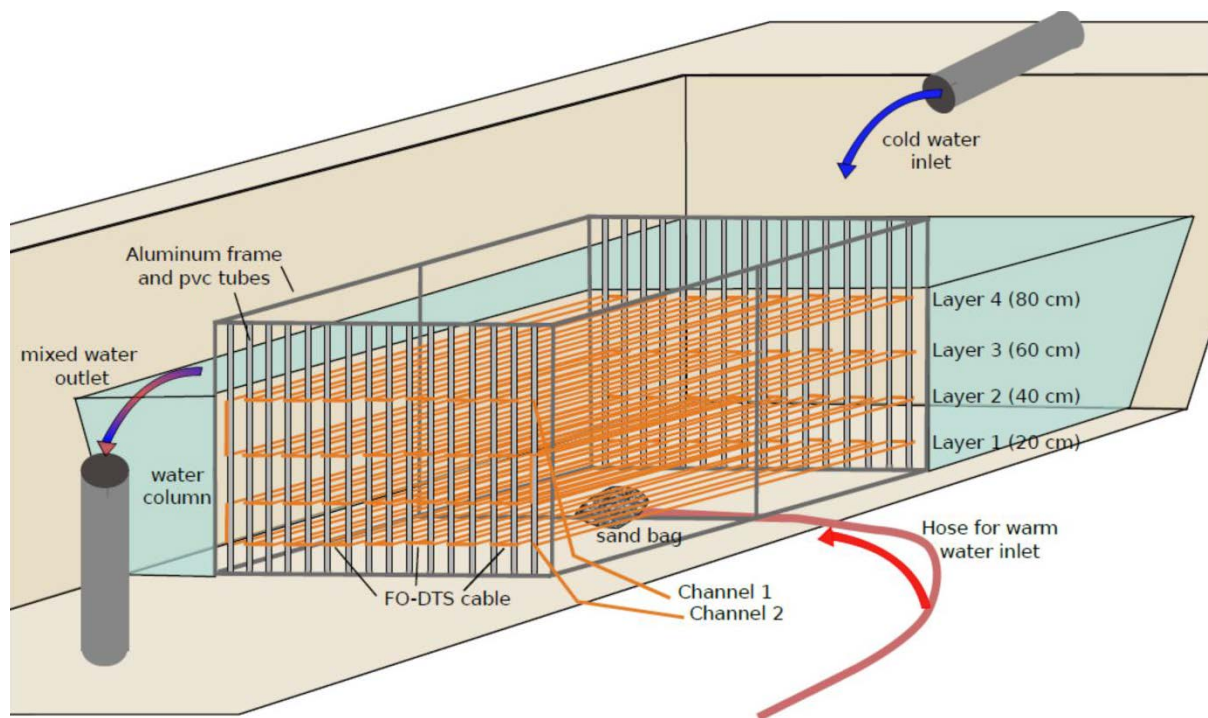


Figure 3.1 Sketch of the experimental set up showing a cross section through the mesocosm including the fibre optic distributed temperature sensing set up.

Measurements were carried out using an ULTIMA-S DTS (SILIXA Ltd.) with a sampling resolution of 12.5 cm and spatial resolution of approximately 30 cm. DTS sampling resolution depends on the duration of each of the laser pulses sent by the DTS. For example, a DTS sending laser pulses of 10 ns has a sampling resolution of 1 m, the ULTIMA-S, with a

sampling resolution of 12.5 cm, sends pulses of 1.25 ns. The spatial resolution refers to the distance between points along the FO cable located next to an abrupt change on temperature in a way that the point on the low side is not placed higher than 10% of the abrupt jump and the point on the high side is placed higher than 90% of the abrupt jump (Selker, Tyler, & Van de Giesen, 2014). Five hundred metres of multimode FO cable from Silixa Ltd., were deployed for the experiments of this study. Using a multimode fibre allowed flexible bending and thus supported an adequate set up of the cable in the aluminium frame.

Simulated upwelling flux rates versus rates reported in literature

The LGD rates used in the present study are based on measured flow rates in the tube (1 to 15 L min⁻¹) used for injecting warm water into the mesocosm. The tube outlet is covered by a sand bag to simulate discrete LGD from sediments. An uncovered tube outlet might have caused a jet stream that would be quite unrealistic for LGD and therefore was avoided. The LGD rate can be referred to different areas: (a) the sand bag covering the tube outlet (35 × 35 cm) resulting in 8.2 to 122.4 L m⁻² min⁻¹, (b) a square metre, that is, 1 to 15 L m⁻² min⁻¹, and (c) the entire mesocosm (10 × 2.8 × 0.82 m) resulting in 0.036 to 0.536 L m⁻² min⁻¹. The latter approach is often used in lake studies in which the total exfiltration is related to the entire lakebed.

The LGD rates applied in the present mesocosm experiment are at the upper end of LGD rates occurring in situ. Rosenberry, Lewandowski, Meinikmann, and Nützmann (2015) reviewed the international literature and report a median exfiltration rate of 0.74 cm day⁻¹ (=0.005 L m⁻² min⁻¹) and a maximum of 745 cm day⁻¹ (=5.2 L m⁻² min⁻¹). The maximum of 745 cm day⁻¹ is a point estimate based on seepage metre measurements (Kidmose, Engesgaard, Nilsson, Laier, & Looms, 2011). A high rate referred to the entire lake bed is reported by Piña-Ochoa and Lvarez-Cobelas (2009), which is 0.05 to 0.1 L m⁻² day⁻¹. For punctual focused LGD much higher rates are possible: For example, in Norrström and Jacks (1996) macropore GW discharge rates of 18 and 42 L min⁻¹ are reported for areas of 0.0078 and 0.031 m². More extreme examples can be found in natural thermal ponds or pools with hot springs with up to 800 L min⁻¹ discharge rates (Haselwimmer, Prakash, & Holdmann, 2013). Intense warm water discharge might also be of anthropogenic origin such as sewage leakage from under water pipes (Apperl, Pressl, & Schulz, 2017).

Measurement protocol and calibration

Once the FO cable was properly deployed onto the aluminium frame, the exact start and end positions of each cable line were identified.

This was done by locally warming the cable at each bend, identifying the temperature peak on the data output graph, and noting the distance along the cable at this peak. This allowed locating of each of the four fibre optic layers, including their start and end points, as well as the beginning and end of each FO cable sequence.

Calibration of the FO-DTS by temperature offset correction was carried out using an external probe of the DTS device and FO cable reference sections within an isolated ice bath with a mix of ice and water that assured constantly 0 °C. For the differential loss correction, the fixed value setting was chosen along the relatively short cable (500 m) without any splices. A default value of 0.255 dB/km was used as this value is the expected value for Corning ClearCurve™ OM3 fibre.

An alternate single-ended measurement set up was used with alternating monitoring direction of the light pulse sent from the DTS device. Measurements were averaged at 10-s intervals (integration time) in each direction. This means that the time interval between measurements from the same channel was 20 s.

3.2.2 Data analyses and spatial statistics

All data analysis, including summarizing statistics for quantification of spatial patterns and statistical relationships of observed data within layers and between layers, was conducted in R and ArcGIS. The following spatial statistical metrics were quantified:

Moran's I and Moran Scatter Plot of testing spatial autocorrelation

The Moran's I values were calculated as indicators of the degree of linear association between a value in a specific location (x-axis) and surrounding locations (y-axis). Moran's I scatter plots were used to visualize the type and strength of spatial autocorrelation of observed temperatures. The four quadrants of the Moran's I scatter plot indicate, from x-axis to y-axis: high-high and low-low quadrants contain values with positive spatial autocorrelation and high-low and low-high quadrants contain values with negative spatial autocorrelations. The Moran's I scatter plot displays a “spatially lagged” transformation of a variable (in y-axis) on the original spatial variable (in x-axis). In addition, the Moran's I scatter plot reports the summary of potential influential observations (highlighted in red diamond shape in Moran's I scatter plot) for the linear relationship between the data and the lag. Finally, the slope of the scatter plot indicates Moran's I values obtained and the overall spatial autocorrelation of the dataset (Anselin, 1996; Bivand, Pebesma, & Gómez-Rubio, 2013).

Local Indicators of Spatial Association maps

Local indicators of spatial association (LISA) have been calculated to identify significant spatial clusters or outliers that have been used in this study to highlight local hotspots of simulated warm water upwelling. The clusters and spatial outliers of LISA maps correspond to the four quadrants of the Moran's I scatter plots, providing a measure of clusters or outliers that are of statistical significance (Anselin, 1995).

Spatial correlation between layers: Band collection statistics

Band collection statistics conducted in ArcGIS allowed the analysis of sets of raster bands, in the present study a set of 4 FO-DTS temperature layers. Covariance and correlation matrices and basic statistical parameters (minimum, maximum, mean, and standard deviation) for each layer have been calculated. The covariance matrix indicates for each layer how much variance is from the mean value of each layer. The correlation matrix shows how correlated the cell values of one layer are to the cell values of another layer (Environmental Systems Research Institute, 2014).

3.2.3 Preprocessing and sources of error

Figure 3.2a shows temperature data of a single measurement point on the FO cable over 24 hr of measurement (black line) with a clear diurnal trend. However, noise is predominant on the plotted curve. Noise can be related to the sensor, turbulence, and short time fluctuations of weather conditions (sunlight/no sunlight). In order to clear the temperature signal, local polynomial regression fitting (LOESS) was applied in R. The red line in Figure 3.2a represents the fitted curve. Applying LOESS to the raw temperature resulted in removal of noise from the data ranging from 0.0 to 0.6 °C (Figure 3.2b).

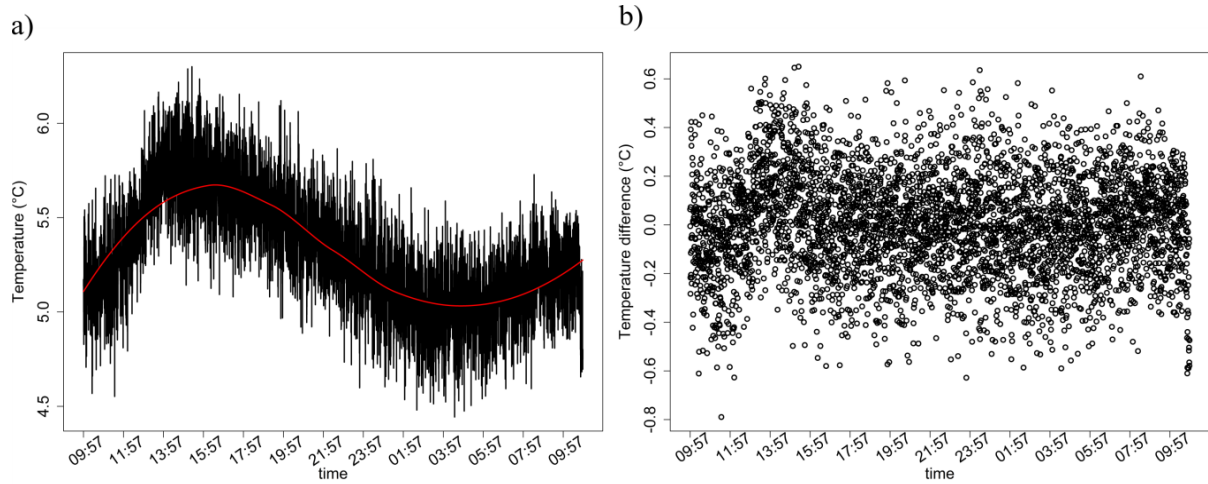


Figure 3.2 (a) Raw temperature data (black line) and smoothed temperature data with local polynomial regression fitting (LOESS; red line) and (b) temperature difference between raw temperature data and smoothed temperature data.

3.2.4 Quantification of net heat fluxes across the water surface, advective heat fluxes and internal energy change

In order to identify the main drivers affecting the spatial patterns observed within the water column (Figure 3.3), heat losses and gains at the mesocosm surface have been quantified. Steady state water flow of the mesocosm has been assumed. G , ΔE , and net-advective heat flux (E_{adv} in MJ) have been calculated following equations in Appendix S1. E_{adv} consists of cold and warm water inputs to the mesocosm and the water flow out of the mesocosm.

3.3 Results

3.3.1 FO-DTS observed temperature patterns

Spatial linear interpolations of time averaged values (day and night separately) from 24-hr measurements are shown in Figure 3.3. The slice3D plots integrate the four layers of FO-DTS temperature measurements. The plots show the temperature differences from the minimum temperatures (ΔT_{min} in degrees [°C]) of each dataset with the same colour scale for both day and night. Because the present figure is focusing on spatial patterns of warm water upwelling, and not on quantifying upwelling per se, we did not use absolute temperature values. In addition, ΔT_{min} values show the intensity of the warm water hotspots in the water column and in the water surface for all three injection rates in each dataset. The plots allow tracing of the warm water injected at the bottom of the mesocosm with rates of 1, 5–5.5, or 15 L min⁻¹, respectively, and its propagation through the water column. These plots represent averaged values of measurements taken during day and night separately. Figure 3.3a–c represents the

ΔT_{\min} observed in experiments under clear or partly cloudy conditions. Although the source of warm water can clearly be detected at the bottom of the mesocosm, its impact on observed ΔT_{\min} spatial patterns is vanishing with increasing distance from the source in the upper layers. In contrast, Figure 3.3d–f represents ΔT_{\min} observed in each experiment under overcast conditions. Injected warm water can be traced in all four layers at all applied injection rates: 1, 5, and 15 L min⁻¹. In addition, night measurements show clearer spatial patterns than day measurements. Finally, depending on the applied injection rate, the upwelling of warm water from the bottom shows different flow paths (see Figure 3.3d–f). The different flow paths observed in Figure 3.3d–f are related to the cold water inlet on the right side of the mesocosm. The cold water inlet created a vortex from the right side of the mesocosm to left, and the injected warm water moved along with this vortex. In Figure 3f, this effect is also visible on the top layer. Due to the high injection rate (15 L min⁻¹), the warm water flows straight up to the SW in Figure 3.3f.

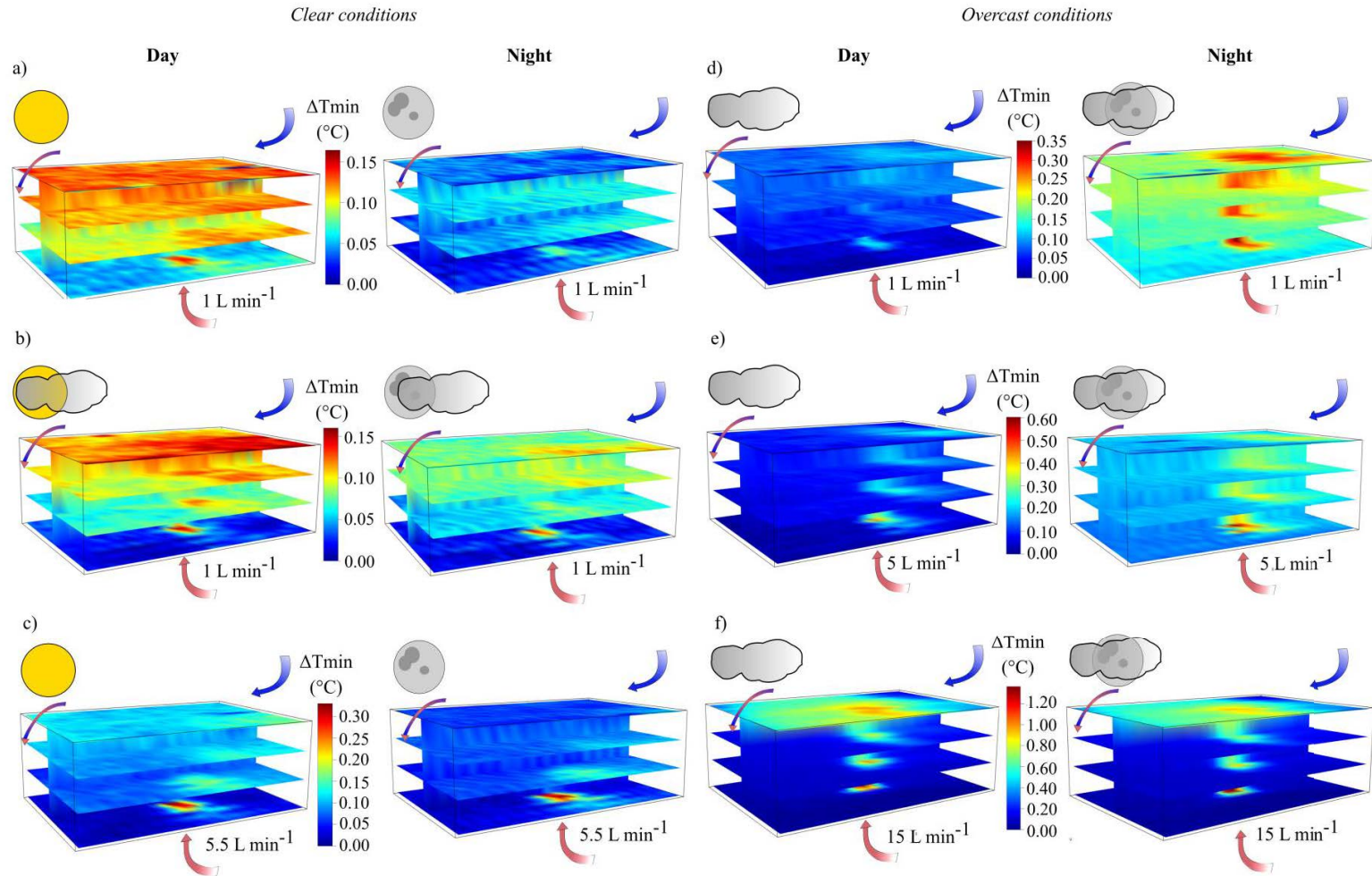


Figure 3.3 Slice3D plots visualizing for the four layers of DTS measurements the difference from the minimum temperature of each dataset. Values averaged for approximately 12 hr day (always left of colour scale) or night (always right), respectively. Different injection rates and weather conditions as follows: (a) 1 L min⁻¹ clear 19.03.2015, (b) 1 L min⁻¹ partly cloudy 25.03.2015, (c) 5.5 L min⁻¹ clear 18.03.2015, (d) 1 L min⁻¹ overcast 26.03.2015, (e) 5 L min⁻¹ overcast 27.03.2015, and (f) 15 L min⁻¹ overcast 12.03.2015. inlet of cold lake water, inlet of warm water, outlet of mixed water from mesocosm. clear day, clear night, partly cloudy day, partly cloudy night, overcast day, and overcast night.

3.3.2 Quantitative analysis of spatial temperature patterns

Horizontal spatial temperature patterns: Spatial autocorrelation within layers: Moran's I scatter plots and LISA maps

All datasets show significant spatial autocorrelation between data points within each layer with p values less than 2.2×10^{-16} , except the dataset of Layer 3 at an injection rate of 1 L min^{-1} at night under clear sky conditions where the p value is 1.18×10^{-6} . As an example, Figure 3.4 compares the Moran's I scatter plots and LISA maps during daytime for 1 L min^{-1} clear sky and 15 L min^{-1} overcast sky conditions. When injecting 1 L min^{-1} with clear sky conditions, despite the significant spatial autocorrelation, the temperature data values are more dispersed over the four quadrants. Figure 3.4a indicates potential influential observations in Layers 1 and 2, mainly located in the quadrant “high-high,” identifying a positive spatial autocorrelation between observation points surrounding those data values. However, in Layers 3 and 4 (Figure 3.4a), the distribution of potential influential observations over the four quadrants is more dispersed, not showing a clear clustering of points on “high-high” and “low-low” quadrants (in red and yellow in LISA maps, Figure 3.4c).

On the contrary, temperatures observed for the 15 L min^{-1} injection rate show stronger spatial autocorrelation with most of the data points in high-high and low-low quadrants indicating a positive spatial autocorrelation (Figure 3.4b and 3.4d). Thus, the spatial autocorrelation over the four layers is stronger than in the dataset of 1 L min^{-1} and clear sky condition. Furthermore, LISA maps (Figure 3.4d) show a clear clustering of the highly spatially autocorrelated values.

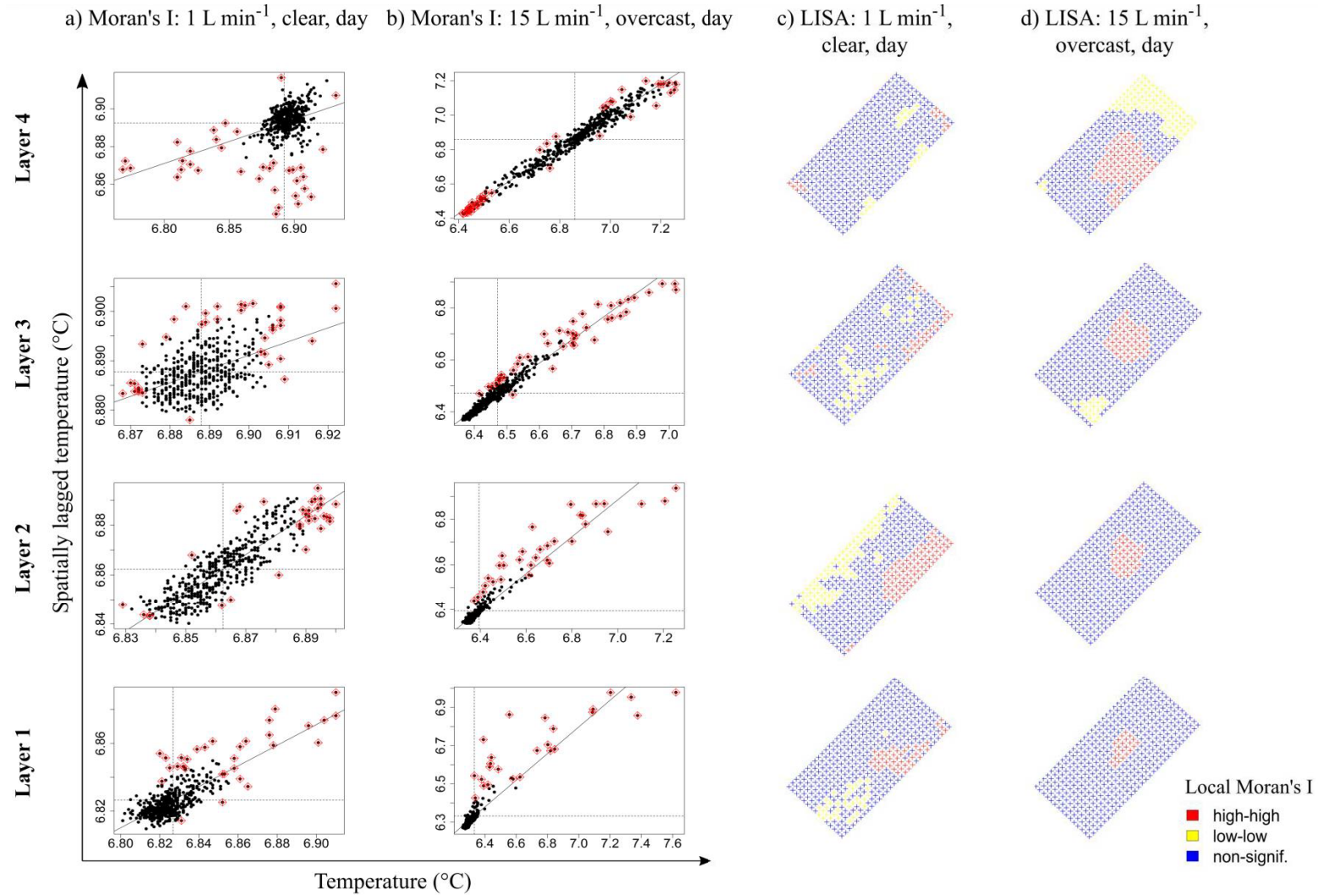


Figure 3.4 (a) and (b) Moran's I scatterplots, (c) and (d) LISA maps, (a) and (c) for 1 L min⁻¹ clear sky, day, (b) and (d) for 15 L min⁻¹ overcast sky, day. In (a) and (b), potential influencing measures for the linear relationship between the data and the lag are highlighted as red diamond shape. In (c) and (d), red coloured points belong to the high-high quadrant in Moran's I scatterplot, yellow coloured points belong to the low-low quadrant in Moran's I scatterplot, and blue coloured points are spatially nonsignificant points. From top row to bottom row: Layers 4, 3, 2, and 1.

Calculated Moran's I values in Figure 3.5 compare the intensity of spatial autocorrelation between the temperature data points for different weather conditions and day or night observations within each layer. In all cases, Moran's I values increase from the lowest to the highest injection rates (Figure 3.5). The injection of warm water has a larger impact on the temperature patterns observed in the upper layers at higher injection rates. In general, all layers show highest Moran's I values when the measurements were obtained under overcast weather conditions. Layers 3 and 4 (uppermost layers in the water column) show the highest increase in Moran's I values under overcast weather conditions at injection rates of 1 and 5 L min^{-1} injection rates.

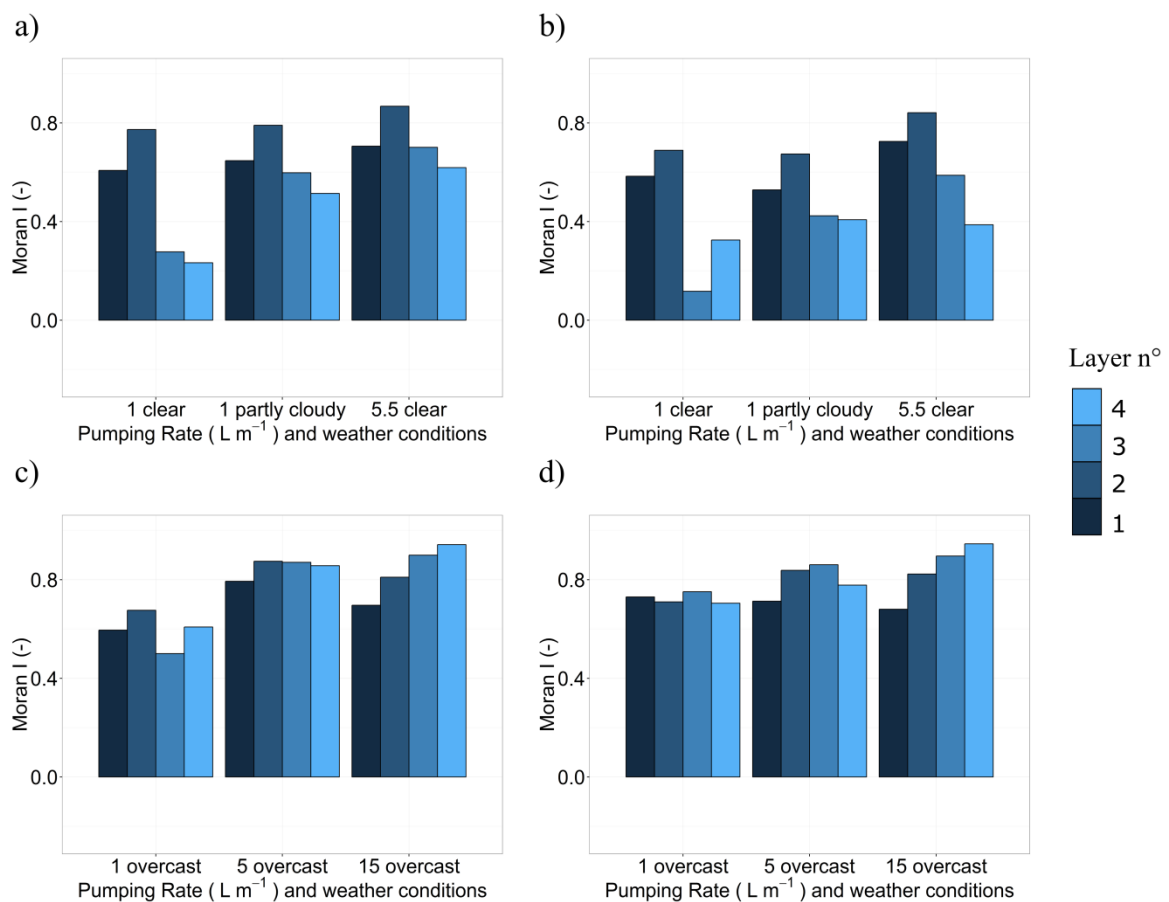


Figure 3.5 Moran's I values. (a) Day, clear and partly cloudy sky; (b) night, clear and partly cloudy sky; (c) day, overcast sky; and (d) night, overcast sky. All plots are plotted from lowest to highest injection rates.

Moran's I values for Layers 1 and 2 (closest to the warm water injection) were high under all weather conditions. This indicates a higher influence of warm water inflow on temperature patterns observed in Layers 1 and 2 than in Layers 3 and 4.

Under clear sky weather conditions, Moran's I values for Layers 1 and 2 are similar or decrease slightly during night measurements. For Layers 3 and 4, Moran's I values during night are lower than Moran's I values during day measurements.

Under overcast weather conditions, Moran's I values within Layers 1, 2, 3, and 4 for 1 L min⁻¹ injection rate increase during night measurements. For an injection rate of 5 L min⁻¹, Moran's I values for Layers 1 and 4 are lower during night than during day measurements. Finally, Moran's I values for 15 L min⁻¹ injection rate are very similar during day and night measurements.

In summary, significant spatial autocorrelations within each layer have been identified in all datasets. However, calculated Moran's I values vary depending on the injection rate of warm water, weather conditions, and the diurnal cycle (see Figure 3.5). This indicates that the strength of the spatial pattern within each layer also varies depending on the injection rates applied, the weather conditions, and the diurnal cycle.

Vertical spatial temperature patterns: Spatial correlation between layers

Spatial correlation between neighboring layers

At high injection rates, the largest correlations between neighbouring layers occurred (Table S1). At lower injection rates, the correlation was usually much smaller and the largest correlation generally occurred between neighbouring layers. There are three exceptions where the largest correlations occurred between nonneighbouring layers: dataset 1 L min⁻¹, clear, daytime and 1 L min⁻¹, partly cloudy, day and night-time. The reason might be that the extent of the spatial warm water pattern in Layers 1 and 3 is more similar than the observed pattern in Layer 2 (See Figures 3.4c and S1).

Measurements under clear sky conditions with an injection rate of 1 L min⁻¹ showed a downward trend (from Layer 1 to 4) on spatial correlation coefficients calculated between neighbouring layers (1&2, 2&3, 3&4). When weather conditions were “partly cloudy” for 1 L min⁻¹, spatial correlation coefficients calculated between neighbouring layers showed an upward trend from Layer 1 to 3 (1&2 and 2&3) and the lowest value between the two uppermost layers (3&4). Finally, when weather conditions were overcast and injecting 1 L min⁻¹, it is possible to see that there was an upward trend (from Layer 1 to 4) on spatial correlation coefficients calculated between neighbouring layers (1&2, 2&3, 3&4), for example, from 0.415 to 0.815 during day.

The same upward trend was observed for an injection rate of 5.5 L min^{-1} with clear sky conditions for spatial correlation coefficients calculated between neighbouring layers: from 0.516 to 0.685. At injection rate of 5 L min^{-1} with overcast conditions, spatial correlation coefficients between neighbouring layers keep increasing, for example, from 0.795 to 0.933 day.

On the contrary, when injecting 15 L min^{-1} , calculated spatial correlation coefficients between neighbouring layers only increase for layers 1&2 and 2&3 from 0.846 to 0.888. Spatial correlation coefficients for 3&4 layers decrease to 0.450.

Spatial correlation between nonneighbouring layers

Highest spatial correlations calculated between nonneighbouring layers (1&3, 1&4, and 2&4) were found for 1 L min^{-1} under overcast conditions during night (0.681, 0.572, and 0.663, respectively) and for 5 L min^{-1} under overcast conditions during day (0.608, 0.546, and 0.791, respectively).

Spatial correlation coefficients between Layers 1&3 generally increase from 1 to 15 L min^{-1} under overcast conditions. Spatial correlation coefficients between layers 1&4 and 2&4 generally increase from 1 to 5 L min^{-1} and considerably decrease at 15 L min^{-1} . These observations agree with the change on the spatial pattern observed in Figure 3.3f, compared with the spatial patterns observed in Figures 3.3d and 3.3e. In Figure 3.3f, injected warm water flows straight up across Layers 1, 2, and 3. In Layer 4, injected warm water spreads all over the water surface. Low spatial correlation coefficients for 15 L min^{-1} between Layers 2&4 and 1&4 indicate differences of spatial patterns observed between Layers 1&4 and 2&4 in Figure 3.3f.

Figure 3.6 presents calculated spatial correlation coefficients for different (clear sky, partly cloudy, and overcast) conditions for both day and night measurements independently.

Spatial correlation coefficients calculated between 1&2, 1&3, and 2&3 are higher during night than during day. However, spatial correlation coefficients calculated for 1&4, 2&4, and 3&4 showed different results. For clear sky conditions, calculated spatial correlation coefficients during night time are lower than calculated spatial correlation coefficients for the same injection rates during day. In contrast, calculated spatial correlation coefficients for overcast weather conditions are slightly higher during night than during day within the same injection rates, for both 1 and 15 L min^{-1} . In contrast, for 5 L min^{-1} under overcast conditions, spatial correlation coefficients are slightly lower during night than during day.

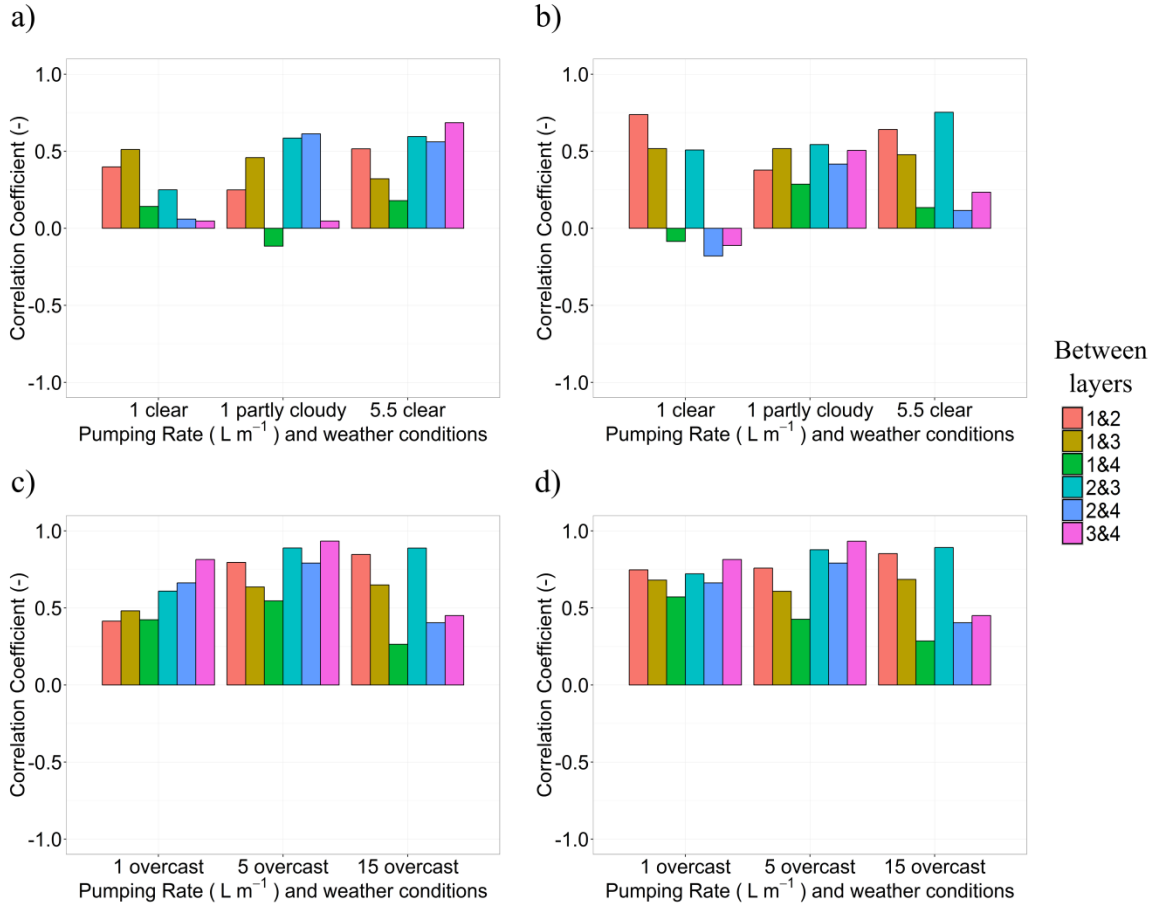


Figure 3.6 Spatial correlation coefficients for (a) day, clear sky and partly cloudy conditions; (b) night and clear sky, partly cloudy conditions; (c) day and overcast conditions; (d) night and overcast conditions.

Three main findings can be listed from the calculation of spatial correlation coefficients between layers:

- In general, overcast weather conditions result in higher spatial correlation coefficients between neighbouring layers and nonneighbouring layers.
- At 15 L min⁻¹, the uppermost layer (Layer 4) is spatially less correlated with the underlying layers than at 1 and 5 L min⁻¹ under overcast conditions. These observations agree with the change on the spatial pattern observed in Figure 3.3f in comparison with the spatial patterns observed in Figure 3.3d,e.
- The diurnal cycle has an effect on spatial correlation coefficients calculated between layers. Layers within the water column show higher spatial correlation coefficients between them during night than during day for the same injection rates no matter of the weather conditions. However, for the uppermost layer (Layer 4) at the water

surface–atmosphere interface, spatial correlation coefficients are lower for clear nights and generally similar or slightly higher for overcast nights.

3.3.3 Net heat fluxes across the water surface, advective heat fluxes and internal energy change

The effects of different weather conditions, different injection rates, and the diurnal cycle on the energy balance of the water column were quantified. This was done by quantifying the net heat fluxes across the water surface (G in W m^{-2}) as well as the energy change due to advective transport by the water inlet from the lake, the warm water inlet at the bottom of the mesocosm and the water outlet from the mesocosm (E_{adv} in MJ). Their sum results in the change of internal energy in the mesocosm (ΔE in MJ).

Net heat fluxes across the water surface (G)

Net heat fluxes across the water surface (G) during day and night are composed of net radiation (R_n), latent heat fluxes (phase transformation, λE), and sensible heat fluxes (H) with R_n being the most important of the three (see Figure 3.7a,c,e,g,i,k,m). This indicates that the system gains and loses energy mainly by R_n .

Net radiation (R_n) is composed of net shortwave radiation (R_{ns}) and net longwave radiation (R_{nl}). The net shortwave radiation (R_{ns}) is considered a heating term (during daytime) and the net longwave radiation (R_{nl}) is considered a cooling term (during day and night; Betts, 2015). Therefore, during daytime, calculated R_n values are higher than during night for both clear and overcast weather conditions (Figure 3.7a, c,e,g,i,k,m). This is because during daytime, the surface cooling due to R_{nl} is partly compensated by R_{ns} (Betts, 2003, 2015; Betts, Desjardins, & Worth, 2013). In addition, during night, there is no shortwave radiation coming from the sun and the cooling term, R_{nl} , will be the main component of the R_n .

In general, R_n values during daytime are lower under overcast weather conditions than under clear sky conditions (Figure 3.7a,c,e,g,i, k,m). During night, R_n values are less negative under overcast conditions than under clear sky conditions (Figure 3.7a,c,e,g,i,k,m). These results are related to the important effect that clouds have on the net radiation balance (R_n ; Betts, 2015). On the one hand, during daytime, incident downward shortwave radiation at the water surface is lower under overcast weather conditions than under clear sky conditions. On the other hand, during day and night, surface cooling to space due to R_{nl} is lower under overcast weather conditions than under clear sky conditions (Betts, 2003, 2015; Betts et al., 2013). The smallest net heat fluxes across the water surface (G) occur under overcast conditions (see Figure 3.7a,g,k,m).

Energy transferred across the interface (E_G) and advected energy by inflows and outflows (E_{adv})

For all datasets, during daytime measurements, the system gains energy mainly by E_G and during night time measurements by E_{adv} (Figure 3.7b,d,f, h,j,l). Only, for 15 L min⁻¹ overcast weather conditions dataset, the system mainly gains energy by E_{adv} during day and night due to the high amounts of injected warm water (Figure 3.7n). This means that the energy gains in the mesocosm during day are dominated by the net heat fluxes across the water surface (G) and the energy losses in the mesocosm are dominated by the energy transported by advection into and out of the mesocosm. On the contrary, the energy gains in the mesocosm during night are dominated by the imported energy of the injected warm water (E_{adv}) and the energy losses in the mesocosm are dominated by the net heat fluxes across the water surface (G).

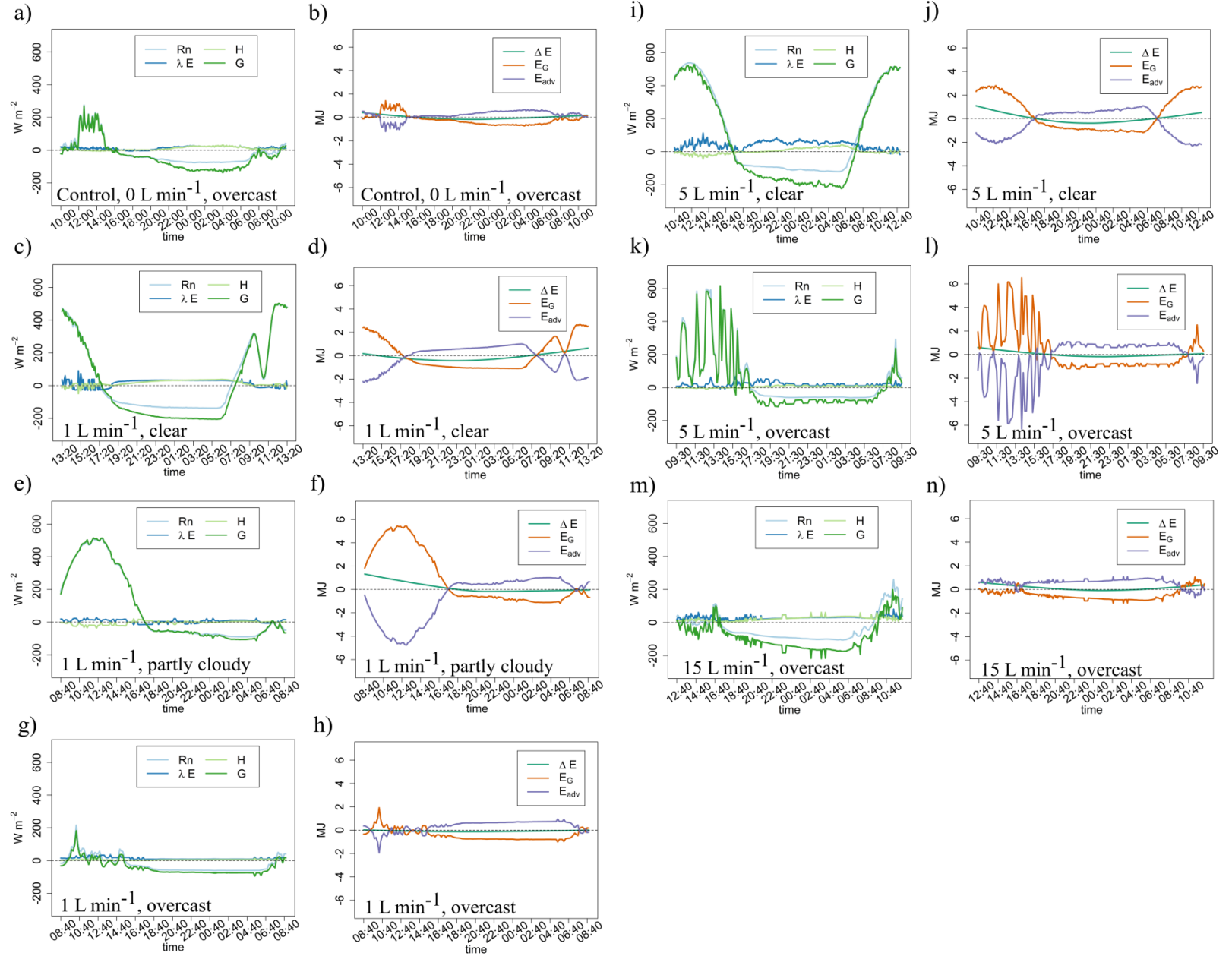
Internal energy changes in the mesocosm (ΔE)

ΔE changes over time are clearly affected by the diurnal cycle (see Figure 3.8). ΔE decreases during the day; it reaches a minimum during night and increases again in the early morning. However, the intensity of changes of ΔE over time varies depending on weather conditions and injection rate.

ΔE changes over time are lowest under overcast weather conditions for all different injection rates. The dataset with an injection rate of 1 L min⁻¹ shows the lowest ΔE changes over time, and 15 L min⁻¹ shows the highest ΔE changes over time.

High changes on ΔE over time are observed when injecting 1 L min⁻¹ under clear sky conditions. For partly cloudy conditions, keeping the same injection rate, the maximum loss of energy over time is smaller than under clear sky weather conditions. However, the slope of ΔE in Figure 3.8 for 1 L min⁻¹ partly cloudy is higher than that of the 1 L min⁻¹ clear sky during day; this indicates that the rate of energy loss is greater. On increasing the injection rate to 5.5 L min⁻¹ under clear sky, maximum energy loss in the system is almost similar to the maximum energy loss when injecting 1 L min⁻¹ under clear sky. However, change of ΔE over time is greater when injecting 5.5 L min⁻¹ under clear sky than when injecting 1 L min⁻¹ under clear sky.

Figure 3.7 Calculated heat fluxes across the water surface (G), net radiation (R_n), evaporative heat flux (λE), and sensible heat flux (H) for (a) control dataset with 0 L min^{-1} injection rate, overcast, (c) 1 L min^{-1} injection rate, clear, (e) 1 L min^{-1} partly cloudy, (g) 1 L min^{-1} overcast, (i) 5.5 L min^{-1} clear, (k) 5 L min^{-1} overcast, and (m) 15 L min^{-1} overcast and calculated ΔE , E_G and E_{adv} for (b) control experiment overcast (d) 1 L min^{-1} clear, (f) 1 L min^{-1} partly cloudy, (h) 1 L min^{-1} overcast, (j) 5.5 L min^{-1} clear, (l) 5 L min^{-1} overcast, and (n) 15 L min^{-1} overcast.



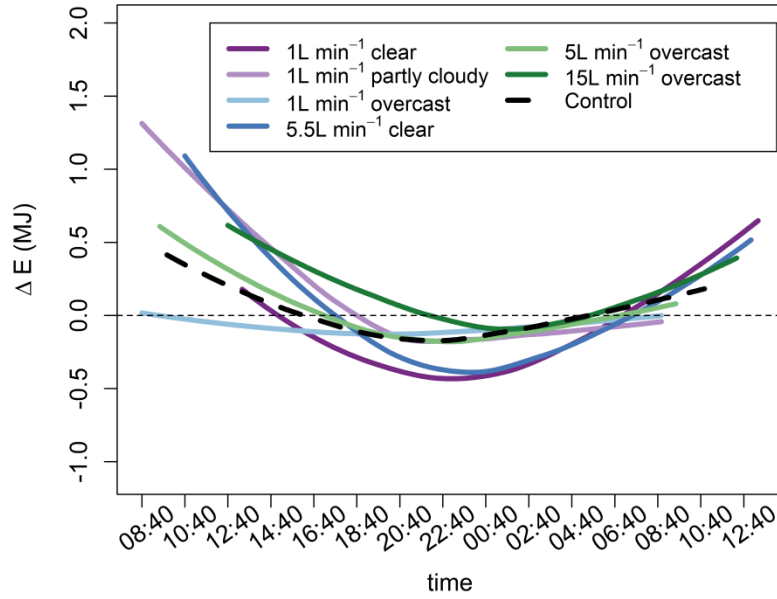


Figure 3.8 Change of energy (ΔE) over time for seven datasets: 1 L min⁻¹ clear, 1 L min⁻¹ partly cloudy, 1 L min⁻¹ overcast, 5.5 L min⁻¹ clear, 5 L min⁻¹ overcast, 15 L min⁻¹ overcast, and control dataset with 0 L min⁻¹ injection rate, overcast conditions.

Coupling internal energy changes over time (ΔE), net heat fluxes across the water surface (G) and energy in the mesocosm (E_G and E_{adv})

Under overcast conditions, energy changes (ΔE) in the mesocosm are lower and slower than energy changes (ΔE) in the mesocosm under clear sky conditions. This can be related to the calculated small net heat fluxes across the water surface (G) under overcast conditions. Or in other words, energy at the water surface is lost at smaller quantities and at slower rates under overcast conditions than under clear sky. As the amount of injected warm water increases, the amount of advected energy (E_{adv}) in the mesocosm increases. Under clear sky, net heat fluxes across the water surface (G) are bigger than under overcast weather conditions. Higher injection rates of warm water under clear sky will result in higher and faster energy changes (ΔE) over time in the mesocosm due to bigger net heat fluxes across the water surface (G). On the contrary, under overcast conditions, higher injection rates of warm water will contribute to decrease and to slow down the energy changes (ΔE) over time in the mesocosm, due to small net heat fluxes across the water surface (G).

Finally, during daytime, because R_n is the main component of the net heat fluxes across the water surface (G), the mesocosm energy gains are due to R_n (R_{ns} and R_{nl}). This agrees with

E_G being the main driver of gains of energy in the mesocosm during daytime. If the mesocosm is subject to strong gains of energy due to R_n during day (for instance under clear sky), it means that energy gains by R_{ns} will prevail over energy losses by R_{nl} . During night, the main losses of energy in the mesocosm are driven by R_n (only R_{nl}). This agrees with E_G being the main driver of losses of energy in the mesocosm during night.

Observed spatial patterns of injected warm water in the mesocosm, net heat fluxes across the water surface (G) and energy changes over time (ΔE)

Spatial patterns of injected warm water across the water column and at the water surface observed in Figure 3.3d–f can be related to small and slow energy changes (ΔE) over time, due to small net heat fluxes across the water surface (G) under overcast weather conditions during day and night. During daytime, the heat signal of the injected warm water will prevail across the water column and at the water surface due to: 1) less absorbed shortwave radiation at the water surface of the mesocosm (R_{ns}) and 2) less water surface cooling in the mesocosm due to R_{nl} . During night-time, the heat signal of the injected warm water will prevail across the water column and at the water surface due to: 1) less water surface cooling in the mesocosm due to R_{nl} and 2) energy gains in the mesocosm due to injected warm water.

Finally, spatial patterns of injected warm water, across the water column and at the water surface, observed in Figure 3.3a–c can be related to high and fast energy changes (ΔE) over time in the mesocosm, due to stronger net heat fluxes across the water surface (G) under clear sky during day and night, than under overcast conditions. In general, during daytime, the heat signal of the injected warm water is not detectable at the water surface, mainly due to high amount of absorbed shortwave radiation at the water surface (R_{ns}) during clear sky and to a less extent, due to water surface cooling in the mesocosm by R_{nl} . During night, the heat signal of the injected warm water is not detectable at the water surface due to strong cooling of the water surface in the mesocosm by R_{nl} .

3.4 Discussion

Detectability of upwelling signals

One basic question of the present study is if and under which circumstances the lake-internal upwelling pattern due to simulated GW discharge can be detected in the water column and at the water surface. For that purpose, temperature signals due to the positive buoyancy of relatively warm water need to be separated from other temperature fluctuations. In the context of the present study, strong spatial autocorrelations within layers and strong spatial

correlations between layers are interpreted as “real” temperature signal related to the positive buoyancy of relatively warm water, instead of to other temperature fluctuations. Moran's I and LISA maps (indicators for horizontal spatial patterns within layers) confirmed the spatial patterns visually observed in Figure 3.3. The strength of spatial autocorrelation within layers (horizontal spatial patterns) increased under overcast conditions, at higher injection rates and during night-time. Calculated spatial correlation coefficients between layers (vertical spatial patterns) also increased under overcast weather conditions, higher injection rates, and during night-time measurements. At 15 L min^{-1} injection rate, spatial correlation coefficients between Layer 4 (the uppermost layer) and the other layers decreased due to a change of the general shape of the upwelling flume (Figure 3.3f and Figure 3.9, a.6 and b.6). Due to the intense injection rate, the warm water signal travels straight upwards, and once it reaches the water surface, it spreads horizontally at the water surface.

Relevance of diurnal cycle and cloud cover on signal detectability

Under overcast conditions, calculated slow energy changes (ΔE) over time and low net heat fluxes across the water surface (G) seem to be related to the spatial patterns in Figure 3.3d–f and the results obtained with the Moran's I coefficient, LISA maps, and the spatial correlation coefficients. Slow changes of energy (ΔE) over time and low net heat fluxes across the water surface (G) indicate that the mesocosm is able to sustain internal energy for longer time periods than under clear sky conditions. This means that the heat signal related to warm water injection is not lost. On the contrary, in datasets under clear and partly cloudy conditions, higher energy changes (ΔE) over time and higher net heat fluxes across the water surface (G) were calculated. In other words, the mesocosm loses internal energy faster over time, and consequently, the heat signal related to warm water injection is lost faster over time under clear sky conditions.

The amount of energy in a water body (for instance, a lake) is controlled by the inflows and outflows of water into and out of the water body and by heat fluxes across the water surface, among others (Henderson-Sellers, 1986). The net heat fluxes across the water surface (G) are composed of net shortwave radiation (R_{ns}), net longwave radiation (R_{nl}) and nonradiative fluxes (sensible heat [H] and latent heat [λE]; Henderson-Sellers, 1986; McAlister & McLeish, 1969). The main component for calculated net heat fluxes across the water surface (G) is the net radiation (R_n), which is the sum of net shortwave radiation (R_{ns}) and net longwave radiation (R_{nl}). The net radiation balance is driven by the diurnal cycle of the incident shortwave radiation (Betts, 2015). This means that the solar warming during daytime

and the longwave cooling during night-time drive the diurnal cycles of air temperature and water surface temperature (Betts, 2015; Vercauteren et al., 2011) and, thus, impact on the detectability of the injected warm water temperature signal in the mesocosm. Furthermore, cloud cover is also a relevant regulator of the diurnal cycle of the net radiation balance (R_n ; Betts, 2003, 2015; Betts et al., 2013; Dai & Trenberth, 1999). Clouds decrease the incident shortwave radiation at the water surface and decrease the net surface cooling at the water surface because there is less R_{nl} . Therefore, the detectability of the injected warm water temperature signal in the mesocosm is decisively controlled by the diurnal cycle of the net radiation balance (R_n) and the cloud cover. In order to illustrate the relevance of the diurnal cycle (day vs. night) of the net radiation balance ($R_n = R_{ns} + R_{nl}$) and cloud cover on the observed spatial patterns of the heat signal related to warm water injection and based on the results presented in this paper, a conceptual model for the spatial patterns observed under different weather conditions (clear, partly cloudy, and overcast), injection rates, and diurnal cycles (day vs. night) is suggested in Figure 3.9. It illustrates the relevance of the net heat fluxes across the water surface (G) by the strength of net short wave (R_{ns}) and net long wave (R_{nl}) radiation (conceptualized by size of arrow: big: high values, small: low values) for different injection rates, different weather conditions (clear, partly cloudy, and overcast), and diurnal cycles (day vs. night). During day, the main gains or losses of heat at the mesocosm's water surface are due to the $R_n (=R_{ns} + R_{nl})$. During clear sky conditions during daytime, due to the higher solar warming (R_{ns}) at the water surface than during overcast weather conditions, the water surface is heated up. In consequence, the heat signal of the injected warm water at the water surface is mixed with the heated water surface due to solar warming. On the contrary, during overcast weather conditions during daytime, calculated R_n (see Figure 3.7) and solar warming due to R_{ns} are lower. In consequence, the heat signal of the injected warm water can be detected at the water surface (see Figure 3.9a). During night, because there is no R_{ns} , the main gains or losses of heat at the mesocosm's water surface are due to R_{nl} . Both, during night and day, the degree of heat losses from the water surface depends on the presence of clouds at the sky (see Figure 3.9b). During clear sky conditions, the strength of R_{nl} is higher than under overcast weather conditions. In consequence, during clear sky conditions at night, the mesocosm loses higher amounts of energy across the water surface–atmosphere interface than during overcast conditions. The heat signal of the injected warm water at the water surface is lost faster during clear sky conditions than during overcast conditions at night (Figure 3.9b).

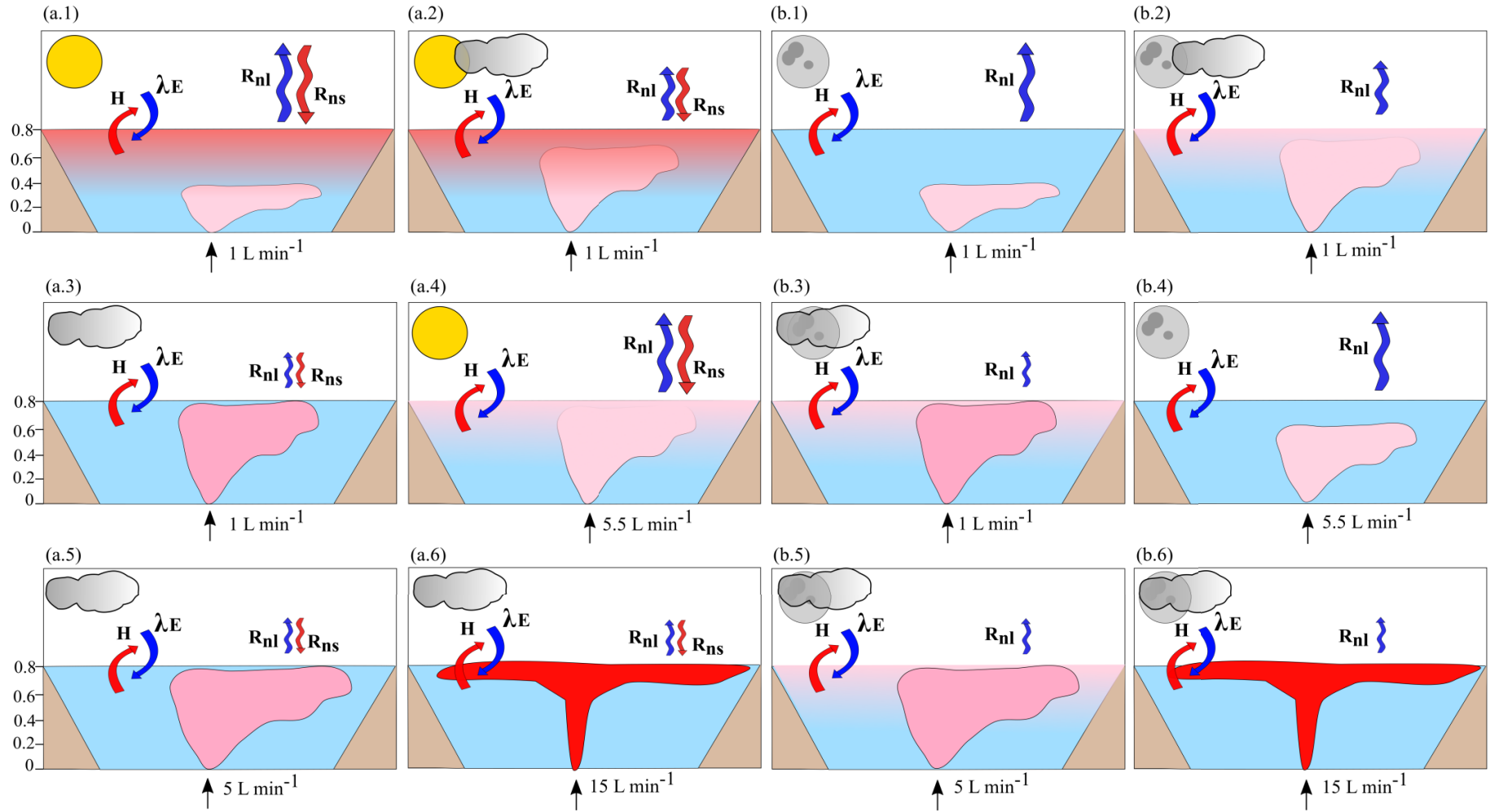


Figure 3.9 Conceptual model of spatial distribution of injected water in the water column under different weather conditions, for different injection rates during (a) day and (b) night. (a.1) and (b.1) 1 L min^{-1} , clear sky; (a.2) and (b.2) 1 L min^{-1} , partly cloudy sky; (a.3) and (b.3) 1 L min^{-1} , overcast sky; (a.4) and (b.4) clear sky, 5.5 L min^{-1} ; (a.5) and (b.5) 5 L min^{-1} , overcast sky; (a.6) and (b.6) 15 L min^{-1} , overcast sky. The degree of the signal strength is indicated by the intensity of the red colour: Light red: weak signal, dark red: strong signal. The size of the arrows indicates the strength of the R_{nl} and R_{ns} . The blue colour indicates the losses of energy from the mesocosm. The red colour indicates the gains of energy in the mesocosm.

Application of FO-DTS for detection of LGD upwelling

FO-DTS has been used to detect GW discharge at the sediment–water interface in lakes (Blume et al., 2013; Liu et al., 2015; Tristram et al., 2015) and streams (Hare et al., 2015; Krause et al., 2012; Lowry et al., 2007). However, it had not yet been determined how the temperature signal propagates from the sediment–water interface through the water column up to the water surface–atmosphere interface and how the signal is affected by environmental parameters such as weather conditions (clear vs. overcast) and the diurnal cycle of net radiation. In Hare et al. (2015), FO-DTS measurements were compared with thermal infrared (TIR) measurements, which allowed the comparison of heat signals detected at the stream bed and at the water surface. Winter conditions were proven to be the best season to conduct these kinds of measurements. However, the characterization of weather and diurnal conditions that might have affected the upwelling patterns of the GW heat signal across the water column was not addressed until the present study. For instance, Liu et al. (2015) conducted an experiment on the lake bed that took into account environmental factors to determine the best time to detect GW discharge areas with FO-DTS. Liu et al. (2015) worked in a lake that was relatively shallow, which reduced the effect of vertical stratification on the lakebed temperatures during the FO-DTS measurements. Nevertheless, the FO-DTS experiment conducted did not include multilevel temperature measurements or a detailed characterization of the influence of weather conditions and the diurnal cycle of net radiation on the detection of GW discharge across the water column.

The knowledge gap on upwelling GW heat signals monitored with FO-DTS across the water column may have led to misinterpretations. This is because the temperature within the water column may be affected by several external parameters. Therefore, timing and conditions when measuring warm upwelling fluxes with FO-DTS are of great relevance for the interpretation of the results. For instance, it is crucial to be aware of the vertical positioning of the cable because variations of the vertical positioning of the cable on the sediment or within the water column may lead to misinterpretations of the patterns observed. Variable external conditions have to be taken into account for correct interpretation that might present a real difficulty for any quantitative assessment. Therefore, it is essential to determine those parameters that may influence the temperature such as solar radiation and to make sure that the temperature variations of the lake as detected by the FO-DTS are mainly caused by GW discharge (Liu et al., 2015) as presented in this paper.

Possible system interferences and uncertainties of the study

Effect of wind and possible consequences

Wind is an important factor affecting lake SW temperatures and lake internal mixing (Pöschke et al., 2015). Wind promotes movement and mixing of SW bodies. The SW can be dragged by the wind from one shore of a lake to the other shore inducing downwelling of water in the water body on one side of the lake and at the same time water movement from the bottom of the lake upwards to the lake surface (mixing). This process, relevant in lake settings, is probably irrelevant in the small experimental mesocosm used in the present study. From the slice3D plots in Figure 3.3, there is no indication for a wind-induced circulation or mixing. Wind speeds during the experiments were generally low (ranging from 0.0045 to 2.1789 m s⁻¹). Steep bank slopes reaching a height of 1 m above the water surface prohibited wind impacts on the water surface. Furthermore, due to the small size of the mesocosm, the wind fetch is short and a potential wind impact on the water surface is irrelevant. However, when transferring the results of the mesocosm experiment to a real lake setting, possible wind impacts should be taken into account.

Thickness of water column in the present study

In the present study, the thickness of the water column is 0.82 m. The obtained conclusions could be directly transferred to shallow lakes not deeper than 1 m, shore areas of lakes not deeper than 1 m, and probably to shallow lakes with slightly larger depth. Because there is no thermal stratification within the water column of the mesocosm, the obtained results of the present study can only be transferred to cases where there is no thermal stratification.

Possible effects of electrical conductivity of groundwater

The upwelling of the water injected at the mesocosm's bottom is driven by density differences of the injected water and the water in the mesocosm. The density differences are caused by different temperatures and different ion compositions of the two waters. The water in the mesocosm is a mixture of lake water and water previously injected at the mesocosm's bottom. Due to differing injection rates during the different experiments, there is no constant relationship between the relatively large inflow from the lake (33 L min⁻¹) and the relatively small inflow from the injection at the mesocosm's bottom (0 to 15 L min⁻¹). For simplicity, we assume that the mesocosm water composition is basically identical to the lake water composition. On the basis of measurements of the ion composition of both water bodies, we

ended up with total dissolved solid concentrations of 489 mg L^{-1} for the lake and 429 mg L^{-1} for the injected water, that is, there is a density difference of 60 mg L^{-1} between the two waters. Based on a mean mesocosm temperature of 4.7°C , the density of the water in the mesocosm is $0.999946 \text{ kg L}^{-1}$, and based on a mean temperature of 15°C of the injected water, the density is $0.999114 \text{ kg L}^{-1}$, that is, there is a density difference of 832 mg L^{-1} between the two waters. Basically, the density difference due to the different ion composition of the two different waters, strengthen the temperature induced density difference. The combined effect of ion composition and temperature on the density difference between the two waters is 880 mg L^{-1} (calculation according to Dietz, Lessmann, & Boehrer, 2012) or 921 mg L^{-1} (calculation according to Boehrer & Herzsprung, 2010).

Therefore, the injected warm water should immediately rise upwards through the surrounding denser lake water via buoyancy. During the short ascent, some mixing might have occurred and the contact with surrounding water resulted in some cooling of the injected warm water. Nevertheless, only in experiments during overcast conditions (Figure 3.3d–f), the injected warm water was still warmer than the rest of the water in the mesocosm when it reached the water surface and thus, floated on the top of the water body. From there, the warmer less dense water gradually spread as a plume on the water surface.

Low wind speeds, shallow water conditions, and density differences between simulated GW and SW might favour the upwelling of simulated GW discharge on the SW. However, in the present study, the main parameters controlling the detection of simulated GW on the water surface seem to be the net radiation balance (R_n) and the cloud cover during day and night-time measurements. Because the experiments have been carried out under specific conditions, the previous statements are only true in lake areas where the same conditions apply as in the mesocosm experiment during winter conditions.

This study is a first attempt to simulate thermal patterns of discrete LGD in shallow lakes or close to lake shores. The mesocosm experiment and simulation of GW discharge is the first step in order to identify the main controlling parameters that favour detection of hotspots of LGD on the lake surface (mesocosm surface in this case). We have decreased the amount of variables that impact LGD by simulating discrete GW discharge in a mesocosm. The mesocosm where the simulation has been performed intends to represent a small shallow area of a lake where GW exfiltration by LGD occurs. Thus, not all the influencing factors such as wind, waves, and vegetation that could be present under natural conditions have been considered. However, GW discharge that is warmer than SW has been little studied relative to

discharge of cold GW to warmer SW. Thus, by conducting studies during colder times of the year, scientist can make use of the conclusions presented here.

3.5 Conclusion

The present study demonstrates that during winter conditions, the positive buoyancy of relatively warm water imported by simulated LGD into shallow water bodies (mesocosm used as model system) allows detection of LGD at the lake's water surface–atmosphere interface by FO-DTS. FO-DTS technology offers fine scale measurements with high temporal resolution and allows the observation of induced lake-internal upwelling caused by simulated LGD in a three-dimensional perspective. In this manner, different lake internal upwelling patterns have been described from the sediment–water interface through the water column to the water surface–atmosphere interface caused by the injection of warm water at different rates, different weather conditions, and during the diurnal cycle. Simulated GW signals at the water surface were identified at all applied injection rates, from lowest 1 L min^{-1} to highest 15 L min^{-1} . However, detection of simulated LGD at the water surface–atmosphere interface was mainly determined by the diurnal cycle of the net radiation balance (R_n) and the cloud cover. Based on the results presented in this paper, overcast weather conditions and night-time measurements are recommended for tracing discrete warm water upwelling fluxes across the water column and at the water surface.

Acknowledgments

Funding: This work was supported by the European Union's Seventh Framework programme for research, technological development and demonstration [grant number 60715]: Ecohydrological Interfaces as Critical Hotspots for Transformations of Ecosystem Exchange Fluxes (INTERFACES).

Special thanks to Franziska Pöschke, Karin Meinikmann, Hauke Dämpfling and Anne Mehrtens.

Supporting information

Appendix S1: Quantification of interfacialne heat transfer and net-advective heat flux

Appendix S2: Nomenclature

Figure S1: Comparison of LISA maps and spatial correlation coefficients between layer 1 and 2 and layer 1 and 3 for datasets: a) 1 L min^{-1} clear conditions, daytime, b) 1 L min^{-1} partly

cloudy conditions, daytime and c) 1 L min^{-1} partly cloudy conditions, night-time. From top row to bottom row: layer 4, layer 3, layer 2 and layer 1.

Table S1. Spatial correlation coefficients between layers.

References

- Anselin L. 1995. Local Indicators of Spatial Association-LISA. *Geographical Analysis* **27** (2): 93–115 DOI: 10.1111/j.1538-4632.1995.tb00338.x
- Anselin L. 1996. The Moran scatterplot as an ESDA tool to assess local instability in spatial association. In *Spatial Analytical Perspectives on GIS* 111–125.
- Apperl B, Pressl A, Schulz K. 2017. Feasibility of Locating Leakages in Sewage Pressure Pipes Using the Distributed Temperature Sensing Technology. *Water, Air, and Soil Pollution* **228** (2) DOI: 10.1007/s11270-017-3250-7
- Baker BH, Martinovic-Weigelt D, Ferrey M, Barber LB, Writer JH, Rosenberry DO, Kiesling RL, Lundy JR, Schoenfuss HL. 2014. Identifying non-point sources of endocrine active compounds and their biological impacts in freshwater lakes. *Archives of environmental contamination and toxicology* **67** (3): 374–388 DOI: 10.1007/s00244-014-0052-4
- Betts AK. 2003. The diurnal cycle over land. In *Forests at the Land-Atmosphere Interface*, Mencuccini M, , Grace J, , Moncrieff J, , McNaughton K (eds).CABI Publishing, Wallingford, Oxon OX10 8DE, UK; 73–93.
- Betts AK. 2015. Diurnal Cycle. In *Encyclopedia of Atmospheric Sciences*, Pyle J, , Fuqing Z (eds).Texas A&M University, College Station, TX, USA; 319–323. DOI: 10.1016/B978-0-12-382225-3.00135-3
- Betts AK, Desjardins R, Worth D. 2013. Cloud radiative forcing of the diurnal cycle climate of the Canadian Prairies. *Journal of Geophysical Research* **118** (June): 8935–8953 DOI: 10.1002/jgrd.50593
- Bivand RS, Pebesma E, Gómez-Rubio V. 2013. *Applied Spatial Data Analysis with R*. Springer-Verlag New York. DOI: 10.1007/978-1-4614-7618-4
- Blume T, Krause S, Meinikmann K, Lewandowski J. 2013. Upscaling lacustrine groundwater discharge rates by fiber-optic distributed temperature sensing. *Water Resources Research* **49** (October 2012): 7929–7944 DOI: 10.1002/2012WR013215
- Boehrer B, Herzprung P. 2010. Calculating density of water in geochemical lake stratification models. *Limnology and oceanography, methods* (1): 567–574 DOI: 10.4319/lom.2010.8.567
- Brabrand Å, Koestler AG, Borgstrøm R. 2002. Lake spawning of brown trout related to groundwater influx. *Journal of Fish Biology* **60** (3): 751–763 DOI: 10.1006/jfbi.2002.1901

- Brunke M, Gonser T. 1997. The ecological significance of exchange processes between rivers and groundwater. *Freshwater Biology* **37**: 1–33 DOI: 10.1046/j.1365-2427.1997.00143.x
- Cardenas MB, Lagmay AMF, Andrews BJ, Rodolfo RS, Cabria HB, Zamora PB, Lapus MR. 2012. Terrestrial smokers: Thermal springs due to hydrothermal convection of groundwater connected to surface water. *Geophysical Research Letters* **39** (2): 1–6 DOI: 10.1029/2011GL050475
- Curry RA, Noakes DLG. 1995. Groundwater and the selection of spawning sites by brook trout (*Salvelinus fontinalis*). *Canadian Journal of Fisheries and Aquatic Sciences* **52** (8) DOI: 10.1139/f95-765
- Dai A, Trenberth KE. 1999. Effects of Clouds , Soil Moisture , Precipitation , and Water Vapor on Diurnal Temperature Range. *Journal of Climate* **12**: 2451–2473
- Dietz S, Lessmann D, Boehrer B. 2012. Contribution of Solutes to Density Stratification in a Meromictic Lake (Waldsee/Germany). *Mine Water and the Environment* **31** (2): 129–137 DOI: 10.1007/s10230-012-0179-3
- Environmental Systems Research Institute (ESRI). 2014. ArcGIS Desktop Help 10.3: How Band Collection Statistics works Available at: <http://desktop.arcgis.com/en/arcmap/10.3/tools/spatial-analyst-toolbox/how-band-collection-statistics-works.htm#GUID-FE2BAE08-24DB-4A50-8F88-86D856F89190> [Accessed 15 March 2016]
- Hare DK, Briggs MA, Rosenberry DO, Boutt DF, Lane JW. 2015. A comparison of thermal infrared to fiber-optic distributed temperature sensing for evaluation of groundwater discharge to surface water. *Journal of Hydrology* **530**: 153–166 DOI: 10.1016/j.jhydrol.2015.09.059
- Haselwimmer C, Prakash A, Holdmann G. 2013. Quantifying the heat flux and outflow rate of hot springs using airborne thermal imagery: Case study from Pilgrim Hot Springs, Alaska. *Remote Sensing of Environment* **136**: 37–46 DOI: 10.1016/j.rse.2013.04.008
- Hausner MB, Suárez F, Glander KE, van de Giesen N, Selker JS, Tyler SW. 2011. Calibrating single-ended fiber-optic Raman spectra distributed temperature sensing data. *Sensors* **11** (11): 10859–79 DOI: 10.3390/s111110859
- Hayashi M, Rosenberry D. 2002. Effects of Ground Water Exchange on the Hydrology and Ecology of Surface Water. *Ground Water* **40** (3): 309–316
- Henderson-Sellers B. 1986. Calculating the surface energy balance for lake and reservoir modeling: A review. *Reviews of Geophysics* **24** (3): 625 DOI: 10.1029/RG024i003p00625

- Hung Y-T, Eldridge J, Taricska JR, Li KH. 2005. Advanced Air and Noise Pollution Control., Wang LK, , Pereira NC, , Hung Y-T (eds). Humana Press: Totowa, NJ; 359–384. DOI: 10.1007/978-1-59259-779-6_10
- Kidmose J, Engesgaard P, Nilsson B, Laier T, Looms MC. 2011. Spatial Distribution of Seepage at a Flow-Through Lake: Lake Hampen, Western Denmark. *Vadose Zone Journal* **10** (1): 110 DOI: 10.2136/vzj2010.0017
- Krause S, Blume T, Cassidy NJ. 2012. Investigating patterns and controls of groundwater upwelling in a lowland river by combining Fibre-optic Distributed Temperature Sensing with observations of vertical hydraulic gradients. *Hydrology and Earth System Sciences* **16** (6): 1775–1792 DOI: 10.5194/hess-16-1775-2012
- Lewandowski J, Meinikmann K, Ruhtz T, Pöschke F, Kirillin G. 2013. Localization of lacustrine groundwater discharge (LGD) by airborne measurement of thermal infrared radiation. *Remote Sensing of Environment* **138**: 119–125 DOI: 10.1016/j.rse.2013.07.005
- Liu C, Liu J, Wang X, Zheng C. 2015. Analysis of Groundwater-Lake Interaction by Distributed Temperature Sensing in Badain Jaran Desert , Northwest China. *Hydrological Processes* DOI: 10.1002/hyp.10705
- Lowry CS, Walker JF, Hunt RJ, Anderson MP. 2007. Identifying spatial variability of groundwater discharge in a wetland stream using a distributed temperature sensor. *Water Resources Research* **43** (10): n/a-n/a DOI: 10.1029/2007WR006145
- McAlister ED, McLeish W. 1969. Heat Transfer in the Top Millimeter of the Ocean. *Journal of Geophysical Research* **74** (13): 3408–3414 DOI: 10.1029/JC074i013p03408
- Nakayama T, Watanabe M. 2008. Missing role of groundwater in water and nutrient cycles in the shallow eutrophic Lake Kasumigaura, Japan. *Hydrological Processes* **22**: 1150–1172 DOI: 10.1002/hyp.6684
- Norrström AC, Jacks G. 1996. Water pathways and chemistry at the groundwater/surface water interface to Lake Skjervatjern, Norway. *Water Resources Research* **32** (7): 2221–2229 DOI: 10.1029/96WR00802
- Piña-Ochoa E, Alvarez-Cobelas M. 2009. Seasonal nitrogen dynamics in a seepage lake receiving high nitrogen loads. *Marine and Freshwater Research* **60** (5): 435–445 DOI: 10.1071/MF08098
- Pöschke F, Lewandowski J, Engelhardt C, Preuß K, Oczipka M, Ruhtz T, Kirillin G. 2015. Upwelling of deep water during thermal stratification onset—A major mechanism of

- vertical transport in small temperate lakes in spring? *Water Resources Research* **51** (January 2016): 9612–9627 DOI: 10.1002/2015WR017579
- Ridgway MS, Blanchfield PJ. 1998. Brook trout spawning areas in lakes. *Ecology of Freshwater Fish* **7**: 140–145 DOI: 10.1111/j.1600-0633.1998.tb00180.x
- Rosenberry DO, Lewandowski J, Meinikmann K, Nitzmann G. 2015. Groundwater - the disregarded component in lake water and nutrient budgets. Part 1: Effects of groundwater on hydrology. *Hydrological Processes* **29** (13): 2895–2921 DOI: 10.1002/hyp.10403
- Sebok E, Duque C, Kazmierczak J, Engesgaard P, Nilsson B, Karan S, Frandsen M. 2013. High-resolution distributed temperature sensing to detect seasonal groundwater discharge into Lake Væng, Denmark. **49** (July): 5355–5368 DOI: 10.1002/wrcr.20436
- Selker JS, Thévenaz L, Huwald H, Mallet A, Luxemburg W, van de Giesen N, Stejskal M, Zeman J, Westhoff M, Parlange MB. 2006b. Distributed fiber-optic temperature sensing for hydrologic systems. *Water Resources Research* **42** (12): n/a-n/a DOI: 10.1029/2006WR005326
- Selker JS, Tyler S, Van de Giesen N. 2014. Comment on ‘capabilities and limitations of tracing spatial temperature patterns by fiber-optic distributed temperature sensing’ by Liliana Rose et al. *Water Resources Research* **50**: 5372–5374 DOI: 10.1002/2013WR014979
- Selker JS, van de Giesen N, Westhoff M, Luxemburg W, Parlange MB. 2006a. Fiber optics opens window on stream dynamics. *Geophysical Research Letters* **33** (24): L24401 DOI: 10.1029/2006GL027979
- Shuster WW. 1986. Water Resources and Natural Control Processes., Wang LK, , Pereira NC (eds). Humana Press: Totowa, NJ; 107–138. DOI: 10.1007/978-1-4612-4822-4_3
- Tristram DA, Krause S, Levy A, Robinson ZP, Waller RI, Weatherill JJ. 2015. Identifying spatial and temporal dynamics of proglacial groundwater – surface-water exchange using combined temperature-tracing methods. *Freshwater Science* **34** (October 2013): 99–110 DOI: 10.1086/679757.
- van de Giesen, N., Steele-Dunne, S. C., Jansen, J., Hoes, O., Hausner, M. B., Tyler, S., & Selker, J. (2012). Double-ended calibration of fiber-optic Raman spectra distributed temperature sensing data. *Sensors*, 12(5), 5471–5485. <https://doi.org/10.3390/s120505471>.
- Vercauteren N, Huwald H, Bou-Zeid E, Selker JS, Lemmin U, Parlange MB, Lunati I. 2011. Evolution of superficial lake water temperature profile under diurnal radiative forcing.

Water Resources Research **47**: 1–10 DOI: 10.1029/2011WR010529

Warren DR, Sebestyen SD, Josephson DC, Lepak JM, Kraft CE. 2005. Acidic Groundwater Discharge and in Situ Egg Survival in Redds of Lake-Spawning Brook Trout. *Transactions of the American Fisheries Society* **134** (5): 1193–1201 DOI: 10.1577/T04-180.1

Appendix S1: Quantification of interfacial heat transfer and net-advective heat flux

Net heat fluxes across the water surface (G in $W m^{-2}$) following equations 1 to 13 have been calculated as (Henderson-Sellers, 1986):

$$G = R_n - \lambda E - H \quad (\text{eq. 1})$$

where

$$R_n = R_{ns} - R_{nl} \quad (\text{eq. 2})$$

$$R_{nl} = L_u - L_d \quad (\text{eq. 3})$$

With L_d , downward long-wave radiation, L_u , upward long-wave radiation, R_{nl} , net long-wave radiation, R_{ns} , net short-wave radiation, R_n , net radiation, H , sensible heat, λE , latent heat and G , net heat fluxes across the water surface.

The calculation of net heat fluxes across the water surface (G in $W m^{-2}$) considered the following processes:

1. Net short wave solar radiation penetrating the water surface (R_{ns} in $W m^{-2}$) (Fritz *et al.*, 1980a):

$$R_{ns} = R_s \times (1 - A_s) \quad (\text{eq. 4})$$

with short wave reflectivity $A_s = 0.06$ and R_s (solar or shortwave radiation).

2. Downward long wave radiation (L_d in $kJ m^{-2} d^{-1}$) (Henderson-Sellers, 1986):

$$L_d = (1 - A_s) \times \varepsilon_a \times \sigma \times T_{ak}^4 \quad (\text{eq. 5})$$

with Boltzmann constant, $\sigma = 4.896 \times 10^{-6} \text{ kJ m}^{-2} \text{ d}^{-1} \text{ K}^4$, atmospheric emissivity (dimensionless) ε_a and water surface reflectance to long wave radiation $A_s = 0.03$ and absolute air temperature in Kelvin, T_{ak} . ε_a is calculated as follows [Wunderlich, 1972].

$$\varepsilon_a = 0.937 \times 10^{-5} \times T_{ak}^2 \times (1 + 0.17 \times C_c^2) \quad (\text{eq. 6})$$

with cloud cover coefficient (C_c), $C_c = 1$ (overcast), $C_c = 0.5$ (partly cloudy), $C_c = 0$ (clear) with absolute air temperature in Kelvin, T_{ak} .

3. Upward long wave radiation (L_u in $kJ m^{-2} d^{-1}$) (Henderson-Sellers, 1986) :

$$L_u = \varepsilon_w \times \sigma \times T_{wk}^4 \quad (\text{eq. 7})$$

with emissivity from water $\varepsilon_w = 0.97$, Boltzmann constant, $\sigma = 4.896 \times 10^{-6} \text{ kJ m}^{-2} \text{ d}^{-1} \text{ K}^4$ and absolute water temperature in Kelvin, T_{wk} .

4. Latent heat transfer (λE ; in $kJ m^{-2} d^{-1}$) (Ryan *et al.*, 1974):

$$\lambda E = (e_s - e_a) \times \left[\lambda \times (T_{wv} - T_{av})^{1/3} + b_0 \times u_2 \right] \quad (\text{eq. 8})$$

with λ and b_0 as constants with values of $311.02 \text{ kJ m}^{-2} \text{ d}^{-1} \text{ mm Hg}^{-1} \text{ K}^{-1/3}$ and $368.61 \text{ kJ m}^{-2} \text{ d}^{-1} \text{ mm Hg}^{-1} (\text{m s}^{-1})$ respectively, wind velocity, $u_2 (\text{m s}^{-1})$ at a reference height of 2 m, saturated vapor pressure at the current water temperature, $e_s (\text{mm Hg})$ (Troxler *et al.*, 1977), water

vapor pressure immediately above the mesocosm surface, e_a (mm Hg) (Troxler *et al.*, 1977), T_{wv} and T_{av} are the virtual water and air temperatures respectively (°K) (Ryan *et al.*, 1974):

$$e_s = 25.37 \times \exp \left[17.62 - \frac{5271}{T_{wk}} \right] \quad (\text{eq. 9})$$

with absolute water temperature in Kelvin, T_{wk} .

$$e_a = Rh \times 25.37 \exp \left[17.62 - \frac{5271}{T_{ak}} \right] \quad (\text{eq. 10})$$

with Rh, relative humidity in decimal fraction and absolute air temperature in Kelvin, T_{ak} .

$$T_{wv} = \left(\frac{T_{wk}}{[1.0 - (0.378 \times e_s / P)]} \right) \quad (\text{eq. 11})$$

with P= barometric pressure (mm Hg) which was assumed to be equivalent to one atmosphere (760 mm Hg) for the current study.

$$T_{av} = \left(\frac{T_{ak}}{[1.0 - (0.378 \times e_a / P)]} \right) \quad (\text{eq. 12})$$

5. Sensible heat transfer (H in $\text{kJ m}^{-2} \text{d}^{-1}$) (Ryan *et al.*, 1974):

$$H = \lambda E \times 0.61 \times 10^{-3} P \times \frac{(T_{wk} - T_{ak})}{(e_s - e_a)} \quad (\text{eq. 13})$$

Change in internal energy (E, in J) over a time interval Δt related to components of the net heat fluxes across the water surface (G) is calculated as:

$$E_{Rns} = R_{ns} \times A_0 \times \Delta t \quad (\text{eq. 14})$$

$$E_{Ld} = L_d \times A_0 \times \Delta t \quad (\text{eq. 15})$$

$$E_{Lu} = L_u \times A_0 \times \Delta t \quad (\text{eq. 16})$$

$$E_{\lambda E} = \lambda E \times A_0 \times \Delta t \quad (\text{eq. 17})$$

$$E_H = H \times A_0 \times \Delta t \quad (\text{eq. 18})$$

$$A_0 = 2\Delta z\Delta x + 2\Delta z\Delta y + \Delta x\Delta y \quad (\text{eq. 19})$$

With A_0 = area (m^2), Δx =length (m), Δy =width (m) and Δz =height (m).

At $t=0$ the internal energy within the control volume is:

$$E_{t=0} = \rho \times (\Delta x\Delta y\Delta z) \times U_{t=0} \quad (\text{eq. 20})$$

At $t=\Delta t$ the internal energy within the control volume is:

$$E_{t=\Delta t} = \rho \times (\Delta x\Delta y\Delta z) \times U_{t=\Delta t} \quad (\text{eq. 21})$$

With U, Internal energy per unit mass of fluid (J kg^{-1}).

Therefore, change on internal energy within the control volume is:

$$\Delta E = \rho \times (\Delta x\Delta y\Delta z) \times \Delta U \quad (\text{eq. 22})$$

Where

$$\Delta U = U_{t=\Delta t} - U_{t=0} \quad (\text{eq. 23})$$

By conservation of energy:

$$\Delta E = E_{in} - E_{out} + E_{gw} - E_{hb} - E_H - E_{\lambda E} + E_{Rns} + E_{Ld} - E_{Lu} \quad (\text{eq. 24})$$

where, E_{in} , advected anergy in the control volume by inflow water, E_{out} , advected energy out of the control volume by outflow water, E_{gw} , advected energy in the control volume by simulated groundwater injection and E_{hb} , energy by sediment conduction.

For a system that performs a small amount of work on its surroundings, the change in internal energy manifests as a change in temperature:

$$dU = C_p \times dT \quad (\text{eq. 25})$$

$$\Delta U \approx C_p \times \Delta T \quad (\text{eq. 26})$$

With heat capacity, $C_p = 4180 \text{ J kg}^{-1} \text{ }^\circ\text{C}^{-1}$, ΔT and dT , change of temperature.

Therefore, change in internal energy can be expressed as:

$$\Delta E \cong \rho \times \sum_{i=1}^{Nm} (\Delta x \Delta y \Delta z) \times C_p \times \Delta T_i \quad (\text{eq. 27})$$

Where $Nm=1944$, total number of FO-DTS measurement locations, i , each measurement location, $\Delta x \Delta y \Delta z \text{ (m}^3\text{)}$, control volume of each FO-DTS measurement, density of water, $\rho_w = 10^3 \text{ kg m}^{-3}$ and ΔT_i , change of temperature over the interval Δt in location i .

Going back to equation 24 and grouping together the atmospheric components of energy into a single term; E_G , energy transferred across the interface:

$$E_G = -E_H - E_{\lambda E} + E_{Rns} + E_{Ld} - E_{Lu} \quad (\text{eq. 28})$$

Now change of internal energy can be expressed as,

$$\Delta E = E_{in} - E_{out} + E_{gw} - E_{hb} + E_G \quad (\text{eq. 29})$$

And the sum of the total advected energy can be calculated as,

$$\Delta E - E_G = E_{in} - E_{out} + E_{gw} \quad (\text{eq. 30})$$

References appendix S1

- Fritz JJ, Meredith DD, Middleton AC. 1980. Non-steady state bulk temperature determination for stabilization ponds. *Water Research* **14**: 413–420 DOI: 0043-1354/80/0501-0413\$02.00/0
- Henderson-Sellers B. 1986. Calculating the surface energy balance for lake and reservoir modeling: A review. *Reviews of Geophysics* **24** (3): 625 DOI: 10.1029/RG024i003p00625
- Ryan PJ, Harleman DRF, Stolzenbach KD. 1974. Surface Heat Loss From Cooling Ponds. *Water Resources Research* **10** (5)
- Troxler RW, Thackston EL, Robert W. 1977. Predicting the Rate of Warming of Rivers

below Hydroelectric Installations. *Water Environment Federation* **49** (8): 1902–1912

Wunderlich, W.O. 1972. Heat and mass transfer between a water surface and the atmosphere. Lab. Report No. 14, Tennessee Valley Authority Engineering Laboratories, Norris, TN.

Cited by: Nath, S.S., 1996. Development of a Decision Support System for Pond Aquaculture. Oregon State University.

Appendix S2 Nomenclature

G ($W m^{-2}$): net heat fluxes across the water surface.

L_d ($kJ m^{-2} d^{-1}$): downward long-wave radiation

L_u ($kJ m^{-2} d^{-1}$): upward long-wave radiation

R_{nl} ($kJ m^{-2} d^{-1}$): net long-wave radiation

R_{ns} ($W m^{-2}$): net short-wave radiation

R_n ($W m^{-2}$): net radiation

H ($kJ m^{-2} d^{-1}$): sensible heat

λE ($kJ m^{-2} d^{-1}$): latent heat.

A_s (dimensionless): short wave reflectivity

R_s ($W m^{-2}$): solar or shortwave radiation.

σ ($kJ m^{-2} d^{-1} K^{-4}$): Boltzmann constant.

ϵ_a (dimensionless): atmospheric emissivity.

A_s (dimensionless): water surface reflectance to long wave radiation.

T_{ak} (Kelvin): absolute air temperature in Kelvin.

C_c (dimensionless): cloud cover coefficient.

ϵ_w (dimensionless): emissivity from water.

T_{wk} (Kelvin): absolute water temperature.

λ ($kJ m^{-2} d^{-1} mm Hg^{-1} K^{-1/3}$): constant

b_0 ($kJ m^{-2} d^{-1} mm Hg^{-1} (m s^{-1})$): constant.

u_2 ($m s^{-1}$): wind velocity, at a reference height of 2 m.

e_s ($mm Hg$): saturated vapor pressure at the current water temperature.

e_a ($mm Hg$): water vapor pressure immediately above the pond surface.

T_{wv} (Kelvin): virtual water temperatures.

T_{av} (Kelvin): virtual air temperatures.

Rh (dimensionless): relative humidity in decimal fraction.

P ($mm Hg$): barometric pressure.

E (J): Internal energy of the system.

ΔE (J): Change in internal energy of the system.

Δt (seconds): time interval.

A_0 (m^2): area of the control volume.

Δ_x (m): length of the control volume.

Δ_y (m): width of the control volume.

Δ_z (m): height of the control volume.

U ($J\ kg^{-1}$): internal energy per unit mass of fluid.

ΔU ($J\ kg^{-1}$): change in internal energy per unit mass of fluid.

E_{in} (J): advected energy in the control volume by inflow water

E_{out} (J): advected energy out of the control volume by outflow water

E_{gw} (J): advected energy in the control volume by simulated groundwater injection.

E_{hb} (J): energy by sediment conduction.

C_p ($J\ kg^{-1}\ ^\circ C^{-1}$): heat capacity.

ΔT and dT ($^\circ C$): change of temperature.

Nm : total number of FO-DTS measurement locations.

ρ_w ($kg\ m^{-3}$): density of water

ΔT_i ($^\circ C$): change of temperature over the interval Δt in location i .

E_G (J): energy transferred across the interface.

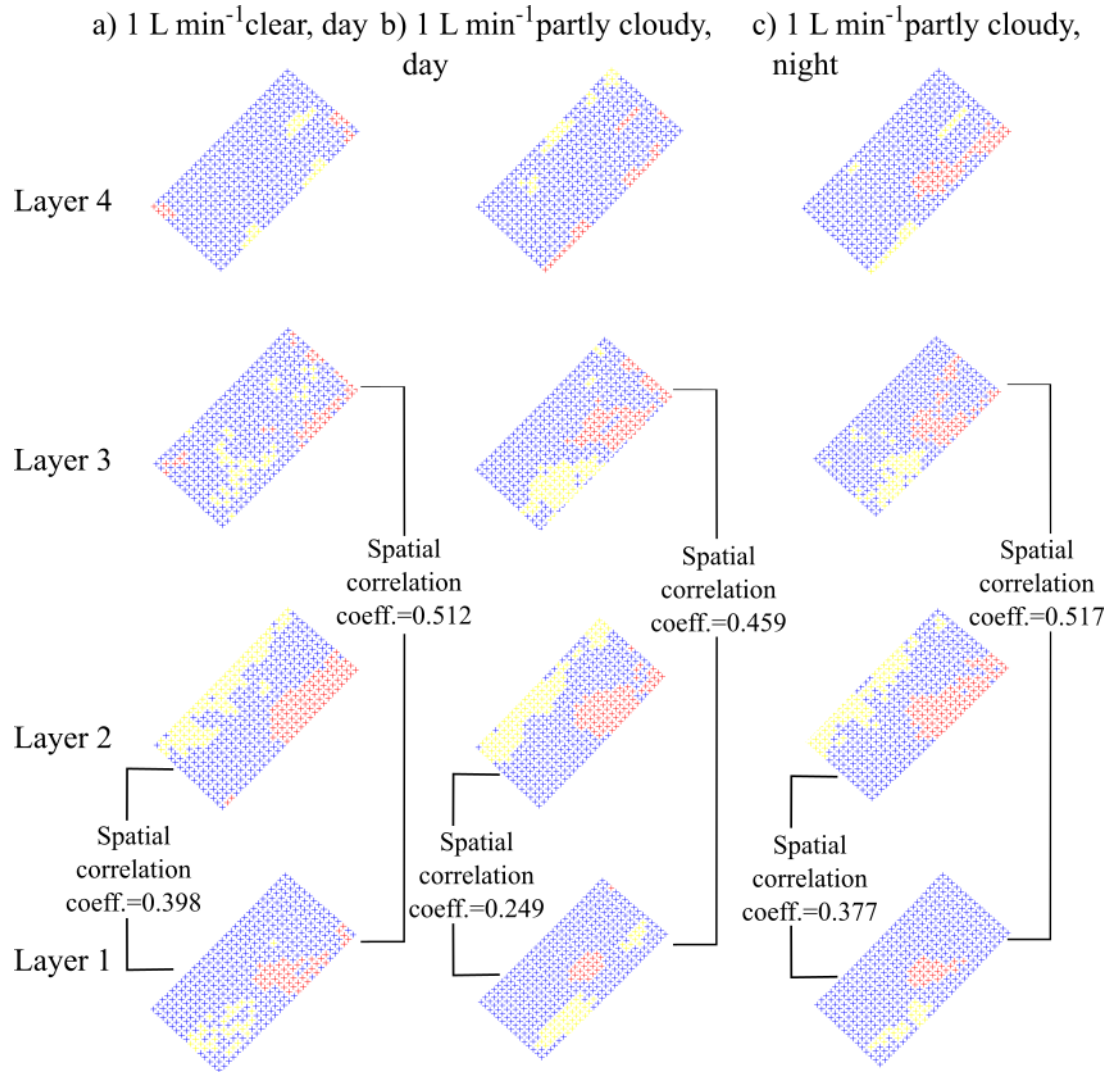


Figure S1 Comparison of LISA maps and spatial correlation coefficients between layer 1 and 2 and layer 1 and 3 for datasets: a) 1 L min^{-1} clear conditions, daytime, b) 1 L min^{-1} partly cloudy conditions, daytime and c) 1 L min^{-1} partly cloudy conditions, night-time. From top row to bottom row: layer 4, layer 3, layer 2 and layer 1.

Table S1 Spatial correlation coefficients between layers.

	Layer n°	Day				Night			
		1	2	3	4	1	2	3	4
1 L min ⁻¹ Clear	1	1	0.39808	0.51153	0.14203	1	0.73808	0.51705	-0.8551
	2	0.39808	1	0.24951	0.05932	0.73808	1	0.50801	-0.18037
	3	0.51153	0.24951	1	0.04728	0.51705	0.50801	1	-0.11156
	4	0.14203	0.05932	0.04728	1	-0.8551	-0.18037	-0.11156	1
1 L min ⁻¹ Partly cloudy	1	1	0.24911	0.45869	-0.1161	1	0.37761	0.51711	0.28616
	2	0.24911	1	0.58511	0.61316	0.37761	1	0.54338	0.41679
	3	0.45869	0.58511	1	0.28031	0.51711	0.54338	1	0.50589
	4	-0.1161	0.61316	0.28031	1	0.28616	0.41679	0.50589	1
1 L min ⁻¹ Overcast	1	1	0.41457	0.48095	0.42329	1	0.74711	0.6806	0.5718
	2	0.41457	1	0.60944	0.66255	0.74711	1	0.72155	0.60979
	3	0.48095	0.60944	1	0.81466	0.6806	0.72155	1	0.83116
	4	0.42329	0.66255	0.81466	1	0.5718	0.60979	0.83116	1
5.5 L min ⁻¹ Clear	1	1	0.51591	0.32147	0.17959	1	0.64121	0.47728	0.13437
	2	0.51591	1	0.59571	0.56061	0.64121	1	0.75321	0.11554
	3	0.32147	0.59571	1	0.68505	0.47728	0.75321	1	0.23392
	4	0.17959	0.56061	0.68505	1	0.13437	0.11554	0.23392	1
5 L min ⁻¹ Overcast	1	1	0.79544	0.63641	0.54602	1	0.75846	0.60806	0.42685
	2	0.79544	1	0.88935	0.79137	0.75846	1	0.87773	0.68253
	3	0.63641	0.88935	1	0.93334	0.60806	0.87773	1	0.8936
	4	0.54602	0.79137	0.93334	1	0.42685	0.68253	0.8936	1
15 L min ⁻¹ Overcast	1	1	0.84675	0.65938	0.26386	1	0.85239	0.68532	0.28563
	2	0.84675	1	0.88841	0.40424	0.85239	1	0.89219	0.44944
	3	0.65938	0.88841	1	0.45033	0.68532	0.89219	1	0.50333
	4	0.26386	0.40424	0.45033	1	0.28563	0.44944	0.50333	1

Mesocosm experiments identifying hotspots of groundwater upwelling in a water column by fiber optic distributed temperature sensing

4 Thermal infrared imaging for detection of groundwater at the surface of stagnant freshwater bodies

Amaya I. Marruedo Arricibita_{a,b}, Stephen J. Dugdale_c, Stefan Krause_c, David M. Hannah_c and Jörg Lewandowski_a

_a Department of Ecohydrology, Leibniz-Institute of Freshwater Ecology and Inland Fisheries, 12587 Berlin, Germany.

_b Department of Geography, Humboldt University of Berlin, 10099 Berlin, Germany.

_c School of Geography, Earth and Environmental Sciences, University of Birmingham, B15 2TT Birmingham, United Kingdom.

Published in: Journal of Hydrology

Marruedo Arricibita AI, Dugdale SJ, Krause S, Hannah DM, Lewandowski J. 2018. Thermal infrared imaging for the detection of relatively warm lacustrine groundwater discharge at the surface of freshwater bodies. *Journal of Hydrology* **562**: 281–289 DOI: 10.1016/j.jhydrol.2018.05.004

Received 24 October 2017; Received in revised form 29 April 2018; Accepted 3 May 2018
Available online 04 May 2018

0022-1694/ © 2018 Elsevier B.V. All rights reserved.

Only for non-commercial use.

Abstract

Thermal infrared (TIR) imaging has been previously applied to survey relatively large thermal footprints in coastal zones, lakes, reservoirs and rivers. In freshwater systems, the buoyancy of relatively warm groundwater during the winter months allows for the surface identification of groundwater discharge or thermal pollution using TIR imaging. However, information regarding the performance of TIR for resolving this warm groundwater upwelling is limited, particularly at fine spatial scales and variable discharge rates. In order to evaluate the suitability of TIR to trace warm groundwater upwelling at the water surface of lakes, ponds and reservoirs (e.g. lacustrine groundwater discharge (LGD) in shallow near-shore zones) we conducted a mesocosm experiment with a TIR camera situated 4 m above the water surface to capture thermal patterns in response to different groundwater discharge rates, weather conditions and the diurnal cycle. A fiber optic distributed temperature sensing system (FO-DTS) installed at 2 cm below the water surface was used to ground-truth spatial patterns observed in TIR images. Results show the impacts of both the diurnal cycle of net radiation and prevailing weather conditions on the accuracy of TIR imaging for resolving warm groundwater discharge. Most reliable results were obtained under overcast weather conditions and during the night. The results of our study provide guidance for those looking to use TIR for conducting thermal tracing of LGD at the surface of freshwater bodies during winter.

Keywords: TIR, FO-DTS, groundwater, lake, heat tracing, leakage

4.1 Introduction

The use of thermal infrared (TIR) remote sensing is increasingly popular in the earth and environmental sciences for mapping of temperature patterns and thermal anomalies in water bodies (Dugdale, 2016). As such, TIR imaging has been applied in a wide range of contexts for monitoring of naturally occurring natural processes such as submarine groundwater discharge (SGD) in coastal areas (Johnson et al., 2008; Lee et al., 2016; Tamborski et al., 2015), groundwater discharge in streams and lakes (Hare et al., 2015; Wawrzyniak et al., 2016), volcanic activity (Davies et al., 2008) or hydrothermal systems (Neale et al., 2016). It is also used for the identification of anthropogenic impacts on hydrological systems including thermal effluent from power plants (Wang et al., 2016) and surface water contamination by illegal sewers or storm drainage (Lega and Napoli, 2010).

TIR imaging allows for the measurement of water surface temperature at high spatial resolution across a wide range of scales (Dugdale, 2016). While TIR has been relatively under-used until recently (in comparison to other remote sensing techniques), the increasing affordability of TIR has led to a recent uptake of this technology. This increased use of TIR has driven a range of literature reviewing the technological applications and limitations of satellite, airborne and ground-based TIR remote sensing (e.g. Dugdale, 2016; Handcock et al., 2012; Mundy et al., 2017; Sobrino et al., 2016) for the monitoring and mapping of water temperature anomalies in both marine and freshwater environments.

In marine systems, Submarine Groundwater Discharge (SGD) is a major source of nutrients and other chemical components (Burnett et al., 2006, 2003; Danielescu and MacQuarrie, 2011; Johnson et al., 2008; Taniguchi et al., 2002). SGD is known to affect water quality and phytoplankton dynamics, potentially leading to environmental phenomena such as eutrophication and algal blooms (Anderson et al., 2002; Hu et al., 2006; Lee and Kim, 2007).

In freshwater systems, groundwater discharge can create discrete temperature anomalies that serve as thermal refugia for fish and other ectothermic species (Baker et al., 2014; Brabrand et al., 2002; Hayashi and Rosenberry, 2002; Warren et al., 2005). Groundwater discharge can also impact nutrient budgets of lentic ecosystems (Boulton et al., 1998; Meinikmann et al., 2013; Shaw et al., 1990) and may play a role as a potential vector for pollution in streams and lakes (Nakayama and Watanabe, 2008).

Due to the importance of groundwater discharge in marine and freshwater systems, the literature abounds with TIR remote sensing-based methods for the detection of diffuse and discrete groundwater discharge. In marine systems, Johnson et al. (2008) demonstrated that

TIR imagery is an appropriate tool for mapping SGD. More recently, Tamborski et al. (2015) combined airborne TIR with radium ($^{223,224}\text{Ra}$) and radon (^{222}Rn) surface water sample collection to quantify diffuse SGD. Similarly, Lee et al. (2016) demonstrated how combining aerial TIR imagery with field observations can be used to identify large groundwater inputs from coastal aquifers to the ocean. In freshwater environments, Schuetz and Weiler (2011) used ground based TIR thermography to detect discrete groundwater discharge into streams. A similar experiment by Briggs et al. (2016) demonstrated how ground-based TIR can reveal fine scale groundwater discharge patterns which would have not been resolved by other (coarser) methodologies. At larger scales, Wawrzyniak et al. (2016) used airborne TIR to resolve cold water patches in a riverine system as a function of the temperature difference between the river (in low flow conditions) and groundwater inputs.

Groundwater detection using TIR is more straightforward in marine than freshwater environments due to the large density difference between groundwater inflow and the saline water column. Unlike in marine environments, where these salinity differences drive SGD upwelling, groundwater upwelling in freshwater systems is largely driven by temperature. Even small temperature differences may provoke groundwater-surface water density gradients that approach levels of buoyancy similar to that of groundwater discharge in saline systems (Lewandowski et al., 2013). This buoyancy, amongst other factors, enables the detection of groundwater upwelling at the surface of freshwater bodies. However, because the groundwater-surface water temperature difference can vary substantially, the ability of TIR to resolve groundwater upwelling is less consistent than in marine systems. While many publications (e.g. Briggs et al., 2016, 2013; Danieleescu et al., 2009; Dugdale et al., 2015; Tcherepanov et al., 2005; Wawrzyniak et al., 2016) document the use of TIR to detect groundwater upwelling in freshwater bodies, the vast majority of these studies focus on the detection of cool thermal anomalies in summer, with relatively little attention paid to the quantification of warm groundwater-surface water exchanges in winter. Furthermore, the examples that do exist which describe TIR imaging to detect winter groundwater upwelling in freshwater environments focus on groundwater discharge: (i) in streams (e.g. Hare et al., 2015; Wirth et al., 2012); (ii) at marine beaches (Röper et al., 2014) and; (iii) in vernal and peatland pools (Frisbee et al., 2016), rather than in lentic waterbodies where mixing patterns are substantially different.

In addition, while previous studies (e.g. Briggs et al., 2016; Dugdale et al., 2015; Hare et al., 2015; Schuetz et al., 2012; Schuetz and Weiler, 2011) highlight the reasonable ability of TIR

remote sensing to detect thermal anomalies related to groundwater discharge in real world freshwater environments, there remains a lack of formal ‘laboratory-style’ data evaluating the precise hydrological (e.g. discharge rates) and meteorological (e.g. weather conditions) conditions under which TIR remote sensing best detects groundwater upwelling, especially during the winter season.

In light of this these knowledge gaps, we present the results of a mesocosm experiment designed to test the suitability of TIR for tracing the upwelling of discrete lacustrine groundwater discharge (LGD) in lentic waterbodies (e.g. in shallow near-shore zones of lakes, ponds and small reservoirs). Our specific objectives were: (i) to compare (both visually and quantitatively) TIR observations of surface water temperature with simultaneously-collected FO-DTS temperature data measured 2 cm below the water surface and (ii) to evaluate the suitability of ground-based TIR for the detection of spatial patterns in relatively warm groundwater upwelling as a function of different discharge rates, weather conditions and the diurnal cycle.

4.2 Methods

4.2.1 Experimental design

The mesocosm used in this study contained two inlets and one outlet (Fig. 4.1). Water from Lake Müggelsee located in Berlin, Germany (mean of 4.7 °C over the course of the experiment) was injected into the corner of the mesocosm via one of the inlets (rate $\approx 33 \text{ L min}^{-1}$). The inlet remained open at all times to keep water temperatures well-mixed and relatively constant. The other inlet was installed at the base of the mesocosm and used for controlled warm water injections. A hosepipe was connected to this inlet to provide warm water. The pipe was insulated with foam to reduce cooling along the flow path from the tap to the mesocosm (approximately 65 m). Temperature of the injected flow (measured at halfway between the tap and mesocosm) ranged from 14 to 16 °C. A nozzle was connected to the end of the inlet and covered with sediment to realistically simulate dispersal of the injected water through a layer of sediment. Finally, an outlet at the other side of the mesocosm was used to maintain a constant water level of 0.82 m. Discharge at this outlet varied from 34 to 48 L min^{-1} depending on the warm water injection rate (Marruedo Arricibita et al., 2018).

For the FO-DTS surveys, an aluminium frame of dimensions 4 m \times 2 m \times 1.5 m (Fig. 4.1) was installed within the mesocosm. The aluminium frame was used to support the FO cable in a grid-like pattern 2 cm below the water surface (Fig. 4.1). The FO cable grid consisted of 15 lines (rows) of cable spaced 12.5 cm apart. An ULTIMA-S DTS (SILIXA Ltd.) instrument

with a sampling resolution of 12.5 cm was used for the FO-DTS surveys. This experimental setup essentially resulted in gridded temperature measurements with a resolution of 12.5 cm. Temperatures were acquired with a temporal frequency of 10 s (mean of the preceding 10 s period; essentially the integration time of the FO-DTS). 500 m of 2.8 mm diameter Corning ClearCurve simplex fibre (loose tube, 1 multimode fibre, both ends terminated with E2000/APC connectors) were deployed for the experiments. This selected FO cable specification allowed bending and was thus appropriate for installation in the aluminium frame (Marruedo Arricibita et al., 2018).

Thermal images were acquired from a TIR camera installed 4 m above the mesocosm on a steel frame (Fig. 4.1) and oriented perpendicular to the water surface. The FO-DTS measurements were used for ground truthing of the TIR results which only capture direct surface temperatures (ie. the upper 10 μm of the water surface; Torgersen et al., 2001). We used a VarioCAM® hr head camera (InfraTec GmbH) with 640 \times 480 pixels (7.5–14 μm). The camera was equipped with a wide angle lens with focal length of 12.5 mm and field of view (FOV) $65^\circ \times 51^\circ$. The temperature measurement range is -40 to 1200°C and reported measurement accuracy is $\pm 2^\circ\text{C}$ or $\pm 2\%$.

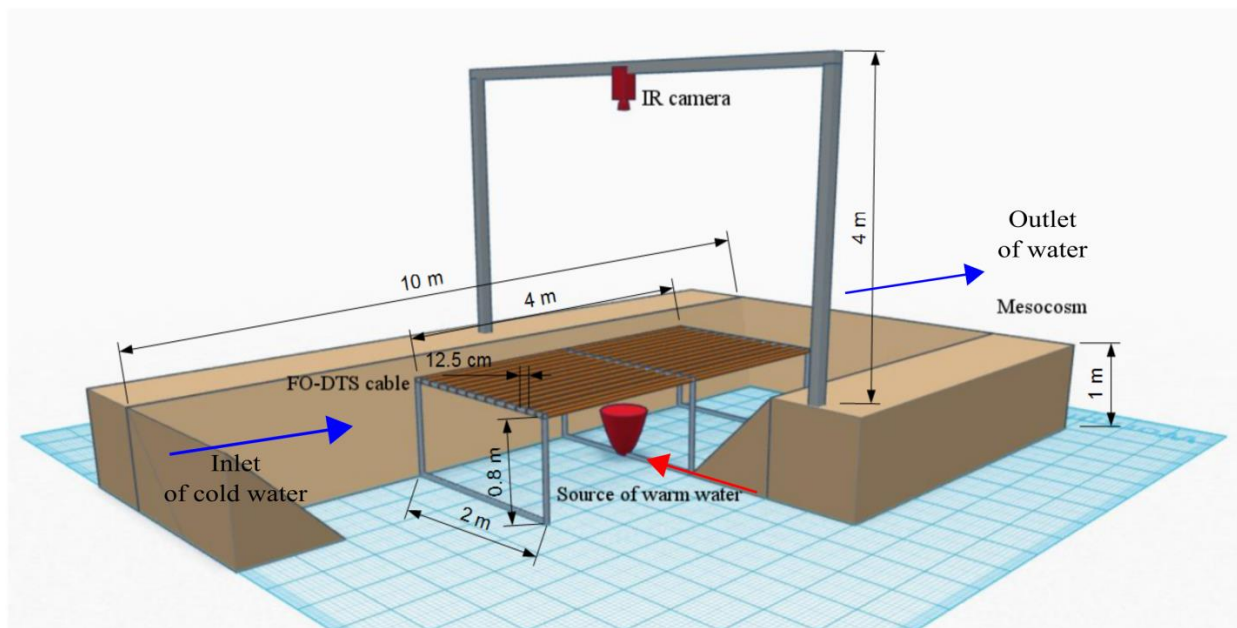


Figure 4.1 Schematic of the mesocosm experimental design including TIR setup and the upper layer of the FO-DTS.

4.2.2 Measurement protocol and calibration

FO-DTS

Calibration of the FO-DTS was carried out using reference sections of fibre optic cable immersed within ice baths containing a mix of ice and water (maintained at $\sim 0.2^\circ\text{C}$). The first and last 20 m of fibre optic cable were submerged in this well mixed ice bath, and an external temperature probe connected to the DTS device used to monitor calibration bath temperatures independently. For differential loss corrections, fixed value settings were chosen along the relatively short cable (500 m) without any splices (Marruedo Arricibita et al., 2018). A default value of 0.255 dB/km was used. This is the expected value for Corning ClearCurve OM3 fibre. A two-way single-ended measurement setup was deployed with alternating bidirectional monitoring of the light pulse sent from the DTS device (Krause and Blume, 2013).

TIR

The TIR camera used in this study has an uncooled microbolometer FPA detector (uncooled Focal Plane Array) with an internal shutter. Small alterations in the microbolometer manufacturing process lead to non-homogeneous pixel specific sensor parameters which can induce temperature non-uniformities in the image (Tempelhahn et al., 2016, 2015). The camera's non-uniformity correction system (NUC) compensates for these minor sources of error by using an internal optical shutter that periodically covers the whole camera field of view to provide a reference temperature. In this manner, the TIR camera performed a NUC (also known as a Flat Field Correction) every 90 s to correct for temperature or thermal drift effects on the measurements (eg. Dugdale, 2016; Handcock et al., 2012; Tempelhahn et al., 2015, 2016; Zuo et al., 2011).

A simple MATLAB function was developed to compensate for the effects of vignetting which created a minor systematic radial temperature gradient in the raw TIR images. This was achieved by applying a convolution filter with a smoothing window of 25 pixels to the raw imagery and subsequently creating a new image whereby each pixel is assigned a value equal to the difference between its smoothed value and the mean of all pixels within the image. The resulting raster essentially contained an inverse image of the vignetting effect which was then subtracted from the raw TIR image resulting in a final corrected TIR image.

Since the aim of the present study is to evaluate the suitability of TIR to determine spatial patterns of warm water upwelling, rather than quantifying rates of upwelling per se, absolute temperatures were not of specific interest and were not calculated for the data obtained by the

TIR camera. Instead, we compared the TIR-derived data to the FO-DTS observations by computing the difference in minimum temperature (ΔT_{\min}) observed by the (corrected) TIR image and the FO-DTS device.

4.2.3 Study period and influence of discharge rates, weather conditions and diurnal cycle

Six 24-h temperature datasets of simultaneously-acquired FO-DTS and TIR data were used in the present study (Table 4.1). The temperature datasets were obtained during 11–27 March 2015. In order to assess the performance of the TIR methodology at different discharge rates and weather conditions, injection rates were varied between 1, 5 and 15 L min⁻¹ under a range of different (ie overcast and clear) sky conditions. Overcast vs. clear weather conditions were inferred from data acquired from a weather station installed alongside the mesocosm, whereby relative solar radiation was defined as the ratio of observed shortwave radiation (measured by the weather station pyranometer) to the computed maximum solar radiation that would be expected using clear sky conditions (after Allan et al., 1998). For example, average relative shortwave radiation measured on 26 March 2015 of 0.17 was considered ‘overcast’ whereas the value on 19 March 2015 of 0.97 was classified as clear. Performance of the TIR methodology was examined at different points throughout the diurnal cycle to evaluate differences between day and night conditions.

Table 4.1 24-hour measurements with FO-DTS and TIR camera. The control dataset is only used as a reference for the initial conditions of the mesocosm measurements and is not included in the results.

Injection rate (L min ⁻¹)	Weather conditions	Date (in March 2015)
0 (control)	overcast	11
1	clear	19
1	overcast	26
5	clear	18
5	overcast	27
15	overcast	12

4.2.4 Comparison of TIR temperature data with FO-DTS temperature data

We assessed the performance of the TIR data for locating and measuring the spatial extent of warm groundwater upwelling by comparing the TIR data with FO-DTS. Because the TIR images essentially contain multiple ‘layers’ of radiation resulting from solar radiation and/ or longwave reflections (from trees, clouds, etc), it is necessary to determine the extent to which the temperature signal from the warm water discharge matches that recorded by the FO-DTS data, in light of these other sources of noise. This was accomplished both visually and quantitatively.

Visual comparison

A direct comparison of the FO-DTS and TIR thermal image data was difficult, given the different spatial resolutions of both methods and the fact that FO-DTS provided a spatially integrated temperature along a 2dimensional cable section while TIR produced gridded temperature data. To enable comparison between the TIR and FO-DTS data, the portion of the TIR image corresponding to the extent of the FO-DTS measurements was extracted from the TIR images of the mesocosm. The TIR images were then down sampled to the same resolution of the FODTS temperature data matrix, allowing the resulting 30×15 pixel TIR matrices to be compared to the FO-DTS grid.

We visually compared the average temperature grids generated by the FO-DTS and TIR approaches for the first 3.5 min of each hour. Although the FO-DTS temperature data showed clearer spatial temperature patterns when averaged over longer periods of time, this was not the case for the temperature data monitored by the TIR camera, presumably due to increased surface movement in comparison to the FO-DTS (submerged at 2 cm below the surface). Indeed, averaging the TIR temperature data over long periods of time resulted in overly blurred or smoothed patterns. Therefore, the decision to focus on the 3.5 min period represented a compromise between the two methods.

Temperature anomalies caused by external factors such as leaves, branches or ducks on the water surface were identified and masked out before plotting the resulting temperature grids for the FO-DTS and TIR data. Temperature values found to be outside of 3 standard deviations above or below the mean were considered outliers due to external factors and were also removed.

Quantitative comparison

In addition to visually comparing the TIR and FO-DTS temperature grids, we quantified spatial correlation between the TIR and FO-DTS grids generated in Section 2.4.1 using Bivariate Global Moran's I. Bivariate Global Moran's I is essentially a global measure of spatial association between two different variables in corresponding neighbourhoods. In this case Bivariate Global Moran's I can thus be understood as an average value representing the correlation between the entire TIR and FO-DTS grids (e.g. Anselin, 1995; Anselin et al., 2002).

4.3 Results

4.3.1 Comparison of TIR temperature data with FO-DTS temperature data

Visual comparison

To highlight differences resulting from variations in injection rate, time of day and technique employed (FO-DTS and TIR), we visually compared pairs of FO-DTS and TIR temperature images with the lowest (ie. worst) and highest (ie. best) spatial correlation (based on Bivariate Global Moran's I coefficients; see Figs. 4.2 and 4.3) under overcast (Fig. 4.2) and clear sky (Fig. 4.3) weather conditions for injection rates of 1 L min⁻¹, 5 L min⁻¹ (Figs. 4.2 and 4.3) and 15 L min⁻¹ (Fig. 4.2). The figures show the averages of ΔT_{min} for the first 3.5 min of each hour.

Overcast conditions: Under overcast conditions with a 1 L min⁻¹ warm water injection rate, the lowest spatial correlation occurred at 20:00 in the evening (Fig. 4.2a). The FO-DTS data showed warmest temperatures on the right side of the image resulting from the injected warm water at the bottom of the mesocosm. Conversely, the TIR data showed warmest temperatures on the left side of the image. This is likely due to the fact that images recorded at this low discharge rate were dominated by thermal reflections of a tree overhanging the left side of the mesocosm, which obscured the temperature signal corresponding to the warm water injection (indicated with a black arrow in Fig. 4.2a, TIR image). In contrast, the best spatial correlation between the FO-DTS and TIR temperature at a 1 L min⁻¹ injection rate occurred at 02:00 in the morning (Fig. 4.2a), whereby there was a strong visual overlap between warmest areas in the FO-DTS and TIR data. Under a 5 L min⁻¹ injection rate, the worst spatial correlation occurred at 07:00 in the morning (Fig. 4.2b). Similar to the 1 L min⁻¹ data, the FO-DTS recorded warmest temperature areas on the right side of the mesocosm, while the TIR

temperature data again indicated warmest temperatures on the left due to reflections from tree cover. The best calculated spatial correlation between FO-DTS and TIR temperature data occurred at 02:00 in the morning (Fig. 4.2b), whereby the FO-DTS and TIR data show a similar extent of warm water. Under an injection rate of 15 L min^{-1} , the worst spatial correlation between FO-DTS and TIR temperature data occurred at 13:00 in the afternoon (Fig. 4.2c), while the best correlation occurred at 20:00 (Fig. 4.2c). Unlike the lower injection rates, both cases showed a good degree of visual similarity between the FO-DTS and TIR temperature grids. Taken together, these results indicate a reasonable degree of similarity between the FO-DTS and TIR data, particularly for the higher injection rates. The TIR signal corresponding to the warm water injection was also clearer at night-time than during the day.

Clear sky conditions: Under clear sky conditions (Fig. 4.3), simulated groundwater upwelling produced by the warm water injection was generally not detected by TIR. Fig. 4.3 shows the FO-DTS and TIR temperature grids corresponding to the lowest and highest spatial correlations. The overall correlation between FO-DTS and TIR was systematically lower than under overcast skies, and no meaningful differences were observed between the computed worst and best spatial correlation values. Thus, there was little visual agreement between the TIR and FO-DTS data for any injection rate, throughout the entire diurnal cycle (see Fig. 4.3a and b).

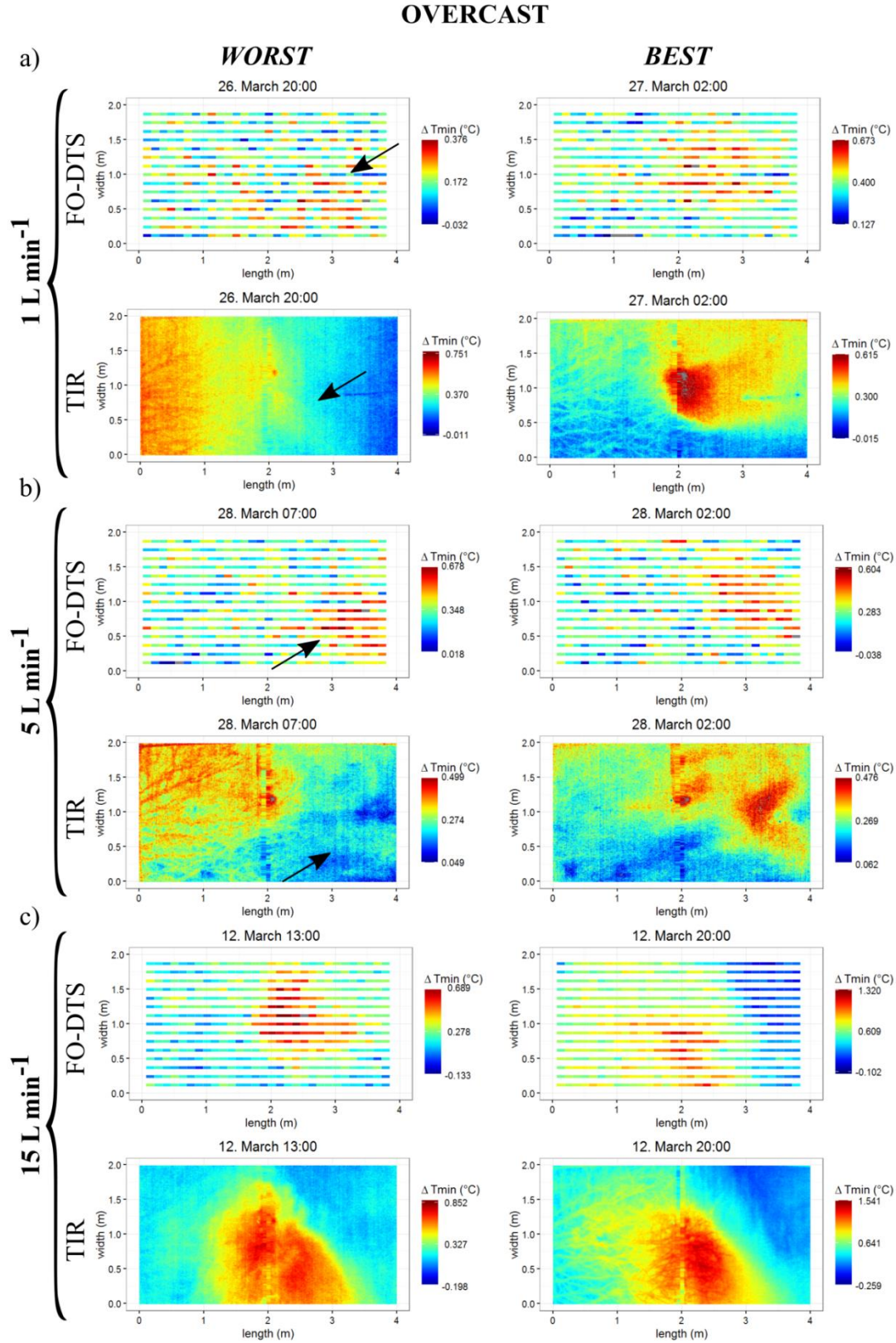


Figure 4.2 Visual comparison of TIR temperature data with FO-DTS temperature data. Worst (left) and best (right) spatially correlated datasets for overcast conditions at three injection rates: a) 1 L min⁻¹, b) 5 L min⁻¹ and c) 15 L min⁻¹. Temperature signal corresponding to the warm water injection is indicated with a black arrow in Fig. 4.2a and b.

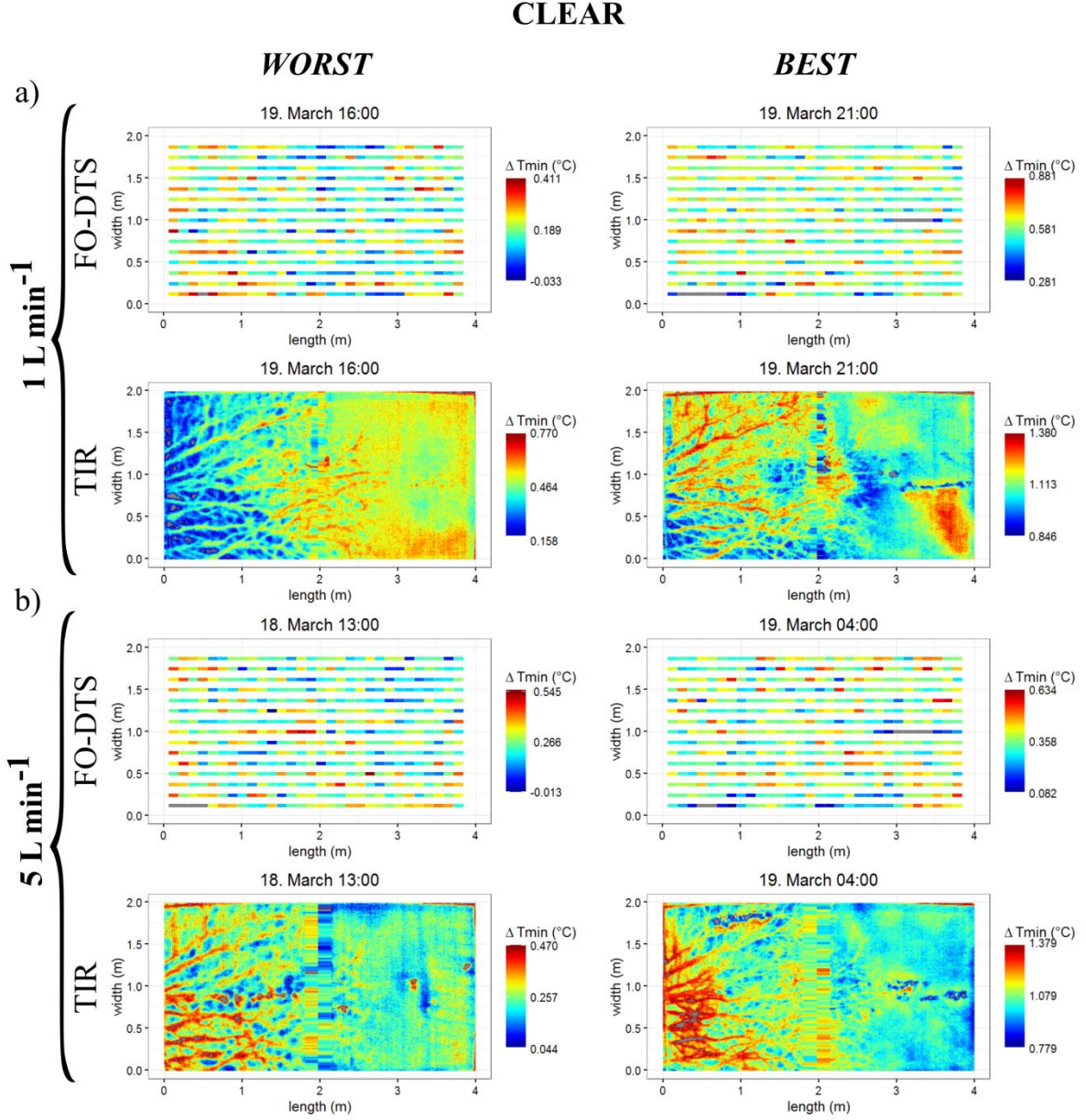


Figure 4.3 Visual comparison of TIR temperature data with FO-DTS temperature data. Worst (left) and best (right) correlated datasets for clear conditions at three injection rates: a) 1 L min^{-1} and b) 5 L min^{-1} .

Quantitative comparison

We calculated Global Moran's I coefficients between FO-DTS and TIR temperature data under overcast (Fig. 4.4) and clear conditions (Fig. 4.5) across the entire 24-h long measurement cycle and for all simulated warm water injection rates (Figs. 4.4 and 4.5: a) 1 L min^{-1} and b) 5 L min^{-1} and Fig. 4c: 15 L min^{-1}) with a view to ascertaining the time and conditions associated with the best and worst performance of the TIR methodology. Generally, we observed that Global Moran's I coefficient values under overcast conditions

were higher than under clear conditions (see Figs. 4.4 and 4.5), with the absolute highest values obtained for the 15 L min^{-1} injection rate (see Fig. 4.4c). Furthermore, for 1 L min^{-1} and 5 L min^{-1} injection rates under overcast conditions, the highest Global Moran's I coefficient values were obtained during night (see Fig. 4.4a and 4.4b). Under clear conditions, Global Moran's I coefficient values (both 1 L min^{-1} and 5 L min^{-1}) were generally lower than those observed under overcast weather conditions, and were often close to 0 or negative (see Fig. 4.5a and b).

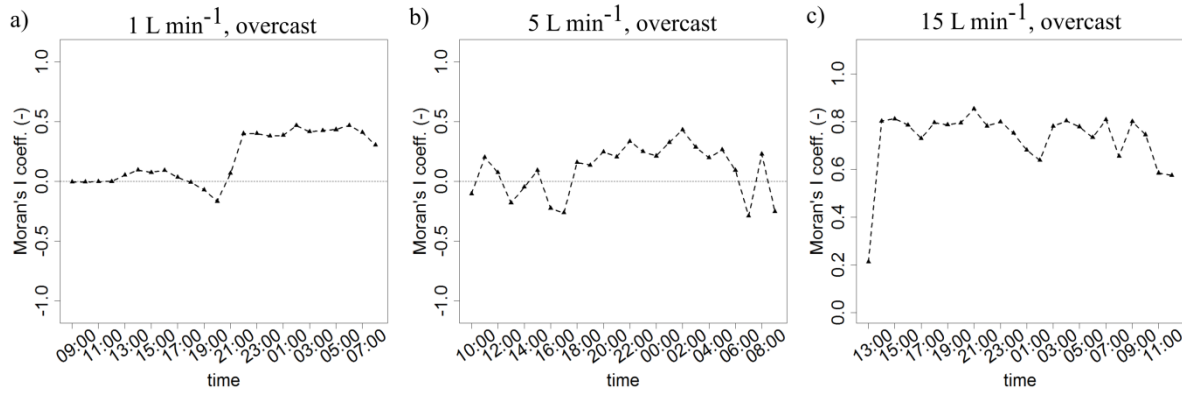


Figure 4.4 Bivariate Global Moran's I values for spatial correlation between FO-DTS and TIR temperature data under overcast weather conditions, for three injection rates: a) 1 L min^{-1} , b) 5 L min^{-1} and c) 15 L min^{-1} .

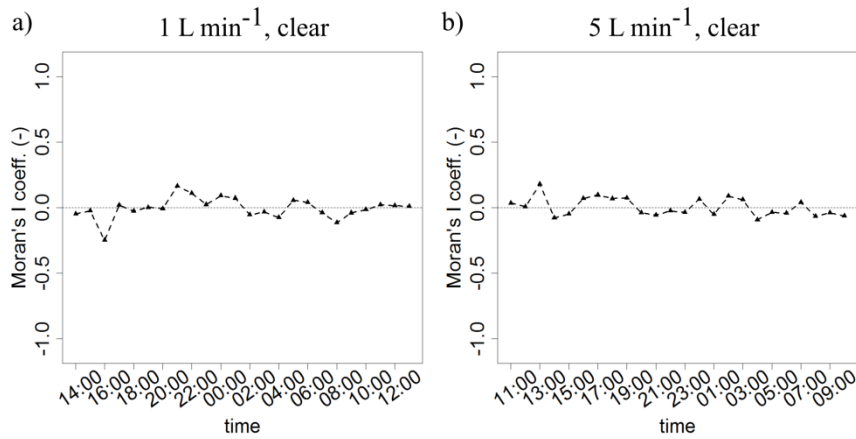


Figure 4.5 Bivariate Global Moran's I values for spatial correlation between FO-DTS and TIR temperature data under clear sky conditions, for two injection rates: a) 1 L min^{-1} and b) 5 L min^{-1} .

4.4 Discussion

4.4.1 Comparison of TIR temperature data with FO-DTS temperature data

Visual and quantitative comparison of the TIR temperatures with FO-DTS data demonstrated that best matches occurred during overcast weather conditions than during clear sky conditions, during night than during day and at higher injection rates than at lower injection rates (Figs. 4.2–4.5). FO-DTS observations provided a spatially-explicit validation for the patterns observed in the TIR images for a range of different discharge rates, weather conditions and points along the diurnal cycle. The FO-DTS setup allowed for the differentiation of thermal anomalies related to groundwater upwelling from thermal anomalies present within the TIR images which were related to other factors (e.g. reflections from vegetation). The use of near-surface mounted FO-DTS to validate TIR in this manner is novel, as the majority of other studies incorporating FO-DTS measurements and TIR use FO-DTS installed at the sediment-water interface (e.g. Lewandowski et al., 2013). In such studies, comparison of TIR images with FO-DTS temperature data is problematic because: a) depth-dependent mixing may fundamentally alter the thermal patterns received by the FO-DTS in comparison with TIR and b) the warming effect of incident radiation at the air water interface (e.g. Benyahya et al., 2012; Marruedo Arricibita et al., 2018; Ouellet et al., 2014) may not be recorded by the bed-mounted FO-DTS. Our experimental setup provides a partial resolution of this problem, allowing for more direct comparison of the two techniques.

4.4.2 Influence of discharge rates, weather conditions and the diurnal cycle

Simulated discharge rates

Higher simulated discharge rates increased the ability of TIR to detect warm upwelling at the surface. The simulated discharge rates in the present study ($1\text{--}15\text{ L min}^{-1}$) are at the higher end of LGD rates reported worldwide (e.g. $745\text{ cm day}^{-1} = 5.2\text{ L m}^{-2}\text{ min}^{-1}$ reported in Rosenberry et al., 2015). Examples of similarly high discrete LGD are found in Karst aquifers or in humic lakes with macropore groundwater discharge, occasionally exceeding 15 L min^{-1} (e.g. Norrström and Jacks, 1996). Nevertheless, we appreciate that the simulated discharge rates are much higher than those typically observed in nature. Our values were chosen with a view to understanding the upper and lower limits of detectability using TIR in high discrete LGD environments under a best-case scenario. Thus, we do not recommend the extrapolation of our results or the use of TIR for studying LGD at the lower end of rates reported in the literature (e.g. $0.005\text{--}124.1\text{ cm day}^{-1}$; Rosenberry et al., 2015).

Influence of weather conditions

The present study builds on the mechanistic findings of Marruedo Arricibita et al. (2018) whereby the propagation of relatively warm water from the sediment to the air-water interface was tracked by several layers of FO-DTS cable in the water column. Marruedo Arricibita et al. (2018) showed that the propagation of relatively warm water heat signal from the sediment to the air-water interface was mainly influenced by the diurnal cycle of net radiation (R_n) and cloud cover, due to the role of R_n in controlling heat gains and losses at the water surface. These findings also have implications for the TIR results. During daytime, R_n values were higher under clear skies than under overcast weather conditions, due to increased incident shortwave radiation. This means that the water surface heated up more than under overcast weather conditions, rendering the signal from the warm water injection (at the base of the mesocosm) difficult to observe with TIR (because of the very small resultant temperature difference between the simulated upwelling and the ambient mesocosm surface temperature). On the contrary, during night-time, a greater amount of net radiation (R_n) was lost during clear sky conditions than under overcast conditions (Marruedo Arricibita et al., 2018). While this increased heat loss explains why the FO-DTS data was not able to properly characterise upwelling (due to rapid dissipation of heat energy at the surface), it does not explain why the TIR images were not readily able to detect the upwelling, as it is this very loss of radiation which is measured by the thermal camera. Instead, we hypothesise that the formation of a (shallow) inverted thermocline resulting from the high surface energy loss may have prevented warm water from reaching the surface prior to mixing, possibly explaining the lack of an observable plume extent in the TIR images.

The TIR sensor measures longwave radiation that is emitted and reflected from the water surface. This means that thermal images obtained from TIR cameras contain information on both water surface temperature and reflections from surrounding vegetation (in this case, tree cover next to the mesocosm) or cloud cover (Anderson and Wilson, 1984; Handcock et al., 2012; Schott, 1994; Torgersen et al., 2001). In addition, the sensor in the TIR camera detects radiation emitted from the upper 0.1 mm of the water surface (Torgersen et al., 2001), whereas the FO-DTS measured true kinetic temperature at 2 cm below the water surface. As a consequence, FO-DTS temperature measurements, unlike the TIR data, were not affected by radiation emitted by surrounding vegetation or clouds.

Under clear sky conditions, the TIR imagery incorporated artefacts generated from longwave reflections of tree cover. These artefacts caused temperature variations at the water surface

and made it extremely difficult to discriminate the extent of the thermal plume associated with the warm water injection. The match with the FO-DTS data (which were not influenced by vegetation reflections) was therefore poor. Conversely, under overcast weather conditions, it was possible to discriminate the extent of the thermal plume associated with the warm water injection in the TIR image. We provide two possible explanations for this phenomenon. First, during overcast conditions, the TIR imagery incorporated longwave reflections not only from vegetation, but also from cloud cover. As a consequence, most reflections from vegetation were masked by bulk reflections of clouds, which provided a relatively uniform background in the TIR image. The thermal plume from the warm water injection into the mesocosm was thus visible against the uniform background, providing an improved degree of similarity between the FO-DTS and TIR data. Second, the decrease in solar radiation under overcast conditions meant that resulting longwave emissions from trees were also diminished, reducing the magnitude of reflections from tree cover.

Influence of the diurnal cycle

Although overcast conditions aided detection of the warm water injection during both day and night, it was generally easier to detect the thermal plume during the night, when longwave reflections from trees beside the mesocosm were minimized. Longwave emissions from vegetation are lower at night because vegetation temperature is generally reduced in comparison to daylight conditions (owing to a lack of incident shortwave radiation at night). This resulted in substantially weaker longwave emissions from vegetation to the water surface, eliminating vegetation reflections in the TIR images and further aiding discrimination of the thermal plume.

4.4.3 Experimental shortcomings and future improvements

The present experiment was conducted in a semi-controlled environment (a mesocosm with simulated groundwater discharge) in order to decrease the number of external influences (e.g. turbulence from waves, vegetation in the water column) on the ability of TIR to detect the warm water injection. This experimental setup allowed us to better isolate and investigate the influence of weather conditions (clear vs overcast) and the diurnal cycle (day vs night), which might otherwise be obscured by other external phenomena. Our results could be applied or extrapolated to shallow lakes up to 1 m deep, or shallow littoral environments, provided wind velocities and mixing were sufficiently similar. However, we acknowledge: (i) that in natural environments, the ability of TIR to detect warm groundwater upwelling in winter is also influenced by a range of other factors and; (ii) the limited number of parameters (discharge

rates, weather conditions and diurnal cycle) included in this study. This experiment is a first attempt to understand under which conditions ground-based TIR remote sensing is a suitable method to detect discrete LGD at the water surface of slow flowing freshwater bodies such as lakes, ponds or reservoirs, in winter. Therefore, we advocate further research that will build upon the lessons learned from the results and conclusions presented in this paper, through the use of more detailed experimental designs capable of examining a larger variation of parameters (e.g. surface water depth, angle of the TIR camera or the range of ΔT between surface water and groundwater) or future measurements in natural conditions (conducted from the shores of lakes).

4.4.4 Implications of results for TIR based monitoring of groundwater upwelling

Our study emphasizes the importance of considering the influences of weather conditions (clear vs overcast) and the diurnal cycle (day vs night) on TIR-based detection of LGD in slow flowing freshwater. The emphasis on the relevance of weather conditions and the diurnal cycle is in agreement with other recent investigations which also highlighted similar findings (e.g. bedrock groundwater seepage detection; Mundy et al., 2017; TIR imaging of high altitude alpine environments; Aubry-Wake et al., 2015). Indeed, in a study designed to assess the influence of air temperature and solar radiation on ground-based TIR measurements of groundwater seepage from bedrock, Mundy et al. (2017) specifically recommended that TIR temperature measurements should be carried out when solar radiation is not present (during night) and in stable weather conditions. This finding supports our results and highlights the importance of conducting monitoring: i) at night and; ii) under overcast weather conditions. Thus, while close-range TIR techniques can constitute an effective tool for monitoring groundwater upwelling, their efficacy depends upon a wide range of environmental factors. Care must therefore be taken when performing similar work to control for the factors detailed in this paper to ensure optimal monitoring results.

We also note that our TIR imagery required post-processing to account for the effects of vignetting. Vignetting results in a circular gradient of decreasing image brightness from the centre of the image to its edges (Gupta, 2018; Lelong et al., 2008). Although commonly associated with optical remote sensing (e.g. Kordecki et al., 2016; Meng et al., 2015), vignetting is also known to impact TIR images in a similar fashion (e.g. Hook et al., 2005; Meier et al., 2011) resulting in generally ‘cooler’ temperatures towards the edges of TIR images. This effect is particularly pronounced with wide angle lenses (Goldman, 2010;

Kelcey and Lucieer, 2012), such as the 12.5 mm ($65^{\circ} \times 51^{\circ}$ field-of-view) model used in our study. While such vignetting is therefore unlikely to present challenges for airborne TIR which benefit from the ability to use narrower field-of-view (FOV) lenses due to increased sensor to object distances, the use of wide FOV lenses is often a necessity in ground-based TIR studies in order to acquire imagery of a given study area in its entirety. Future ground-based studies of discrete LGD should therefore be aware of the potential for temperature bias resulting from the use of wide-angle lenses; such studies may therefore require the application of similar post-processing methodologies to account for this.

4.5 Conclusions

The manifestation of warm water upwelling at the surface of a mesocosm was monitored using TIR and compared to FO-DTS temperature observations for a range of different injection rates. Results show that the diurnal cycle of incoming net radiation as well as weather conditions (clear versus overcast skies) had a substantial effect on the ability of TIR to accurately detect simulated warm water upwelling (in comparison to FO-DTS records). While simulated warm water discharges were generally well detected during overcast conditions and at night, TIR was less able to replicate FO-DTS observations during day and under clear sky conditions. These findings have important implications for the use of TIR imaging to detect discrete LGD at the water surface of slow flowing freshwater bodies in winter.

Acknowledgments and Data

Funding: This work was supported by the European Union's Seventh Framework programme for research; technological development and demonstration [grant number 60715]: Ecohydrological Interfaces as Critical Hotspots for Transformations of Ecosystem Exchange Fluxes (INTERFACES).

The data supporting the conclusions can be obtained in the results section, figures and references.

Special thanks to Franziska Pöschke, Karin Meinikmann, Hauke Dämpfling and Anne Mehrtens for their technical and moral support.

Finally, we would like to thank the two anonymous reviewers and the editor Tim R. McVicar for the detailed and helpful reviews provided.

References

- Allan, R.G., Pereira, L., Raes, D., Smith, M., 1998. Crop evapotranspiration-Guidelines for computing crop water requirements-FAO Irrigation and drainage paper 56.
- Anderson, D.M., Glibert, P.M., Burkholder, J.M., 2002. Harmful algal blooms and eutrophication: nutrient sources, composition, and consequences. *Estuaries* 25, 704–726. <http://dx.doi.org/10.1007/BF02804901>.
- Anderson, J.M., Wilson, S.B., 1984. Review Article. The physical basis of current infrared remote-sensing techniques and the interpretation of data from aerial surveys. *Int. J. Remote Sens.* 1–18. <http://dx.doi.org/10.1080/01431168408948786>.
- Anselin, L., 1995. Local indicators of spatial association-LISA. *Geogr. Anal.* 27, 93–115. <http://dx.doi.org/10.1111/j.1538-4632.1995.tb00338.x>.
- Anselin, L., Syabri, I., Smirnov, O., 2002. Visualizing Multivariate Spatial Correlation with Dynamically Linked Windows. in: Anselin, L., Rey, S. (Eds.), *New Tools for Spatial Data Analysis: Proceedings of the Specialist Meeting*. Santa Barbara.
- Aubry-Wake, C., Baraer, M., McKenzie, J.M., Mark, B.G., Wigmore, O., Hellström, R., Lautz, L., Somers, L., 2015. Measuring glacier surface temperatures with groundbased thermal infrared imaging. *Geophys. Res. Lett.* 42, 8489–8497. <http://dx.doi.org/10.1002/2015GL065321>.
- Baker, B.H., Martinovic-Weigelt, D., Ferrey, M., Barber, L.B., Writer, J.H., Rosenberry, D.O., Kiesling, R.L., Lundy, J.R., Schoenfuss, H.L., 2014. Identifying non-point sources of endocrine active compounds and their biological impacts in freshwater lakes. *Arch. Environ. Contam. Toxicol.* 67, 374–388. <http://dx.doi.org/10.1007/s00244-014-0052-4>.
- Benyahya, L., Caissie, D., Satish, M.G., El-Jabi, N., 2012. Long-wave radiation and heat flux estimates within a small tributary in Catamaran Brook (New Brunswick, Canada), 484, 475–484. doi: 10.1002/hyp.8141.
- Boulton, A.J., Findlay, S., Marmonier, P., Stanley, E.H., Boulton, A.J., Findlay, S., Marmonier, P., Stanley, E.H., Valett, H.M., 1998. The Functional Significance of the Hyporheic Zone in Streams and Rivers Maurice Valett Source : *Annual Review of Ecology and Systematics*, Vol. 29 (1998), pp. 59–81 Published by : Annual Reviews Stable URL : <http://www.jstor.org/stable/221702> REFERENCE 29, 59–81.
- Brabrand, Å., Koestler, A.G., Borgström, R., 2002. Lake spawning of brown trout related to groundwater influx. *J. Fish Biol.* 60, 751–763. <http://dx.doi.org/10.1006/jfbi.2002.1901>.

- Briggs, M.A., Hare, D.K., Boutt, D.F., Davenport, G., Lane, J.W., 2016. Thermal infrared video details multiscale groundwater discharge to surface water through macropores and peat pipes. *Hydrol. Process.* 30, 2510–2511. <http://dx.doi.org/10.1002/hyp.10722>.
- Briggs, M.A., Voytek, E.B., Day-Lewis, F.D., Rosenberry, D.O., Lane, J.W., 2013. Understanding water column and streambed thermal refugia for endangered mussels in the Delaware River. *Environ. Sci. Technol.* 47, 11423–11431. <http://dx.doi.org/10.1021/es4018893>.
- Burnett, W.C., Aggarwal, P.K., Aureli, A., Bokuniewicz, H., Cable, J.E., Charette, M.A., Kontar, E., Krupa, S., Kulkarni, K.M., Loveless, A., Moore, W.S., Oberdorfer, J.A., Oliveira, J., Ozyurt, N., Povinec, P., Privitera, A.M.G., Rajar, R., Ramessur, R.T., Scholten, J., Stieglitz, T., Taniguchi, M., Turner, J.V., 2006. Quantifying submarine groundwater discharge in the coastal zone via multiple methods. *Sci. Total Environ.* 367, 498–543. <http://dx.doi.org/10.1016/j.scitotenv.2006.05.009>.
- Burnett, W.C., Bokuniewicz, H., Huettel, M., Moore, W.S., Taniguchi, M., 2003. Groundwater and pore water inputs to the coastal zone. *Biogeochemistry* 66, 3–33. <http://dx.doi.org/10.1023/B:BIOG.0000006066.21240.53>.
- Danielescu, S., MacQuarrie, K.T.B., 2011. Nitrogen loadings to two small estuaries, Prince Edward Island, Canada: a 2-year investigation of precipitation, surface water and groundwater contributions. *Hydrol. Process.* 957, 945–957. <http://dx.doi.org/10.1002/hyp.7881>.
- Danielescu, S., MacQuarrie, K.T.B., Faux, R.N., 2009. The integration of thermal infrared imaging, discharge measurements and numerical simulation to quantify the relative contributions of freshwater inflows to small estuaries in Atlantic Canada. *Hydrol. Process.* 23, 2847–2859. <http://dx.doi.org/10.1002/hyp.7383>.
- Davies, A.G., Calkins, J., Scharenbroich, L., Vaughan, R.G., Wright, R., Kyle, P., Castaño, R., Chien, S., Tran, D., 2008. Multi-instrument remote and in situ observations of the Erebus Volcano (Antarctica) lava lake in 2005: a comparison with the Pele lava lake on the jovian moon Io. *J. Volcanol. Geotherm. Res.* 177, 705–724. <http://dx.doi.org/10.1016/j.jvolgeores.2008.02.010>.
- Dugdale, S.J., 2016. A practitioner's guide to thermal infrared remote sensing of rivers and streams: recent advances, precautions and considerations. *Wiley Interdiscip. Rev. Water* 3, 251–268. <http://dx.doi.org/10.1002/wat2.1135>.

- Dugdale, S.J., Bergeron, N.E., St-Hilaire, A., 2015. Spatial distribution of thermal refuges analysed in relation to riverscape hydromorphology using airborne thermal infrared imagery. *Remote Sens. Environ.* 160, 43–55. <http://dx.doi.org/10.1016/j.rse.2014.12.021>.
- Frisbee, M.D., Shope, C.L., Briggs, M., Boutt, D.F., 2016. Field methods for the evaluation of groundwater and surface-water interactions. In: Cushman, J.H., Tartakovski, D.M. (Eds.), *The Handbook of Groundwater Engineering*. CRC Press.
- Goldman, D.B., 2010. Vignette and exposure calibration and compensation. *IEEE Trans. Pattern Anal. Mach. Intell.* 32, 2276–2288. <http://dx.doi.org/10.1109/TPAMI.2010.55>.
- Gupta, R.P., 2018. Image Quality and Principles of Interpretation. In: *Remote Sensing Geology*. Springer, Berlin, Heidelberg, pp. 107–114. http://dx.doi.org/10.1007/9783-662-55876-8_9.
- Handcock, R.N., Torgersen, C.E., Cherkauer, K.A., Gillespie, A.R., Tockner, K., Faux, R.N., Tan, J., 2012. Thermal infrared remote sensing of water temperature in riverine landscapes. *Fluv. Remote Sens. Sci. Manag.* 85–113. <http://dx.doi.org/10.1002/9781119940791.ch5>.
- Hare, D.K., Briggs, M.A., Rosenberry, D.O., Boutt, D.F., Lane, J.W., 2015. A comparison of thermal infrared to fiber-optic distributed temperature sensing for evaluation of groundwater discharge to surface water. *J. Hydrol.* 530, 153–166. <http://dx.doi.org/10.1016/j.jhydrol.2015.09.059>.
- Hayashi, M., Rosenberry, D., 2002. Effects of ground water exchange on the hydrology and ecology of surface water. *Ground Water* 40, 309–316.
- Hook, S.J., Clodius, W.B., Balick, L., Alley, R.E., Abtahi, A., Richards, R.C., Schladow, S.G., 2005. In-flight validation of mid- and thermal infrared data from the Multispectral Thermal Imager (MTI) using an automated high-altitude validation site at Lake Tahoe CA/NV, USA. *IEEE Trans. Geosci. Remote Sens.* 43, 1991–1999. <http://dx.doi.org/10.1109/TGRS.2005.853191>.
- Hu, C., Muller-karger, F.E., Swarzenski, P.W., 2006. Hurricanes, submarine groundwater discharge, and Florida ' s red tides. *Geophys. Res. Lett.* 33, 1–5. <http://dx.doi.org/10.1029/2005GL025449>.
- Johnson, A.G., Glenn, C.R., Burnett, W.C., Peterson, R.N., Lucey, P.G., 2008. Aerial infrared imaging reveals large nutrient-rich groundwater inputs to the ocean. *Geophys. Res. Lett.* 35, 1–6. <http://dx.doi.org/10.1029/2008GL034574>.
- Kelcey, J., Lucieer, A., 2012. Sensor correction of a 6-band multispectral imaging sensor for UAV remote sensing. *Remote Sens.* 4, 1462–1493. <http://dx.doi.org/10.3390/rs4051462>.

- Kordecki, A., Palus, H., Bal, A., 2016. Practical vignetting correction method for digital camera with measurement of surface luminance distribution. *Signal Image Video Process.* 10, 1417–1424. <http://dx.doi.org/10.1007/s11760-016-0941-2>.
- Krause, S., Blume, T., 2013. Impact of seasonal variability and monitoring mode on the adequacy of fiber-optic distributed temperature sensing at aquifer-river interfaces. *Water Resour. Res.* 49, 2408–2423. <http://dx.doi.org/10.1002/wrcr.20232>.
- Lee, E., Kang, K., Hyun, S.P., Lee, K.-Y., Yoon, H., Kim, S.H., Kim, Y., Xu, Z., Kim, D., Koh, D.-C., Ha, K., 2016. Submarine groundwater discharge revealed by aerial thermal infrared imagery: a case study on Jeju Island, Korea. *Hydrol. Process.* 3506, 3494–3506. <http://dx.doi.org/10.1002/hyp.10868>.
- Lee, Y., Kim, G., 2007. Linking groundwater-borne nutrients and dinoflagellate red-tide outbreaks in the southern sea of Korea using a Ra tracer. *Estuar. Coast. Shelf Sci.* 71, 309–317. <http://dx.doi.org/10.1016/j.ecss.2006.08.004>.
- Lega, M., Napoli, R.M.a., 2010. Aerial infrared thermography in the surface waters contamination monitoring. *Desalin. Water Treat.* 23, 141–151. <http://dx.doi.org/10.5004/dwt.2010.1988>.
- Lelong, C.C.D., Burger, P., Jubelin, G., Roux, B., Labbé, S., Baret, F., 2008. Assessment of unmanned aerial vehicles imagery for quantitative monitoring of wheat crop in small plots. *Sensors* 8, 3557–3585. <http://dx.doi.org/10.3390/s8053557>.
- Lewandowski, J., Meinikmann, K., Ruhtz, T., Pöschke, F., Kirillin, G., 2013. Localization of lacustrine groundwater discharge (LGD) by airborne measurement of thermal infrared radiation. *Remote Sens. Environ.* 138, 119–125. <http://dx.doi.org/10.1016/j.rse.2013.07.005>.
- Marruedo Arricibita, A.I., Krause, S., Gomez-Velez, J., Hannah, D.M., Lewandowski, J., 2018. Mesocosm experiments identifying hotspots of groundwater upwelling in a water column by fibre optic distributed temperature sensing. *Hydrol. Process.* 32, 185–199. <http://dx.doi.org/10.1002/hyp.11403>.
- Meier, F., Scherer, D., Richters, J., Christen, A., 2011. Atmospheric correction of thermal infrared imagery of the 3-D urban environment acquired in oblique viewing geometry. *Atmos. Meas. Tech.* 4, 909–922. <http://dx.doi.org/10.5194/amt-4-909-2011>.
- Meinikmann, K., Lewandowski, J., Nützmänn, G., 2013. Lacustrine groundwater discharge: combined determination of volumes and spatial patterns. *J. Hydrol.* 502, 202–211. <http://dx.doi.org/10.1016/j.jhydrol.2013.08.021>.

- Meng, H., Guan, W., Liu, C., Wu, Q., 2015. Algorithm research of vignetting distortion correction based on near-infrared CCD thermometer, in: *Design, Manufacturing and Mechatronics*. WORLD SCIENTIFIC, pp. 1290–1298. doi:10.1142/9789814730518_0151.
- Mundy, E., Gleeson, T., Roberts, M., Baraer, M., McKenzie, J.M., 2017. Thermal imagery of groundwater seeps: possibilities and limitations. *Groundwater*. <http://dx.doi.org/10.1111/gwat.12451>.
- Nakayama, T., Watanabe, M., 2008. Missing role of groundwater in water and nutrient cycles in the shallow eutrophic Lake Kasumigaura, Japan. *Hydrol. Process.* 22, 1150–1172. <http://dx.doi.org/10.1002/hyp.6684>.
- Neale, C.M.U., Jaworowski, C., Heasler, H., Sivarajan, S., Masih, A., 2016. Hydrothermal monitoring in Yellowstone National Park using airborne thermal infrared remote sensing. *Remote Sens. Environ.* 184, 628–644. <http://dx.doi.org/10.1016/j.rse.2016.04.016>.
- Norrström, A.C., Jacks, G., 1996. Water pathways and chemistry at the groundwater/ surface water interface to Lake Skjervatjern, Norway. *Water Resour. Res.* 32, 2221–2229 0043-1397/96/96WR-00802.
- Ouellet, V., Secretan, Y., St-Hilaire, A., Morin, J., 2014. Water temperature modelling in a controlled environment: comparative study of heat budget equations. *Hydrol. Process.* 28, 279–292. <http://dx.doi.org/10.1002/hyp.9571>.
- Röper, T., Greskowiak, J., Massmann, G., 2014. Detecting small groundwater discharge springs using handheld thermal infrared imagery. *Groundwater* 52, 936–942. <http://dx.doi.org/10.1111/gwat.12145>.
- Rosenberry, D.O., Lewandowski, J., Meinikmann, K., Nützmann, G., 2015. Groundwater – the disregarded component in lake water and nutrient budgets. Part 1: effects of groundwater on hydrology. *Hydrol. Process.* 29, 2895–2921. <http://dx.doi.org/10.1002/hyp.10403>.
- Schott, J.R., 1994. Thermal infrared calibration of aerial and satellite images over land, in: *geoscience and remote sensing symposium*. IEEE, Pasadena, CA, pp. 1–4. doi: 10.1109/IGARSS.1994.399083.
- Schuetz, T., Weiler, M., 2011. Quantification of localized groundwater inflow into streams using ground-based infrared thermography. *Geophys. Res. Lett.* 38, 1–5. <http://dx.doi.org/10.1029/2010GL046198>.

- Schuetz, T., Weiler, M., Lange, J., Stoelzle, M., 2012. Two-dimensional assessment of solute transport in shallow waters with thermal imaging and heated water. *Adv. Water Resour.* 43, 67–75. <http://dx.doi.org/10.1016/j.advwatres.2012.03.013>.
- Shaw, R.D., Shaw, J.F.H., Fricker, H., Prepas, E.E., 1990. An integrated approach to quantify groundwater transport of phosphorus to Narrow Lake. *Alberta* 35, 870–886.
- Sobrino, J.A., Del Frate, F., Drusch, M., Jiménez-Muñoz, J.C., Manunta, P., Regan, A., 2016. Review of thermal infrared applications and requirements for future high-resolution sensors. *IEEE Trans. Geosci. Remote Sens.* 54, 2963–2972. <http://dx.doi.org/10.1109/TGRS.2015.2509179>.
- Tamborski, J.J., Rogers, A.D., Bokuniewicz, H.J., Cochran, J.K., Young, C.R., 2015. Identification and quantification of diffuse fresh submarine groundwater discharge via airborne thermal infrared remote sensing. *Remote Sens. Environ.* 171, 202–217. <http://dx.doi.org/10.1016/j.rse.2015.10.010>.
- Taniguchi, M., Burnett, W.C., Cable, J.E., Turner, J.V., 2002. Investigation of submarine groundwater discharge. *Hydrol. Process.* 2129, 2115–2129. <http://dx.doi.org/10.1002/hyp.1145>.
- Tcherepanov, E.N., Zlotnik, V.a., Henebry, G.M., 2005. Using Landsat thermal imagery and GIS for identification of groundwater discharge into shallow groundwater dominated lakes. *Int. J. Remote Sens.* 26, 3649–3661. <http://dx.doi.org/10.1080/01431160500177315>.
- Tempelhahn, A., Budzier, H., Krause, V., Gerlach, G., 2016. Shutter-less calibration of uncooled infrared cameras. *J. Sensors Sens. Syst.* 5, 9–16. <http://dx.doi.org/10.5194/jsss-5-9-2016>.
- Tempelhahn, A., Budzier, H., Krause, V., Gerlach, G., 2015. Development of a shutterless calibration process for microbolometer-based infrared measurement systems. *ejournal Nondestructive Test* 20. <http://dx.doi.org/10.21611/qirt.2014.060>.
- Torgersen, C.E., Faux, R.N., McIntosh, B.A., Poage, N.J., Norton, D.J., 2001. Airborne thermal remote sensing for water temperature assessment in rivers and streams. *Remote Sens. Environ.* 76, 386–398. [http://dx.doi.org/10.1016/S0034-4257\(01\)00186-9](http://dx.doi.org/10.1016/S0034-4257(01)00186-9).
- Wang, X., Wang, X., Fan, J., Wen, S., Zhao, J., Su, X., 2016. Comparison of different spatial resolution thermal infrared data in monitoring thermal plume from the Hongyanhe nuclear power plant. 2016 IEEE Int. Geosci. Remote Sens. Symp. 4649–4652. doi: 10.1109/IGARSS.2016.7730213.
- Warren, D.R., Sebestyen, S.D., Josephson, D.C., Lepak, J.M., Kraft, C.E., 2005. Acidic groundwater discharge and in situ egg survival in redds of lake-spawning brook trout.

- Trans. Am. Fish. Soc. 134, 1193–1201. <http://dx.doi.org/10.1577/T04-180.1>.
- Wawrzyniak, V., Piégay, H., Allemand, P., Vaudor, L., Goma, R., Grandjean, P., 2016. Effects of geomorphology and groundwater level on the spatio-temporal variability of riverine cold water patches assessed using thermal infrared (TIR) remote sensing. *Remote Sens. Environ.* 175, 337–348. <http://dx.doi.org/10.1016/j.rse.2015.12.050>.
- Wirth, L., Rosenberger, A., Prakash, A., Gens, R., Margraf, J.F., Hamazak, T., 2012. A remote-sensing, gis-based approach to identify, characterize, and model spawning habitat for fall-run chum salmon in a sub-arctic, glacially fed River. *Trans. Am. Fish. Soc.* 141, 1349–1363. <http://dx.doi.org/10.1080/00028487.2012.692348>.
- Zuo, C., Chen, Q., Gu, G., Sui, X., 2011. Scene-based non-uniformity correction algorithm based on interframe registration. *J. Opt. Soc. Am. A* 28 (6), 1164. <http://dx.doi.org/10.1364/JOSAA.28.001164>.

5 Synopsis

5.1 Summary of results

- The positive buoyancy of relatively warm water imported by (simulated) LGD into shallow water bodies (e.g. the mesocosm) allows detection of LGD at the water surface-atmosphere interface by FO-DTS. Injection of warm water was conducted with different rates under different weather conditions (clear vs. overcast) over the entire diurnal cycle. This resulted in different upwelling patterns across the water column were described from the sediment-water interface through the water column to the water surface-atmosphere interface. Upwelling signals at the water surface were identified at all applied injection rates: 1 L min^{-1} , 5 L min^{-1} and 15 L min^{-1} . However, detectability of simulated LGD at the water surface-atmosphere interface was mainly determined by the diurnal cycle of the net radiation balance (R_n) and the cloud cover. Detection of simulated LGD at the water surface-atmosphere interfaces was best under overcast conditions and during the night (Chapter 3 and Figure 3.3).
- TIR can detect upwelling at the water surface. The diurnal cycle of incoming shortwave radiation as well as weather conditions (clear vs. overcast) have a substantial effect on the ability of TIR to accurately detect simulated warm water upwelling (in comparison to FO-DTS measurements). While simulated LGD was generally well-detected during overcast conditions and at night, TIR was less able to replicate FO-DTS observations during day and under clear sky conditions (Chapter 4, Figures 4.2 and 4.3).
- The HPD based approach is helpful to distinguish the overlapping impacts of heat transport processes across spatial and temporal scales. Heat fluxes related to simulated LGD and heat fluxes from the atmosphere (e.g. incident shortwave radiation) overlap across spatial and temporal scales. The detection of heat as a tracer for LGD depends on whether the heat signal related to LGD is dominant or overshadowed by heat fluxes coming from the atmosphere (Chapter 2).

5.2 Discussion

5.2.1 Impacts of diurnal cycle of net radiation and cloud cover on tracing of LGD

In the present PhD thesis, hydrometeorological parameters are identified as main controlling factors for detection of GW-SW interactions (in this case, LGD) at the water surface of stagnant water bodies such as lakes (research goal n°3, chapter 1.3). The strength of the heat

or temperature signal that solely belongs to the simulated warm LGD in the water column and at the water surface-atmosphere interface was strongly controlled by weather conditions (clear sky and overcast sky) and the diurnal cycle of the net radiation (Figures 3.3, 3.7 and 3.9). For instance, when simulating warm LGD at a rate of 1 L min^{-1} , the heat signal of the simulated warm LGD could be distinguished across the entire extent of the water column and the water surface but only under overcast weather conditions (Chapter 3, Figure 3.3 d). On the contrary, the heat signal of the simulated warm LGD could not be distinguished (during day) or did not reach the water surface (during night) under clear sky conditions (Chapter 3, Figure 3.3 a). In addition, calculated net heat fluxes across the water surface were stronger during clear sky day and more negative during clear sky night than during overcast day and night respectively (Chapter 3, Figure 3.8 a). This means that more heat was gained during the day or lost during the night across the water surface-atmosphere interface under clear sky conditions.

A more in-depth analysis revealed that the main component of the net heat fluxes across the water surface was the net radiation which is the sum of the net shortwave and the net longwave radiation (Chapter 3, Figure 3.8). Therefore, the diurnal cycle of the net radiation balance controlled the strength of the heat fluxes across the water surface and in consequence, the gains and losses of heat across the water surface. For this reason, during day under clear sky conditions, the warming effect of incident shortwave radiation at the water surface and some cm below the water surface prevented a differentiation of the heat signals of the simulated warm LGD and the radiation. During night under clear sky conditions, the heat signal of the simulated warm LGD was lost due to the strong cooling effect of the net longwave radiation across the water surface.

Finally, the cloud cover (clear sky vs. overcast sky) played an important role for the strength of the heat signal caused by simulated warm LGD. Cloud cover is an important controller of the diurnal cycle of the net radiation balance (Dai and Trenberth, 1999; Betts, 2003, 2015; Betts *et al.*, 2013) 1) by diminishing the incident shortwave radiation at the water surface and 2) by diminishing the cooling due to net longwave radiation from the water surface. This means that the heat gains and losses across the water surface under overcast conditions are smaller than under clear sky conditions. Therefore, during day under overcast conditions the heat signal related to the simulated warm LGD was discernible across the water column and at the water surface. During night under overcast conditions, the cooling effect of net longwave radiation at the water surface was weaker than under clear sky conditions,

preventing the loss of the heat signal related to the simulated warm LGD at the water surface as occurred under clear sky conditions.

5.2.2 FO-DTS for monitoring LGD in lakes

Most research on GW-SW interactions with FO-DTS is done in streams (Lowry *et al.*, 2007; Slater *et al.*, 2010; Krause *et al.*, 2012; Briggs *et al.*, 2013, 2016a; Mamer and Lowry, 2013; Birkham *et al.*, 2014; González-pinzón *et al.*, 2015; Rosenberry *et al.*, 2016) while research on lakes is not as common (Blume *et al.*, 2013; Sebok *et al.*, 2013; Liu *et al.*, 2015; Tristram *et al.*, 2015). Typically, the FO-DTS cable is deployed directly on the sediment bed or buried few cm in the sediment (Blume *et al.*, 2013; Tristram *et al.*, 2015). There are also few studies where the DTS cable was wrapped around tubes and inserted in the sediment to get a high resolution depth profile (Vogt *et al.*, 2010). To the best of my knowledge there is only one other study in which DTS was used to trace the heat signal of LGD across the water column. Sebok *et al.* (2013) deployed the FO-DTS at three different depths in the water column of Lake Væng close to the shore of the lake and at three different distances from the shore of the lake. Influence of solar radiation on monitored water temperatures by FO-DTS was mentioned as a relevant factor affecting the detection of LGD across the water column and the water surface-atmosphere interface during the spring and summer months. Only night measurements reliably detected LGD for periods with strong solar radiation. However, in Sebok *et al.* (2013) the influence of solar radiation during winter conditions was neglected. Finally Sebok *et al.* (2013) concluded that the positive buoyancy of the LGD was responsible for the lack of ice cover at those specific water surface areas recommending more elaborate multilevel FO-DTS setups in order to further understand the development of the thermal plumes related to LGD in three dimensions. The three dimensional and more elaborated FO-DTS setup of the present PhD thesis allowed describing interactions between simulated GW discharge, upwelling warm water and cold SW in terms of spatial and temporal distribution of temperature through the water column (research goal n°2, chapter 1.3) at different weather conditions and over the entire diurnal cycle (Chapter 3 and Figure 3.3). The different warm water upwelling patterns monitored by the FO-DTS setup, allowed considering possible connections between the monitored spatial patterns of the heat signal and the different weather conditions and the diurnal cycle (addressed in chapter 5.2.1). Thus, FO-DTS is a useful method for spatial pattern characterization of warm water upwelling in the water column and for supporting other methods (e.g. TIR) to identify hotspots of GW discharge at different interfaces such as at the water surface-atmosphere interface. Some other researches (e.g. Blume *et al.*, 2013) successfully used as well FO-DTS in combination with other

methods for 2 dimensional spatial pattern identification of LGD at the sediment-water interface. In addition, in most of the studies (Krause *et al.*, 2012; Sebok *et al.*, 2015) the main focus is on the horizontal spatial pattern characterization at the sediment surface or at the water surface in order to get more insights about LGD and to detected hotspots of GW discharge. Thus, generally the FO-DTS is not setup across the water column. However, vertical pattern characterization across the water column of simulated LGD allowed understanding the mechanism of the upwelling process of warm GW and how the heat signal propagated across the water column. Thus, 2 and 3 dimensional FO-DTS setups seem to improve the mechanistic understanding of LGD in terms of temperature spatial patterns at different interfaces (sediment-water or water surface-atmosphere) and across the water column.

Finally, since TIR imaging is the most appropriate method for monitoring water temperature at the water surface, FO-DTS is a reliable method for ground truthing TIR data monitored at the water surface (see Chapter 4).

5.2.3 TIR imaging for detection of LGD at the lake surface

TIR imaging is broadly used in marine science (Johnson *et al.*, 2008; Tamborski *et al.*, 2015; Lee *et al.*, 2016) and sometimes also in freshwater systems, especially streams, (Hare *et al.*, 2015; Wawrzyniak *et al.*, 2016) to detect groundwater discharge at medium to large scales (e.g. km²). TIR imaging was seldom used to detect LGD (Rundquist and Murray, 1985; Cook *et al.*, 1991; Anderson *et al.*, 1995; Lewandowski *et al.*, 2013) and research on the adequacy and reliability of TIR imaging for detection of LGD at the water surface-atmosphere interface is still insufficient. Only few other recent researches (e.g. Aubry-Wake *et al.*, 2015; Mundy *et al.*, 2017) have paid attention to the importance of weather conditions and diurnal cycle of air temperatures and solar radiation on TIR measurements. Still, these examples are not related to LGD in freshwater bodies but to bed rock to air GW seepage detection (Mundy *et al.*, 2017) or TIR imaging in high altitude alpine environments (Aubry-Wake *et al.*, 2015).

As discussed in Chapters 3 and 5.2.1, the strength of the heat or temperature signal that exclusively corresponds to the simulated warm LGD across the water column and at the water surface-atmosphere interface is strongly controlled by weather conditions (clear sky vs. overcast sky) and the diurnal cycle of the net radiation. This is of relevance for TIR imaging of LGD at the water surface-atmosphere interface because the TIR sensor monitors longwave radiation that is emitted and reflected from the water surface. This implies that thermal

images acquired by TIR imaging include information on: 1) water surface temperature and 2) on reflections from clouds or the vegetation around the water body (Anderson and Wilson, 1984; Schott, 1994; Torgersen *et al.*, 2001; Handcock *et al.*, 2012). Thus, the heat or temperature signal of the simulated warm LGD should be predominant over the longwave radiation reflected from the water surface.

In chapter 4, interactions between simulated GW discharge, upwelling warm water and cold SW were described in terms of spatial and temporal distribution of temperature at the water surface by TIR (research goal n°2, chapter 1.3). FO-DTS measurements were used for spatial validation of monitored temperatures by TIR imaging (Chapter 4, Figures 4.2 and 4.3). TIR measurements were affected by the weather conditions (clear sky vs. overcast sky) and the diurnal cycle of the net longwave radiation (Figures 4.2 and 4.3). Most reliable TIR images were obtained under overcast weather conditions and during night (no solar radiation). During day under overcast conditions, TIR images contained longwave reflections from vegetation and from the homogeneous cloud cover. The majority of the reflections from vegetation were masked by reflections due to the cloud cover in the sky resulting in a uniform background of reflections in the TIR image. Consequently, the heat or temperature signal from the simulated warm LGD was clearly distinguishable from the homogeneous background related to longwave reflections. During night under overcast weather conditions, longwave radiation from vegetation was smaller than during day due to reduced vegetation temperature in comparison to day temperatures. The lack of incident shortwave radiation at night was the main reason for reduced vegetation temperature. In consequence, longwave reflections of vegetation on the water surface were weaker during night. This allowed easier detection of heat or temperature signal related to the simulated warm LGD at the water surface with TIR imaging.

The results presented and discussed in chapter 4 demonstrate that close-range TIR imaging is a method with potential for detecting LGD at the water surface. Nevertheless, the reliability of the data obtained with TIR imaging depends on several hydrometeorological factors such as cloud cover and diurnal cycle of net radiation.

5.2.4 Combination of multiple heat tracing techniques for scaling of GW-SW interactions across ecohydrological interfaces

Several recent researches combined multiple techniques to describe GW-SW interactions across the scale continuum (Blume *et al.*, 2013; Hare *et al.*, 2015; Rosenberry *et al.*, 2016; Wilson and Rocha, 2016). Nevertheless there is still a knowledge gap on the process understanding of GW-SW interactions and its controlling factors over several spatial and

temporal scales. Controlling factors of GW-SW interactions can be hydrogeological and hydrometeorological. This is determined by the interface at which the GW-SW interactions are studied or monitored. When monitoring GW-SW interactions at the aquifer-stream/lake interface, hydrogeological controlling factors play a key role on regulating GW-SW interactions. For instance, the spatial distribution and heterogeneity of hydraulic conductivity of the HZ or the lacustrine sediments and the underlying aquifer is a well reported controlling factor for GW-SW interactions (Leek *et al.*, 2009; Angermann *et al.*, 2012a; Blume *et al.*, 2013). On the contrary, when monitoring GW-SW interactions at the water surface-atmosphere interface, hydrometeorological controlling factors are key parameters on regulating GW-SW interactions (Chapter 3 and 4). In the latter case, there are really few researches that mention how hydrometeorological factors control the identification/measurement of GW-SW interactions across the water column and the water surface-atmosphere interface of freshwater bodies, especially lakes (e.g. Sebok *et al.*, 2013). Therefore, there is still a lack of balance between measurements and process understanding of GW-SW interactions over several spatial and temporal scales and across ecohydrological interfaces (e.g. sediment-water, water surface-atmosphere). For instance, in Lewandowski *et al.* (2013) airborne TIR imaging of the entire Lake Arendsee showed warm water areas at the lake surface and close to the lake's shore. Temperature data collected by temperature lances at different depths in the lacustrine sediment at the shore of the lake as well was used to calculate LGD fluxes at the shore of the lake. Both techniques seemed to indicate potential LGD hotspots in nearby areas located at the lake surface and at the sediment of the lake, respectively. However, further research showed that the warm water areas detected by TIR imaging at the lake surface were linked to wind-driven upwelling of cold water (Pöschke *et al.*, 2015). Thus, hydrometeorological factors (e.g. wind over the lake surface) had an important effect on the reliability of heat tracing techniques for monitoring GW-SW interactions at the lake surface. In addition, heat transport processes in the sediment differ from heat transport processes in the water column and across the water surface-atmosphere interface (see Chapters 1.4.2 to 1.4.6). Therefore, potential hotspots of GW-SW interactions monitored in the sediment or lake bed might not always agree with thermal anomalies detected with other heat tracing techniques at the lake surface.

The new technology available at the moment, allows collecting data at different interfaces (e.g. TIR at the water surface or FO-DTS at the lake bed). However, there is not an agreement

on a unique method for transferring and combining data collected with different heat tracing techniques, between different ecohydrological interfaces and over several scales (in the present PhD thesis, spatial scales). More specifically speaking, a general conceptual framework for freshwater systems that unites water and heat exchange processes (LGD, HEF and water flow from saturated to unsaturated areas) monitored by various heat tracing techniques across several ecohydrological interfaces and spatial scales, is missing. This knowledge gap motivated the development of a general conceptual framework based on HPD that could work as guidance for identifying and quantifying water and heat exchange related to GW-SW interactions, in freshwater systems across ecohydrological interfaces and over several spatial scales, by combining various heat tracing techniques (Chapter 2) (research goal n°1, chapter 1.3). The application of hierarchy theory and HPD can be found in a number of environmental sciences and in ecohydrological publications (e.g. Frissell *et al.*, 1986; Dent *et al.*, 2001; Poole and Berman, 2001). Nevertheless, ecohydrological interfaces in freshwater systems are not usually approached from a landscape perspective (Soranno *et al.*, 2009). Part of the uniqueness of the present PhD thesis resides on the fact that this is the first time that HPD was employed to design a conceptual framework for appropriately combining several heat tracing techniques across ecohydrological interfaces and over several spatial scales for process understanding of GW-SW interactions.

The experimental design based on HPD (Chapter 2, 3 and 4) demonstrated to be successful on: 1) hypothesis testing of this PhD thesis: the positive buoyancy of warm GW upwelling across the water column during winter, allows the detection of LGD at the water surface by TIR and 2) identifying controlling hydrometeorological factors of LGD across the water column and at the water surface-atmosphere interface (research goal n°3, chapter 1.3).

The example presented in the present PhD thesis could be extrapolated to other heat tracing devices. We believe that this integrated approach could aid researchers on scaling GW-SW interactions by using multiple heat tracing techniques at various ecohydrological interfaces. In addition, if the same scaling approach is used by all researchers, findings on GW-SW interactions across different ecohydrological interfaces and spatial scales could be combined resulting in a successful increase on process understanding of GW-SW interactions across ecohydrological interfaces and over several spatial scales, in freshwater environments.

5.3 Conclusions

The present PhD revealed that under specific conditions it is possible to up and down scale LGD from the sediment-water interface through the water column to the water surface-atmosphere interface by heat tracing techniques (main research goal of this PhD thesis). In

Chapters 3 and 4 it is demonstrated that the positive buoyancy of warm GW causes upwelling across the cold water column during winter and allows the detection of LGD at the water surface by TIR. However, the heat signal related to warm GW at the water surface is best detected under overcast conditions and during night. Therefore, the upscaling of LGD from the sediment-water interface to the water surface-atmosphere interface (e.g. lakes surface) is strongly controlled by hydrometeorological factors such as cloud cover and diurnal cycle of the net radiation balance. Nevertheless, in real lake settings (instead of our model mesocosm) it should be considered that the chances to detect LGD at the water surface of the lake might decrease due to several factors that have not been considered in the present PhD thesis research (e.g. wind, vegetation in the water column). Thus, there are several limitations that make the detection of LGD at the water surface of a lake difficult:

- The positive buoyancy of GW occurs only during a short period of time (Lewandowski *et al.*, 2013).
- In real lake settings, currents or mixing due to wind might reduce the GW signal.
- In most cases LGD rates will be much smaller than in the present study (for instance median exfiltration rates of 0.74 cm d^{-1} ($= 0.005 \text{ L m}^{-2} \text{ min}^{-1}$) and a maximum of 745 cm d^{-1} ($= 5.2 \text{ L m}^{-2} \text{ min}^{-1}$) are reported in Rosenberry *et al.* (2015)).
- In most parts of a lake the water column is thicker and thus the travel distance between sediment surface and water surface larger (the signal might be lost).

On the contrary, the circumstances that increase the chance to see a strong signal of GW at the water surface of lakes can be:

- Focused and high discharge rates in Karst aquifers or in lakes with macropore groundwater discharge (see chapter 3.2.1: Simulated upwelling flux rates vs. rates reported in literature.)
- Salinity gradient with the groundwater fresher than the lake water.
- Suitable weather conditions as demonstrated in the present PhD thesis.
- Discrete or focused LGD in shallow lakes or at the shore of the lake.

5.4 Future direction

The present PhD thesis has shown the relevance of hydrometeorological factors for detection of LGD at the water surface by FO-DTS and TIR imaging. The results and conclusions presented in the thesis support research on the mechanistic understanding of LGD across

various interfaces and over several scales. To deepen and supplement the knowledge gained in the thesis, I would recommend experiments/measurement campaigns in natural shallow lakes or near the shore of lakes where LGD occurs. The measurements should take place during winter and preferably following the recommendations presented in this PhD thesis (under overcast conditions and if possible at night). LGD rates need to be determined with independent methods such as seepage meters and temperature lances between others. The impacts of wave mixing near the shore or wind forces at the water surface, could be studied and would increase the mechanistic understanding of LGD and upwelling under natural conditions. Next, the data collected in this type of experiments, could be used to parametrize new models that could predict the location of thermal plumes related to LGD, at the surface of the lake. Finally, TIR cameras setup in drones could be used for validation of the model predictions.

5.5 References

- Anderson JM, Wilson SB. 1984. Review Article. The physical basis of current infrared remote-sensing techniques and the interpretation of data from aerial surveys. *International Journal of Remote Sensing* (5:1): 1–18 DOI: 10.1080/01431168408948786
- Anderson JM, Duck RW, McManus J. 1995. Thermal radiometry: a rapid means of determining surface water temperature variations in lakes and reservoirs. *Journal of Hydrology* **173**: 131–144
- Angermann L, Krause S, Lewandowski J. 2012. Application of heat pulse injections for investigating shallow hyporheic flow in a lowland river. *Water Resources Research* **48** (October): 1–16 DOI: 10.1029/2012WR012564
- Aubry-Wake C, Baraer M, McKenzie JM, Mark BG, Wigmore O, Hellström R, Lautz L, Somers L. 2015. Measuring glacier surface temperatures with ground-based thermal infrared imaging. *Geophysical Research Letters* **42** (20): 8489–8497 DOI: 10.1002/2015GL065321
- Betts AK. 2003. The diurnal cycle over land. In *Forests at the Land-Atmosphere Interface*, Mencuccini M, , Grace J, , Moncrieff J, , McNaughton K (eds). CABI Publishing, Wallingford, Oxon OX10 8DE, UK; 73–93.
- Betts AK. 2015. Diurnal Cycle. In *Encyclopedia of Atmospheric Sciences*, Pyle J, , Fuqing Z (eds). Texas A&M University, College Station, TX, USA; 319–323. DOI: 10.1016/B978-0-12-382225-3.00135-3
- Betts AK, Desjardins R, Worth D. 2013. Cloud radiative forcing of the diurnal cycle climate of the Canadian Prairies. *Journal of Geophysical Research* **118** (June): 8935–8953 DOI: 10.1002/jgrd.50593
- Birkham T, Barbour SL, Goodbrand A, Tallon L, Szmigielski J, Klein R. 2014. Assessing groundwater discharge to streams with distributed temperature sensing technology
- Blume T, Krause S, Meinikmann K, Lewandowski J. 2013. Upscaling lacustrine groundwater discharge rates by fiber-optic distributed temperature sensing. *Water Resources Research* **49** (October 2012): 7929–7944 DOI: 10.1002/2012WR013215
- Briggs MA, Buckley SF, Bagtzoglou AC, Werkema DD, Lane JW. 2016. Actively heated high-resolution fiber-optic-distributed temperature sensing to quantify streambed flow dynamics in zones of strong groundwater upwelling. **52**: 5179–5194 DOI: 10.1002/2015WR018219
- Briggs MA, Voytek EB, Day-Lewis FD, Rosenberry DO, Lane JW. 2013. Understanding

- water column and streambed thermal refugia for endangered mussels in the Delaware River. *Environmental Science and Technology* **47** (20): 11423–11431 DOI: 10.1021/es4018893
- Cook JM, Edmunds WM, Robins NS. 1991. Groundwater contribution to an acid upland lake (loch fleet, scotland) and the possibilities for amelioration. *Journal of Hydrology* **125**: 111–128
- Dai A, Trenberth KE. 1999. Effects of Clouds , Soil Moisture , Precipitation , and Water Vapor on Diurnal Temperature Range. *Journal of Climate* **12**: 2451–2473
- Dent CL, Grimm NB, Fisher SG. 2001. Multiscale effects of surface-subsurface exchange on stream water nutrient concentrations. *Journal of the North American Benthological Society* **20** (2): 162–181 DOI: 10.2307/1468313
- Frissell CA, Liss WJ, Warren CE, Hurley MD. 1986. A hierarchical framework for stream habitat classification: Viewing streams in a watershed context. *Environmental Management* **10** (2): 199–214 DOI: 10.1007/BF01867358
- González-pinzón R, Ward AS, Hatch CE, Wlostowski AN, Singha K, Gooseff MN, Haggerty R, Harvey JW, Cirpka OA, Brock JT. 2015. A field comparison of multiple techniques to quantify groundwater – surface-water interactions. *Freshwater Science* **34** (1): 139–160 DOI: 10.1086/679738.
- Handcock RN, Torgersen CE, Cherkauer KA, Gillespie AR, Tockner K, Faux RN, Tan J. 2012. Thermal Infrared Remote Sensing of Water Temperature in Riverine Landscapes. *Fluvial Remote Sensing for Science and Management*: 85–113 DOI: 10.1002/9781119940791.ch5
- Hare DK, Briggs MA, Rosenberry DO, Boutt DF, Lane JW. 2015. A comparison of thermal infrared to fiber-optic distributed temperature sensing for evaluation of groundwater discharge to surface water. *Journal of Hydrology* **530**: 153–166 DOI: 10.1016/j.jhydrol.2015.09.059
- Johnson AG, Glenn CR, Burnett WC, Peterson RN, Lucey PG. 2008. Aerial infrared imaging reveals large nutrient-rich groundwater inputs to the ocean. *Geophysical Research Letters* **35** (15): 1–6 DOI: 10.1029/2008GL034574
- Krause S, Blume T, Cassidy NJ. 2012. Investigating patterns and controls of groundwater upwelling in a lowland river by combining Fibre-optic Distributed Temperature Sensing with observations of vertical hydraulic gradients. *Hydrology and Earth System Sciences* **16** (6): 1775–1792 DOI: 10.5194/hess-16-1775-2012
- Lee E, Kang K, Hyun SP, Lee K-Y, Yoon H, Kim SH, Kim Y, Xu Z, Kim D, Koh D-C, et al.

2016. Submarine groundwater discharge revealed by aerial thermal infrared imagery: a case study on Jeju Island, Korea. *Hydrological Processes* **3506** (June): 3494–3506 DOI: 10.1002/hyp.10868
- Leek R, Wu JQ, Hanrahan TP, Barber ME, Qiu H. 2009. Heterogeneous characteristics of streambed saturated hydraulic conductivity of the Touchet River, south eastern Washington, USA. *Hydrological Processes* **23**: 1236–1246 DOI: 10.1002/hyp.7258
- Lewandowski J, Meinikmann K, Ruhtz T, Pöschke F, Kirillin G. 2013. Localization of lacustrine groundwater discharge (LGD) by airborne measurement of thermal infrared radiation. *Remote Sensing of Environment* **138**: 119–125 DOI: 10.1016/j.rse.2013.07.005
- Liu C, Liu J, Wang X, Zheng C. 2015. Analysis of Groundwater-Lake Interaction by Distributed Temperature Sensing in Badain Jaran Desert , Northwest China. *Hydrological Processes* DOI: 10.1002/hyp.10705
- Lowry CS, Walker JF, Hunt RJ, Anderson MP. 2007. Identifying spatial variability of groundwater discharge in a wetland stream using a distributed temperature sensor. *Water Resources Research* **43** (10): n/a-n/a DOI: 10.1029/2007WR006145
- Mamer EA, Lowry CS. 2013. Locating and quantifying spatially distributed groundwater / surface water interactions using temperature signals with paired fiber-optic cables. **49**: 7670–7680 DOI: 10.1002/2013WR014235
- Mundy E, Gleeson T, Roberts M, Baraer M, McKenzie JM. 2017. Thermal Imagery of Groundwater Seeps: Possibilities and Limitations. *Groundwater* (2009) DOI: 10.1111/gwat.12451
- Poole GC, Berman CH. 2001. An Ecological Perspective on In-Stream Temperature : Natural Heat Dynamics and Mechanisms of Human-Caused Thermal Degradation. **27** (6): 787–802 DOI: 10.1007/s002670010188
- Pöschke F, Lewandowski J, Engelhardt C, Preuß K, Oczipka M, Ruhtz T, Kirillin G. 2015. Upwelling of deep water during thermal stratification onset—A major mechanism of vertical transport in small temperate lakes in spring? *Water Resources Research* **51** (January 2016): 9612–9627 DOI: 10.1002/2015WR017579
- Rosenberry DO, Briggs MA, Delin G, Hare DK. 2016. Combined use of thermal methods and seepage meters to efficiently locate, quantify, and monitor focused groundwater discharge to a sand-bed stream. *Water Resources Research* **52** (6): 4486–4503 DOI: 10.1002/2016WR018808. Received
- Rosenberry DO, Lewandowski J, Meinikmann K, Nitzmann G. 2015. Groundwater - the

- disregarded component in lake water and nutrient budgets. Part 1: Effects of groundwater on hydrology. *Hydrological Processes* **29** (13): 2895–2921 DOI: 10.1002/hyp.10403
- Rundquist D, Murray G. 1985. Airborne thermal mapping of a ‘flow-through’ lake in the nebraska sandhills. *Water resources bulletin* **21** (6)
- Schott JR. 1994. Thermal Infrared Calibration of Aerial and Satellite Images Over Land. In *Geoscience and Remote Sensing Symposium* IEEE: Pasadena, CA; 1–4. DOI: 10.1109/IGARSS.1994.399083
- Sebok E, Duque C, Engesgaard P, Boegh E. 2015. Application of Distributed Temperature Sensing for coupled mapping of sedimentation processes and spatio-temporal variability of groundwater discharge in soft-bedded streams. *Hydrological Processes* **3422** (March): 3408–3422 DOI: 10.1002/hyp.10455
- Sebok E, Duque C, Kazmierczak J, Engesgaard P, Nilsson B, Karan S, Frandsen M. 2013. High-resolution distributed temperature sensing to detect seasonal groundwater discharge into Lake Væng , Denmark. **49** (July): 5355–5368 DOI: 10.1002/wrcr.20436
- Slater LD, Ntarlagiannis D, Day-Lewis FD, Mwakanyamale K, Versteeg RJ, Ward A, Strickland C, Johnson CD, Lane JW. 2010. Use of electrical imaging and distributed temperature sensing methods to characterize surface water-groundwater exchange regulating uranium transport at the Hanford 300 Area, Washington. *Water Resources Research* **46** (10): 1–13 DOI: 10.1029/2010WR009110
- Soranno PA, Webster KE, Cheruvilil KS, Bremigan MT. 2009. The lake landscape-context framework : linking aquatic connections , terrestrial features and human effects at multiple spatial scales. *Verh. Internat. Verein. Limnol.* **30** (January): 695–700
- Tamborski JJ, Rogers AD, Bokuniewicz HJ, Cochran JK, Young CR. 2015. Identification and quantification of diffuse fresh submarine groundwater discharge via airborne thermal infrared remote sensing. *Remote Sensing of Environment* **171**: 202–217 DOI: 10.1016/j.rse.2015.10.010
- Torgersen CE, Faux RN, McIntosh BA, Poage NJ, Norton DJ. 2001. Airborne thermal remote sensing for water temperature assessment in rivers and streams. *Remote Sensing of Environment* **76** (3): 386–398 DOI: 10.1016/S0034-4257(01)00186-9
- Tristram DA, Krause S, Levy A, Robinson ZP, Waller RI, Weatherill JJ. 2015. Identifying spatial and temporal dynamics of proglacial groundwater – surface-water exchange using combined temperature-tracing methods. *Freshwater Science* **34** (October 2013): 99–110 DOI: 10.1086/679757.

- Vogt T, Schneider P, Hahn-woernle L, Cirpka OA. 2010. Estimation of seepage rates in a losing stream by means of fiber-optic high-resolution vertical temperature profiling. *Journal of Hydrology* **380** (1–2): 154–164 DOI: 10.1016/j.jhydrol.2009.10.033
- Wawrzyniak V, Piégay H, Allemand P, Vaudor L, Goma R, Grandjean P. 2016. Effects of geomorphology and groundwater level on the spatio-temporal variability of riverine cold water patches assessed using thermal infrared (TIR) remote sensing. *Remote Sensing of Environment* **175**: 337–348 DOI: 10.1016/j.rse.2015.12.050
- Wilson J, Rocha C. 2016. A combined remote sensing and multi-tracer approach for localising and assessing groundwater-lake interactions. *International Journal of Applied Earth Observations and Geoinformation* **44**: 195–204 DOI: 10.1016/j.jag.2015.09.006

Acknowledgements

I would like to thank Jörg Lewandowski and Stefan Krause for their help and supervision during my PhD as well as for giving me the opportunity to do my PhD within the European Union's FP7: Ecohydrological Interfaces as Critical Hotspots for Transformations of Ecosystem Exchange Fluxes (INTERFACES).

Thank you to the entire INTERFACES team for their work on creating this project and for trusting in the ESRs achieving the goals established in this project.

Special thanks to Jesús Gomez-Velez and Stephen Dugdale for helping me with analyzing my data and sharing with me their knowledge in physics and thermal infrared imaging, respectively.

Thank you to Hauke Dämpfling, Anne Mehrrens and Jörg Friedrich (Fritz) for their help during my field work during the cold winter days in January-March 2015.

Thank you to Karin Meinikmann and Franziska Pöschke for being such good office mates and colleagues and for all your help and advices during all this time. Thank you to my all IGB mates as well, for the good times having a beer at the boat house, playing volley or simply having lunch together or eating cake.

Big thank you to my colleagues at University of Birmingham (UoB) and now friends: Silvia Folegot, Rhoswen Leonard, Sophie Briffa, Sophie Comer, Rebwar Dara and Grace Garner for supporting me through my PhD and having such good times in Birmingham.

Special thanks to Paul Romeijn who accompanied and supported me no matter what during my entire PhD.

Finally, I would like to thank my family, who played a crucial role on the achievement of all my life goals, this time, on successfully finishing my PhD.

Declaration of independent work

I declare that I have completed the thesis independently using only the aids and tools specified. I have not applied for a doctor's degree in the doctoral subject elsewhere and do not hold a corresponding doctor's degree. I have taken due note of the Faculty of Mathematics and Natural Sciences PhD Regulations, published in the Official Gazette of Humboldt-Universität zu Berlin no. 126/2014 on 18/11/2014.

Berlin, 4 December 2017

Amaya I. Marruedo Arricibita